Models of Rotationally Symmetric, Collision-Dominated Debris Discs

—DISSERTATION—

zur Erlangung des Akademischen Grades
Doctor Rerum Naturalium (Dr. rer. nat.)

vorgelegt dem Rat der Physikalisch-Astronomischen Fakultät
der Friedrich-Schiller-Universität Jena

von Dipl.-Phys. TORSTEN LÖHNE
geb. am 15.10.1979 in Sömmerda

1. Gutachter: Prof. Dr. Alexander V. Krivov
Friedrich-Schiller-Universität Jena

2. Gutachter: Prof. Dr. Philippe Thébault
Stockholms Universitet und Observatoire de Paris

3. Gutachter: Prof. Dr. Mark C. Wyatt
University of Cambridge

Tag des Rigorosums: 06. Juni 2008

Tag der öffentlichen Verteidigung: 19. Juni 2008

Contents

Danksagung vi

Kurzfassung vii

Abstract viii

1 Introduction 1

2 Background 3
- 2.1 Preliminaries 3
  - 2.1.1 Size and Mass Distributions 3
  - 2.1.2 Orbital Elements 4
  - 2.1.3 Units 4
- 2.2 Collisions 4
  - 2.2.1 Disruptive Collisions and Critical Specific Energy for Dispersal 5
  - 2.2.2 Cratering Collisions 7
  - 2.2.3 Rebound and Agglomeration 8
- 2.3 Interaction with Radiation 8
  - 2.3.1 Scattering, Absorption and Thermal Emission 8
  - 2.3.2 Influence on Orbital Motion 10
  - 2.3.3 Poynting-Robertson Drag 11
- 2.4 Other Effects 11
  - 2.4.1 Planetary Perturbations and Self-Stirring 11
  - 2.4.2 Cometary Activity 12
  - 2.4.3 Wind Drag 12
  - 2.4.4 Electric Charge 13
- 2.5 The Solar System 13
  - 2.5.1 The Edgeworth-Kuiper Belt 13
  - 2.5.2 Interplanetary Dust and the Zodiacal Cloud 14

3 Kinetic Theory and its Implementation 16
- 3.1 The Phase Space 16
  - 3.1.1 Densities 16
  - 3.1.2 Discretization and Averaging 17
  - 3.1.3 Phase Space Variables 18
- 3.2 The Master Equation 19
  - 3.2.1 Gain and Loss 19
  - 3.2.2 Discretization 21
  - 3.2.3 The Grid 23
- 3.3 Treatment of Collisions 24
  - 3.3.1 Impact Velocity and Probability 24
  - 3.3.2 Characterization of Outcomes 28
  - 3.3.3 The Fragment-Mass Distribution 29
  - 3.3.4 Orbital Elements of Fragments 30

3.4 Transport Mechanisms . . . 32
3.4.1 General Description . . . 32
3.4.2 Poynting-Robertson and Wind Drag . . . 32
3.5 The Integrator . . . 33
3.6 The ACE Code . . . 34

4 Dust in Collisional Equilibrium 35
4.1 Introduction: Vega as an Example . . . 35
4.2 Description of Numerical Runs . . . 35
4.3 Size Distribution . . . 36
4.3.1 The Lack of Unbound Grains . . . 36
4.3.2 The Wave . . . 36
4.3.3 Disc Mass and Mass Loss . . . 39
4.3.4 Cratering Collisions . . . 40
4.4 Spatial Distribution . . . 40
4.4.1 Distribution of Orbital Elements . . . 40
4.4.2 Radial Profiles . . . 41
4.4.3 Surface Brightness . . . 42
4.5 Discussion of the Vega Problem . . . 43

5 Long-Term Evolution 46
5.1 Introduction: Observational Statistics and Models . . . 46
5.2 Description of Numerical Runs . . . 47
5.2.1 Commons for All Runs . . . 47
5.2.2 Specifics of Individual Runs . . . 47
5.3 Numerical Results and Scaling Laws . . . 48
5.3.1 Evolution of Discs of Different Masses . . . 48
5.3.2 Dependence on Distance from the Star . . . 49
5.3.3 Dependence on Eccentricities of Parent Bodies . . . 50
5.4 Analytic Model for Evolution of Disc Mass and Dust Mass . . . 51
5.4.1 Three-Slope Distribution . . . 51
5.4.2 Collisional Lifetimes of Planetesimals . . . 53
5.4.3 Evolution of Disc Mass . . . 55
5.4.4 Evolution of Disc Mass at Latest Stages . . . 57
5.4.5 Evolution of Mass in Dynamically “Cold” Discs . . . 57
5.4.6 Evolution of Dust Mass . . . 58
5.4.7 The Slope of the Steady-State Size Distribution . . . 59
5.4.8 Model Parameters . . . 59
5.5 Evolution of Disc Luminosity . . . 61
5.5.1 Fractional Luminosity for a Given Age . . . 61
5.5.2 24 and 70 Micron Fluxes from Partial Rings . . . 62
5.5.3 Fluxes from Extended Discs . . . 63
5.6 Comparison with Observational Data . . . 64
5.6.1 Spitzer Data . . . 64
5.6.2 Population Synthesis . . . 65

6 Summary and Conclusions 69

Bibliography 72

Ehrenwörtliche Erklärung 81

Lebenslauf **82**

Danksagung

Gleich zu Beginn möchte ich ganz herzlich allen danken, die mich in den vergangenen Jahren unterstützt und mir die Arbeit erleichtert haben.

Da ist natürlich zunächst Prof. Alexander Krivov zu nennen, der Vertrauen in mich gesetzt und meine Arbeit in der Theoriegruppe des Astrophysikalischen Instituts Jena betreut hat. In zahlreichen Besprechungen und Diskussionen war er stets bedacht darauf, der Gruppe und mir mit durchdachter Didaktik fachliches Wissen und Erfahrung zu vermitteln und einen Einblick in den internationalen Wissenschaftsbetrieb zu geben. Der Austausch und die Diskussion in der Arbeitsgruppe halfen oftmals, Ziele klarer zu definieren sowie Probleme besser zu erkennen und Lösungen schneller zu finden. Spezieller Dank gilt dabei auch Martina Queck, meiner Bürokollegin und Mitdoktorandin, der auch kniffligste Fragen zu fachlichen, sprachlichen oder alltagsphilosophischen Aspekten nicht die Gelassenheit nehmen konnten.

Das Astrophysikalische Institut um Prof. Ralph Neuhäuser hatte wahrscheinlich als Ganzes einen sehr positiven Einfluss. Seien es die entspannenden, anregenden und amüsanten Teerunden, die gemeinsamen Filmabende, der Informationsaustausch mit der Beobachtergruppe und die praktizierte Basisdemokratie in den Institutsseminaren oder aber die ständige technische und logistische Unterstützung durch Jürgen Weiprecht und Monika Müller. Auch die gemeinsame Arbeit und die Diskussionen mit der Laborgruppe um Dr. Harald Mutschke möchte ich nicht missen.

Ferner danke ich dem Land Thüringen und der Deutschen Forschungsgemeinschaft für die finanzielle Unterstützung sowie auch der Universität Kobe/Japan, die mir die einmalige Gelegenheit gab, im Dezember 2006 an einer Winterschule zum Thema „Kleinkörper in Planetensystemen“ teilzunehmen.

Schließlich und vorallem möchte ich meinen Eltern danken, die mir Spaß und Interesse an Naturwissenschaft und Technik in die Wiege legten, meiner Schwester, deren Vorbild an Unabhängigkeit und doch Offenheit ich wohl nicht erreichen werde, sowie Manuela, die mich mit Geist und Humor durchs Leben begleitet und es schöner und farbenfroher macht.

Kurzfassung

Die vorliegende Arbeit behandelt Modelle der Größenverteilung und der räumlichen Verteilung des Materials in sogenannten zirkumstellaren Trümmerscheiben mit Rotationssymmetrie. Diese Scheiben, die als Überbleibsel der Planetenenstehung betrachtet werden, umkreisen Hauptreihensterne und bestehen aus Objekten von submikrometergroßem Staub bis möglicherweise hin zu Planetesimalen von einigen hundert Kilometern Durchmesser. Kollisionen und das Herauswerfen sehr kleinen Staubes durch den stellaren Strahlungsdruck führen bei ansonsten ungestörten Scheiben zu einem stetigen Ausdünnen.

Als Werkzeug zur Modellierung wurde dabei einerseits eine numerische Implementierung der kinetischen, statistischen Theorie verwendet. Andererseits wurden analytische Näherungen zur Verifizierung und Interpretation der erhaltenen Ergebnisse entwickelt.

Am Beispiel der Trümmerscheibe um Wega wurden erwartete typische Wellen in der Staubgrößenverteilung bestätigt sowie die Produktions- und verlustrate ungebundener Kleinstmeteoroiden bestimmt. Dabei wurde festgestellt, dass die andernorts empirisch ermittelte große Menge dieses vom Strahlungsdruck dezimierten kleinsten Staubes im Widerspruch steht zu den hier erhaltenen numerischen Ergebnissen sowie zu grundlegenden Argumenten.

Desweiteren konnte allgemeingültig die radiale Abhängigkeit der Dichte der von einem Planetesimalgürtel erzeugten Staubverteilung numerisch bestimmt werden. Diese wird von lose gebundenen Staubteilchen auf hochexzentrischen Bahnen dominiert.

Bezüglich der Langzeitentwicklung einer Trümmerscheibe konnte festgestellt werden, dass diese maßgeblich bestimmt wird vom Übergang der Population der großen und größten Planetesimale von der in der Wachstumsphase entstandenen Größenverteilung hin zum Gleichgewicht zerstörerischer Kollisionen. Relevant ist dies sowohl unmittelbar für den zeitlichen Verlauf der Masse und der Leuchtkraft des beobachtbaren Staubes als auch indirekt für die daraus gefolgerte Gesamtmasse einer Scheibe. Es konnte gezeigt werden das die gemachten Vorhersagen mit Beobachtungsstatistiken vereinbar sind.

Mittels Numerik und Analytik wurden Skalierungsregeln ermittelt. Diese Regeln beschreiben die Abhängigkeit der Kollisionszeitskalen von Scheibenmasse, Scheibenradius und mittlerer Bahnexzentrizität der Planetesimale.

Abstract

The subject of the work presented here has been models of the size distribution and the spatial distribution of the material in rotationally symmetric so-called debris disc around main-sequence stars. These discs, which are considered remnants of the formation of planetary systems, are an ensemble of objects from sub-micron-sized dust to planetesimals with diameters up to hundreds of kilometres. Mutual collisions and the ejection of very small dust by the stellar radiation pressure lead to a steady decay of otherwise unperturbed debris discs.

The models used are a numerical implementation of the kinetic theory of statistical physics as well as analytic approximations intended for verification and interpretation.

Exemplified by the debris disc found around Vega, the expected wavy size distribution in the dust regime is confirmed, and the production and loss rate is determined for the unbound micro-meteoroids that are ejected from the system due the stellar radiation pressure. It is concluded that the elsewhere proposed high abundance of those unbound grains is incompatible with the numerical results presented here and with more fundamental considerations.

A general conclusion is drawn concerning the radial distribution of dust produced by a planetesimal belt: it is dominated by barely bound grains on highly eccentric orbits.

The long-term evolution of a debris disc is shown to be dominated by the slow transition of the population of planetesimals from the size distribution set in the planet formation and growth phase to the steady-state size distribution defined by disruptive collisions. This transition is directly relevant to the temporal evolution of the observable dust masses and luminosities and indirectly to the deduced total disc masses. The developed models are compatible with observational statistics.

From numerics and analytics, scaling laws are derived for the dependence of the collisional timescales on the disc mass, the radial distance to the star, and the planetesimals’ orbital eccentricities.

1 Introduction

"Earth and moon and sun and stars,
Planets and comets with tails blazing,
All are there forever falling,
Falling lovely and amazing."

NICK CAVE, As I sat sadly by her side

The Big Picture

One of the most stereo-typed questions in life and for science is: are we alone in the universe? For a long time, this question was only subject to speculations since there was no answer to the related, less emotional question: is our solar system unique? With the increasing capabilities of detection techniques, more and more information about extrasolar systems has been gathered. This information needs to be categorized and interpreted along the lines of adequate theories.

The formation of stars and planetary systems is commonly attributed to the collapse of proto-stellar clouds. Once a central core has formed that is massive enough to ignite nuclear fusion, the largest fraction of the initial cloud mass is again blown away from the system. The remaining mass settles predominantly onto the central object, the star. Only a small mass fraction is neither accreted onto the star nor ejected but can form planetesimals, proto-planets, and eventually planets, carrying most of the system's angular momentum in their orbital motion.

When it comes to observations, a system's age or its evolutionary stage is an important issue. While the star can sustain a near-constant luminosity due to nuclear burning, the planets basically cool out and get fainter. The chances for a detection with direct imaging gradually decrease with time.

Here, the less and least massive objects in an evolved stellar system come into play. The left-over planetesimals, which were not consumed in planet formation within roughly the first ten million years, cease to grow further since relative velocities are no longer damped by gas but increased by gravitational perturbations. Collisions usually no longer lead to growth but to erosion or fragmentation. These planetesimals are negligible for the total mass budget but numerous. Still, they are outnumbered by the smaller rocks and smallest dust grains, which are continuously destroyed and replenished in mutual collisions. Through their sheer number, their total geometrical cross section supersedes that of planets: a single extrasolar dust grain cannot be resolved with a telescope, but a dusty disc is much more luminous than a compact, cool planet. And so, even though planets and planetesimals may remain hidden from an astronomer's eye, the traces they leave in the observable dust component stay present for giga-year timescales.

Debris Discs

Since the Infrared Astronomical Satellite (IRAS) discovered the excess infrared emission around Vega (Aumann et al. 1984), subsequent surveys with the Infrared Space Obseratory (ISO), the Spitzer Space Observatory, and other instruments have shown this so-called Vega phenomenon to be common for main-sequence stars. For instance, Spitzer has detected cold circumstellar dust around 15 to 20% of the observed sun-like stars of spectral types F, G, and K (Trilling et al. 2008; Hillenbrand et al. 2008). While, at higher ages, the reported average excesses are only slowly decreasing, significantly higher incidences of IR excess are found around younger stars as well as early-type stars (Su et al. 2006; Siegler et al.

2007) and marginally higher incidences around binary stars (Trilling et al. 2007). Of the less massive and luminous M stars, only for a fraction of a few percent excess has been detected, yet (Lestrade et al. 2006).

The observed excess is attributed to second-generation circumstellar dust, produced in a collisional cascade (Weissman 1984) from planetesimals and comets (Beust et al. 1989) down to smallest grains that are blown away by the stellar radiation. The dust material evolves then through a collisional cascade under the action of stellar gravity and radiation pressure forces. Thus, these so-called debris discs can be defined as gas-poor discs of second-generation dust grains and dust-producing parent bodies around main-sequence stars.

While the bulk of such a debris disc's mass is hidden in invisible parent bodies, the observed luminosity is dominated by small particles at dust sizes. Hence the studies of dust emission offer a natural tool to gain insight into the properties of planetesimal populations as well as planets that may shape them and, ultimately, into the evolutionary history of circumstellar planetary systems.

Stimulated by a growing bulk of observational data on debris discs, substantial effort has been invested into their theoretical studies. In recent years, statistics of, for example, the age dependence of the Vega phenomenon have been analysed and compared with simplified evolution models (Wyatt et al. 2007a,b).

Many authors also focused on modelling inner gaps and substructure found in most of the directly resolved debris discs, these features being attributed to the gravity of presumed planets (Wyatt et al. 1999; Ozernoy et al. 2000; Moro-Martín & Malhotra 2002; Quillen & Thorndike 2002; Wyatt & Dent 2002; Wilner et al. 2002; Kuchner & Holman 2003; Moran et al. 2004; Deller & Maddison 2005; Krivov et al. 2006; Freistetter et al. 2007, among others). A number of studies dealt with dynamics of discs at transitional phases between proto-planetary and debris discs, exemplified by β Pic, AU Mic, HR4796A and similar objects, which may have retained gas in moderate amounts, still sufficient to influence the dust dynamics (e.g., Takeuchi & Artymowicz 2001; Thébault & Augereau 2005). Kenyon & Bromley (2005) studied non-stationary processes in debris discs – consequences of major planetesimal collisions for the dust distributions. Ironically, these more particular cases receive more attention than the underlying "regular" debris discs.

Aims

This work is intended to identify the generic properties of debris discs, properties defined by mutual collisions among objects in the disc and by the interaction with the stellar radiation. To this end, debris discs are treated as a rotationally symmetric, statistical ensemble of objects with sizes from below 1 micrometre to tens of kilometres. The goal is to find out what kind of size distributions and spatial distributions of the disc material can be expected from theory, and how these distributions depend on the population of parent bodies, the parameters of the central star, the grain properties, and on time.

Chapter 2 provides an overview of the basic physical processes in debris discs, while the implementation of these processes in a kinetic model is described in Chapter 3.

Then, in Chapter 4, the size and the spatial distribution of a disc's dust component is discussed and specific application is made to the disc around the A-type star Vega.

The influence of the objects at the upper end of the size distribution, the planetesimals, is addressed in Chapter 5 where the long-term evolution of disc mass and dust mass in debris discs around G-type stars is studied. Comparison is made between numerical and analytic models as well as observational statistics.

Finally, a summary is given and the major conclusions are formulated in Chapter 6.

2 Background

2.1 Preliminaries

2.1.1 Size and Mass Distributions

The distribution of material over different object sizes or masses can be expressed in many ways, but there exist some frequently used standards. First of all, such distributions are commonly approximated or described by a power law, either piecewise or as a whole. For example, the number of objects per unit size (with s denoting the object radius) can be expressed as

$$\mathrm{d}N = n_{0,\mathrm{s}} s^{-p} \mathrm{d}s, \tag{2.1}$$

where $n_{0,\mathrm{s}}$ is the normalising constant, which can be obtained from, for instance, the integrated number

$$N \equiv \int n_{0,\mathrm{s}} s^{-p} \mathrm{d}s. \tag{2.2}$$

Based on equation (2.1), various alternative yet equivalent formulations are conceivable. An incomplete list of such *differential* distributions may be comprised of

$$\begin{aligned}
\mathrm{d}N(m) &\propto m^{-q}\mathrm{d}m \quad \text{with} \quad q = (p+2)/3, && (2.3)\\
\mathrm{d}N(s) &\propto s^{1-p}\mathrm{d}(\log s), && (2.4)\\
\mathrm{d}N(m) &\propto m^{1-q}\mathrm{d}(\log m), && (2.5)\\
m\mathrm{d}N = \mathrm{d}M(s) &\propto s^{3-p}\mathrm{d}s, && (2.6)\\
\mathrm{d}M(m) &\propto m^{1-q}\mathrm{d}m, && (2.7)\\
\mathrm{d}M(s) &\propto s^{4-p}\mathrm{d}(\log s), && (2.8)\\
\mathrm{d}M(m) &\propto m^{2-q}\mathrm{d}(\log m), && (2.9)
\end{aligned}$$

where it was assumed that the mass m is proportional to the size cubed: $m \propto s^3$. Starting from equation (2.2), one can also define a set of *cumulative* distributions:

$$\begin{aligned}
N(>s) &\propto s^{1-p}, && (2.10)\\
N(>m) &\propto m^{1-q}, && (2.11)\\
M(<s) &\propto s^{4-p}, && (2.12)\\
M(<m) &\propto m^{2-q}. && (2.13)
\end{aligned}$$

When it comes to terminology, confusion can occur. While a “size distribution” is commonly associated with a distribution over size range, in some cases intuition or common sense fail. A “mass distribution”, for example, can easily be mistaken for a distribution of mass in space. Therefore, please note that distributions over argument s are henceforth referred to as *size distributions*, those over m as *mass distributions* – regardless of whether it is $\mathrm{d}N$ or $\mathrm{d}M$.

2.1.2 Orbital Elements

In general, the position and velocity of an object are spanning three dimensions each, giving six dimensions in total. A cartesian set of coordinates is given by

$$\mathbf{k}' = \{\mathbf{r},\mathbf{v}\} = \{x,y,z;\dot{x},\dot{y},\dot{z}\} \tag{2.14}$$

whereas a distribution over orbital elements can be parameterized as

$$\mathbf{k} = \{a,e,I,\Omega,\omega,\theta\}. \tag{2.15}$$

Here, a denotes the semi-major axis, e the (numeric) eccentricity, I the inclination with respect to the plane of reference, Ω the longitude of the ascending node, ω the argument of the pericentre, and θ the true anomaly.

2.1.3 Units

The centimetre-gramme-second (cgs) unit system is used next to the standard SI units (metre, kilogramme, second). Conversions for common composite units are, for example,

$$\begin{aligned}
1\ \mathrm{g\ cm^{-3}} &= 10^3\ \mathrm{kg\ m^{-3}},\\
1\ \mathrm{erg} &= 10^{-7}\ \mathrm{J},\\
1\ \mathrm{erg\ g^{-1}} &= 10^{-4}\ \mathrm{J\ kg^{-1}}.
\end{aligned}$$

In addition, the following astronomical units are used where appropriate:

$$\begin{aligned}
1\,yr &\approx 3.156\times10^{7}\ \mathrm{s} \quad (\text{one year}),\\
1\,AU &\approx 1.496\times10^{11}\ \mathrm{m} \quad (\text{one astronomical unit}),\\
1\,L_\odot &\approx 3.85\times10^{26}\ \mathrm{W} \quad (\text{one Solar luminosity}),\\
1\,M_\odot &\approx 1.99\times10^{30}\ \mathrm{kg} \quad (\text{one Solar mass}),\\
1\,M_\mathrm{Jup} &\approx 1.90\times10^{27}\ \mathrm{kg} \quad (\text{one Jupiter mass}),\\
1\,M_\oplus &\approx 5.97\times10^{24}\ \mathrm{kg} \quad (\text{one Earth mass}),\\
1\,M_\mathrm{Moon} &\approx 7.35\times10^{22}\ \mathrm{kg} \quad (\text{one Lunar mass}).
\end{aligned}$$

2.2 Collisions

In contrast to protoplanetary discs, collisions in optically thin, gas-poor debris discs occur at high relative velocities ($\gtrsim$ 100 m s^{-1} to 1 km s^{-1}) and are, therefore, erosive or destructive and create smaller fragments. Removal of fine debris by stellar radiation pressure is the main loss "channel" of material in such systems. So the questions to be addressed are: when or how often do grains collide? and: what happens if they collide?

The first question deals with the probability that two (spherical) objects on Keplerian orbits come close enough to touch. This probability can be expressed as a product of a purely geometric factor Δ, describing the overlap of two orbits, the density of grains at the desired location in the space of orbital elements, the relative or impact velocity v_imp, and the cross section σ for the collision, which is basically $\pi(s_\mathrm{p}+s_\mathrm{t})^2$, where s_p and s_t are the radii of target and projectile, respectively (Krivov et al. 2005).

The answer to the second question depends on the physics of the impact and the fragmentation process. Collisions are usually classified according to the fate of the colliders. Diverse cases range from elastic collisions to totally inelastic ones, with and without fragmentation. The mutual impact energy is a common means of classifying the different scenarios. This impact energy is given by the colliders' masses and their relative velocity at impact

$$E_{\mathrm{imp}} = \frac{1}{2}\frac{m_{\mathrm{t}} m_{\mathrm{p}}}{m_{\mathrm{t}} + m_{\mathrm{p}}} v_{\mathrm{imp}}^2, \tag{2.16}$$

where the index "t" stands for "target" and "p" for "projectile", respectively. In a first approximation, average impact velocities can be estimated from the Keplerian velocity v_{k} and the effective/average eccentricity (and/or inclination) e:

$$v_{\mathrm{imp}} \approx e v_{\mathrm{k}}. \tag{2.17}$$

This Section gives an overview of possible outcomes of collisions.

2.2.1 Disruptive Collisions and Critical Specific Energy for Dispersal

A collision can be defined as disruptive if the largest remaining fragment has at most half the mass of the original parent body (see, e.g., Paolicchi et al. 1996). Based on that, a critical impact energy can be introduced:

$$E_{\mathrm{imp}} > E_{\mathrm{crit}} \tag{2.18}$$

for a collision to be disruptive. This threshold is determined by the internal binding forces and the amount of binding energy.

For forces that act only locally, like cohesion, a linear volume dependence seems reasonable. Having twice as much material to break up necessitates twice as much energy. Therefore, the critical specific energy for dispersal, Q_{D}^* was introduced in order to eliminate that volume or mass dependence. Like any other specific energy, it is related to the corresponding critical energy via

$$Q_{\mathrm{D}}^* = \frac{E_{\mathrm{D}}^*}{m}, \tag{2.19}$$

where m is the mass of the affected object. Using that notation, the target is disrupted on impact if

$$Q_{\mathrm{imp}} \geq Q_{\mathrm{D}}^*. \tag{2.20}$$

However, laboratory experiments with centimetre-sized targets (see, e.g., Fujiwara et al. 1977; Fujiwara 1986; Davis & Ryan 1990; Love et al. 1993) have shown that Q_{D}^* is not completely constant in this so-called strength regime but shows some dependence on target mass.

The impact experiments have also yielded an empirical functional dependence for the distribution of the fragments from a disruptive collision. One crucial parameter is the upper cut-off, i.e. the mass of the largest fragment, m_{x}:

$$\frac{m_{\mathrm{x}}}{m_{\mathrm{t}}} = \frac{1}{2}\left(\frac{m_{\mathrm{t}} Q_{\mathrm{D}}^*(m_{\mathrm{t}})}{E_{\mathrm{imp}}}\right)^c, \tag{2.21}$$

where m_{t} denotes the mass of the fragmented target. The slope is $c \approx 1.24$ for basalt (Fujiwara et al. 1977) and $c \approx 0.91$ for ice (Arakawa 1999). In contrast to the experimental results for c, Benz & Asphaug (1999) report the *lower* absolute values for basalt and the *higher* ones for ice: from their models, they derive

$$\frac{m_{\mathrm{x}}}{m_{\mathrm{t}}} = 0.5 - S\left(\frac{E_{\mathrm{imp}}}{Q_{\mathrm{D}}^* m_{\mathrm{t}}} - 1\right). \tag{2.22}$$

With the linear slope $S = 0.35 \ldots 0.6$ around $E_{\mathrm{imp}} \approx Q_{\mathrm{D}}^* m_{\mathrm{t}}$, this corresponds to $c \approx 2S = 0.7 \ldots 1.2$ around $Q_{\mathrm{imp}} \approx Q_{\mathrm{D}}^*$.

From laboratory (Fujiwara & Tsukamoto 1980) and from numerical simulations (Durda et al. 2007), it has been concluded that the value of m_{x}, like the whole outcome of a collision, depends on the impact angle of the projectile with respect to the target's surface. Therefore, modellers (Davis et al. 1985; Petit & Farinella 1993; Thébault et al. 2003) suggest a correction of the mass of the largest fragment by a factor of $4^{-1/1.24} = 0.327$ in order to account for an average impact angle.

Below the largest fragment's mass, the experimental results indicate a bimodal power-law distribution of fragments with slopes $p_1 = 3\ldots 10$ and $p_2 = 1.6\ldots 3.7$ (Davis & Ryan 1990), for larger and smaller projectiles, respectively. The break between the two modes is at masses $\sim 10^{-2} m_\mathrm{t}$. The slope p_1 shows an especially strong dependence on the relative strength of the target, being steeper for stronger targets. Davis & Ryan (1990) combined their data with that of Takagi et al. (1984) and derived empirical power laws for the slopes b_1 and b_2 of the cumulative mass distribution as a function of the mass of the largest fragment:

$$b_1 = 0.47 \left(\frac{m_\mathrm{x}}{m_\mathrm{t}}\right)^{-0.53}, \tag{2.23}$$

$$b_2 = 0.18 \left(\frac{m_\mathrm{x}}{m_\mathrm{t}}\right)^{-0.49}. \tag{2.24}$$

Using $p = 3(b+1) - 2$, this corresponds to slopes p_1 and p_2 of the (non-cumulative) size distribution given by

$$p_1 = 2.3 \left(\frac{m_\mathrm{x}}{m_\mathrm{t}}\right)^{-0.40} \quad \text{for } p_1 \approx 4, \tag{2.25}$$

$$p_2 = 1.4 \left(\frac{m_\mathrm{x}}{m_\mathrm{t}}\right)^{-0.29} \quad \text{for } p_2 \approx 2.5. \tag{2.26}$$

Note that the power-laws for p_1 and p_2 result in a slightly different functional dependence when solved for $m_\mathrm{x}/m_\mathrm{t}$ than the power-laws for b_1 and b_2 do. Equations (2.25) and (2.26) lead to exactly the same $m_\mathrm{x}/m_\mathrm{t}$ as (2.23) and (2.24) *only* at the (arbitrarily chosen) reference points $p_1 = 4$ ($b_1 = 1$) and $p_2 = 2.5$ ($b_2 = 0.5$). Benz et al. (1994) performed numerical simulations for similar set-ups and likewise found a bimodal distribution, although with less pronounced differences between the two modes.

Takagi et al. (1984) state an additional feature: a third regime for even smaller fragments. For that regime, i.e. for fragment masses below $10^{-3} m_\mathrm{t}$, they report negative slopes $p_3 = 2.5\ldots 4.0$. This range of slopes is much narrower than that for p_1 and p_2. Results from impact experiments with equal initial set-ups but different distributions in regimes 1 and 2 indicate a reconvergence of the distributions towards regime 3 (Takagi et al. 1984, their Figures 5 and 8). Fujiwara et al. (1977) have come to a similar conclusion, although their slope p_3 is even more narrowly confined to the range $p_3 = 3.4\ldots 3.6$. These authors ascribe the transition from regime 3 to regime 2 at sizes of around 1 mm to "the pressure at which the change from plastic to elastic flow occurs in the basaltic target."

Thébault et al. (2003) and Thébault & Augereau (2007) incorporated the bimodal distribution into their model of collisional outcomes, leaving the ratio between the two slopes as a free parameter. However, they decided not to use the empirical relations in equations (2.25) and (2.26), but rather fixed p_1/p_2 and numerically calculated the absolute values of p_1 and p_2 from the mass ratio $m_\mathrm{x}/m_\mathrm{t}$ and the assumption that the cumulative distribution equals unity at the size of the largest fragmemt, i.e. there is one and only one largest fragment. Nevertheless, their results indicate that the ratio p_1/p_2, which is crucial for the outcome of an individual impact, has only little influence on the overall statistics. (Section 5.4.7 contains another aspect of how little relevance the fragment size distribution has on the collisional equilibrium.)

The work of Tanga et al. (1999) and Campo Bagatin & Petit (2001) has shown that geometry can put constraints on fragment size distributions. Especially for barely catastrophic collisions with $m_\mathrm{x} \approx 0.5 m_\mathrm{t}$, the few largest fragments are overabundant when compared to the extrapolation of the distribution of the many smaller ones. For so-called supercritical collisions, with impact energies well above the disruption threshold, there is no such effect. Moreover, in this case, the largest fragments are *underabundant* when compared to the extrapolation from smaller sizes. The result is the steep slope p_1. Figures 6 and 7 of Takagi et al. (1984) illustrate the transition from subcritical, to barely catastrophic, to supercritical collisions. Durda et al. (2007) report a similar effect for asteroidal objects. As a result, with increasing impact energy, the *average* fragment size decreases slower than the *maximum* fragment size.

With increasing object mass, self-gravity becomes more and more important, and from object sizes of around 1 km on, it is the dominating binding force. Since gravity is a long-distance force, the critical specific energy cannot be expected to be constant with respect to object mass/volume, even in the most basic approximation. For example, the total specific energy needed to completely disperse a homogeneous sphere that is gravitationally bound is proportional to $m^{2/3}$, where m is the object's mass. Detailed hydrodynamical models of shattering, dispersal, and reaccumulation (Nolan et al. 1996; Benz & Asphaug 1999; Michel et al. 2001, 2002) have found a dependence $Q_\mathrm{D}^* \propto m^b$ with $b = 0.4\ldots0.5$. Since the gravitational binding energy is a lower boundary in this context, this shallower slope indicates that the fraction of energy consumed in deformation or carried away by fast ejecta is reducing towards larger targets (Davis et al. 1979; Melosh & Ryan 1997).

In addition, the hydrocode results show a difference between the *largest intact fragment* and the *largest remnant*: the mass of the former is set in the shattering phase and mostly determined by material strength, while the mass of the latter is an outcome of the subsequent phase of gravitational reaccumulation. Consequentially, several authors introduce a critical specific energy for shattering, Q_S^*, which equals Q_D^* in the strength-only regime but is well below Q_D^* in the gravity regime. As a result, the largest remnants from disrupted planetesimals are predicted to be "rubble piles", agglomerates of boulders and rocks. These pre-shattered rubble pile objects react differently on an impact than intact, homogeneous objects would: (Asphaug et al. 1998) state that the porosity damps the shockwave and shields regions that are distant from the impact area.

Another aspect is the mass dependence of the velocity of ejecta, $v(m)_\mathrm{ej}$. Nakamura & Fujiwara (1991) report $v_\mathrm{ej}(m) \propto m^\beta$ with $\beta \approx 1/6$. In consequence, mid-sized fragments might fall back more easily while small fragments can escape. As long as collisions are studied by means of Q_S^*, the gravitational reaccumulation of material can be described, following, e.g., Stern & Colwell (1997). However, the prescription with Q_D^* already includes the process of reaccumulation; no correction is necessary.

Combining the "strength regime" and the "gravity regime", Benz & Asphaug (1999) compile a functional dependence of Q_D^* on the object mass that is composed of two power laws with a turn-over at sizes of around 100 m:

$$Q_\mathrm{D}^*(s) = A_\mathrm{s}\left(\frac{s}{1\,\mathrm{m}}\right)^{3b_\mathrm{s}} + A_\mathrm{g}\left(\frac{s}{1\,\mathrm{km}}\right)^{3b_\mathrm{g}}. \tag{2.27}$$

The authors state $A_\mathrm{s} = 0.6\ldots1.7\times10^7$ erg g^{-1}, $b_\mathrm{s} \approx -0.12$, $A_\mathrm{g} = 0.5\ldots0.9\times10^7$ erg g^{-1}, and $b_\mathrm{g} \approx 0.45$ for basalt as well as $A_\mathrm{s} = 0.3\ldots0.9\times10^7$ erg g^{-1}, $b_\mathrm{s} \approx -0.12$, $A_\mathrm{g} = 0.17\ldots0.22\times10^7$ erg g^{-1}, and $b_\mathrm{g} \approx 0.41$ for ice.

In addition to the mass dependence, Benz & Asphaug (1999) noticed that the critical energy is slightly velocity-dependent, making the concept of a "critical specific energy" even more questionable. Both parameters of an impactor, mass and velociy, influence the outcome, and a combination into one parameter, the kinetic energy, is only an approximation. However, for the purpose of this work, the velocity dependence is considered only implicitly as part of the impact energy.

2.2.2 Cratering Collisions

Then, the logically successing step towards lower impact energy is inelastic deformation and ejection of material. In these so-called cratering collisions, the bulk of at least one of the colliders stays bound or even intact, but some fragments are released. The results of Thébault et al. (2003) show that, for the inner part of the disc around β Pictoris, catastrophic collisions are overall dominating but cratering is very important for millimetre-sized particles, i.e. particles sizing from 100 µm to 1 cm.

In impact experiments with targets in the centimetre-size range (e.g., Marcus 1969; Fujiwara et al. 1977; Fujiwara 1986; Davis & Ryan 1990; Love et al. 1993; Koschny & Grün 2001a,b; Hiraoka et al. 2007) the dependence of the distribution of fragments on impact energy and material parameters has been studied. The projectiles used were significantly smaller than the targets, measuring between tens of micrometres and a few millimetres in diameter. Several results were obtained. First, for small craters, the total mass of the excavated material, m_crat, roughly follows a power-law dependence on the impact energy:

$$\frac{m_{\mathrm{crat}}}{\rho_{\mathrm{t}}} = \alpha \left(\frac{E_{\mathrm{imp}}}{1\ \mathrm{erg}} \right)^{\gamma}, \tag{2.28}$$

where α is the so-called crater excavation coefficient. The target's bulk density is denoted by ρ_{t}, and the empirically found value for the exponent is $\gamma \approx 1.23$. Marcus (1969) and Koschny & Grün (2001a) give values for α, roughly ranging from 10^{-7} cm^3 to 10^{-9} cm^3. Second, for large craters with sizes of the order of the target, Wyatt & Dent (2002) and Thébault & Augereau (2007) adopt

$$\frac{m_{\mathrm{crat}}}{m_{\mathrm{t}}} = 0.5 \left(\frac{E_{\mathrm{imp}}}{Q_{\mathrm{D}}^{*} m_{\mathrm{t}}} \right)^{\varepsilon} \tag{2.29}$$

with $\varepsilon = 1$. The model results of Benz & Asphaug (1999) (cf. Eq. 2.22) now read

$$\frac{m_{\mathrm{crat}}}{m_{\mathrm{t}}} = 0.5 + S \left(\frac{E_{\mathrm{imp}}}{Q_{\mathrm{D}}^{*} m_{\mathrm{t}}} - 1 \right) \tag{2.30}$$

again with slope $S = 0.35 \ldots 0.6$ or $\varepsilon \approx 2S = 0.7 \ldots 1.2$ around $Q \approx Q_{\mathrm{D}}^{*}$. Third, the distribution of fragments can be described by a single power law up to mass m_{x}. The index of that power-law fragment-size distribution is $\eta \approx 3.5$ (Fujiwara et al. 1977). And fourth, assuming that the distribution of large fragments holds up to *the* largest one, the mass of this largest fragment is given by

$$m_{\mathrm{x}} = 1 + \frac{1}{3} (1 - p)\, m_{\mathrm{crat}} \overset{p=3.5}{\approx} \frac{1}{6} m_{\mathrm{crat}}. \tag{2.31}$$

Thus, it is proportional to $E_{\mathrm{imp}}^{\gamma}$, too (Petit & Farinella 1993; Thébault et al. 2003).

Koschny & Grün (2001b) found an additional feature in the size distribution when they studied targets mixed of ice and silicate: an overabundance of particles with sizes of 10–20 µm. They ascribe this feature to the unfragmented silicate inclusions that were formerly embedded in the mainly icy targets. In a more general context, the inclusions represent “unbreakable” monomeres that may determine the fragment distribution at their size regime. At larger scales, the monomeres are averaged over. However, the effect has not been studied further and is not implemented in typical models.

2.2.3 Rebound and Agglomeration

Below a certain energy threshold, the colliders rebound from each other. They are able to escape from their mutual binding potential and are separated again. Since head-on bouncing collisions require reversion of the relative linear momenta of the objects, the stress on the objects is rather high.

The final step towards ever lower energies is done when the colliders stick to each other due the binding forces. This criterion for the relative velocity is usually met in the gaseous, damped protoplanetary discs. In that regime, objects tend to agglomerate material and grow. For micron-sized silicon spheres, the transition between the two regimes occurs at relative velocities of around 1–10 m s^{-1} (e.g, Poppe et al. 2000; Blum et al. 2000).

2.3 Interaction with Radiation

2.3.1 Scattering, Absorption and Thermal Emission

Radiation acts in different ways on debris discs and especially on the dust. First of all, the stellar radiation heats the grains. Electromagnetic energy that is intercepted, but not scattered, is absorbed and dissipated into thermal energy and finally re-emitted with a characteristic spectrum. In general, the spectra for both absorption and emission are determined by the configuration of the internal energy levels of an object. An infinitely extended homogeneous, isotropical (black) body would absorb at unit probability and emit a classical Planck spectrum. In contrast, a real object may be partly crystalline, irregularly shaped,

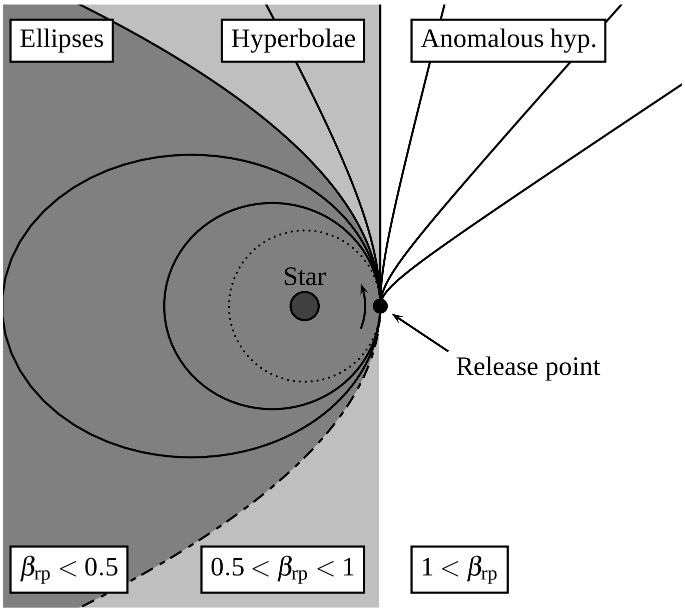

Figure 2.1: Three possible types of orbits of dust particles under the combined action of stellar gravity and direct radiation pressure. For illustrative purposes, grains are assumed to be released from a circular orbit (dotted). The ratio between radiation pressure and gravity is denoted by β_{rp}.

conducting, of inhomogeneous composition, and of rather small extent, compared to the wavelength of interest.

Following, e.g., Bohren & Huffman (1983), two general parameters can be used to describe the interaction of a particle with radiation: the absorption cross section C_{abs} and the scattering cross section C_{sca}. These cross sections are defined as incidenting flux over absorbed and scattered flux, respectively. They depend on the wavelength of the incident light and on the particle, e.g., its structure and orientation. The cross section for extinction is the sum of both: $C_{ext} = C_{abs} + C_{sca}$. One usually defines related efficiencies as $Q = C/\sigma$, where σ denotes the particle's geometrical cross-sectional area.

Knowledge of the phase function, which describes the angular intensity distribution (in the far-field) of the scattered light, is important for the interpretation of measurements of scattered light (e.g., Leinert et al. 1998; Absil et al. 2006, for applications) and polarisation of dust (e.g., Krivova et al. 2000).

The relative momentum transfer from the starlight to a particle is described by the raditation pressure efficiency:

$$Q_{pr} = Q_{ext} - gQ_{sca} \qquad (\text{with } Q_{ext} = C_{ext}/\sigma \text{ and } Q_{sca} = C_{sca}/\sigma), \tag{2.32}$$

where $g = \langle\cos\theta\rangle$ is called asymmetry parameter, distinguishing between forward-scattering ($0 < g < 1$) and back-scattering ($0 > g > -1$).

One of the basic approaches for the calculation of the above quantities is the so-called Mie theory, named after Gustav Mie (1868–1957). Mie theory can exactly describe the interaction of radiation with homogeneous isotropical spheres. It is widely used where only radiation pressure efficiencies or rough emission features are sought. However it naturally fails to accurately reproduce spectra emitted from, e.g., crystalline matter, where resonant lattice vibrations depend on particle size, orientation, etc. This becomes important when the composition of circumstellar (or interstellar) dust is studied (e.g., Lisse et al. 2007).

A widely used set of (synthetic) optical constants is that for the amorphous so-called Astronomical Silicate (Laor & Draine 1993; Draine 2003). Laboratory measurements of diverse astronomically relevant materials are compiled in the Heidelberg-Jena-St. Petersburg Database of Optical Constants (HJPDOC, Henning et al. 1999).

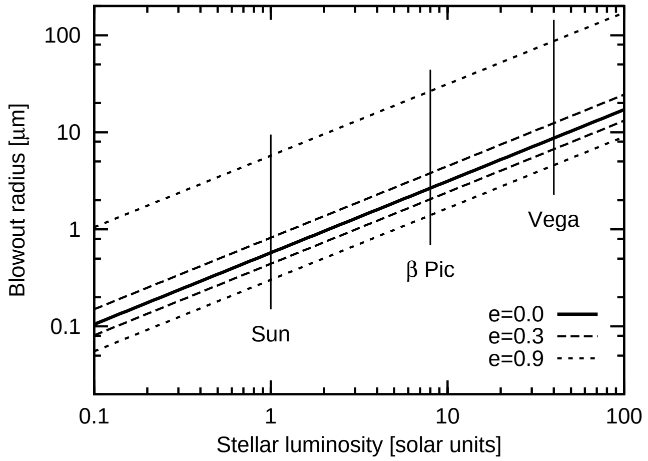

Figure 2.2: Grain radius that separates particles in bound and hyperbolic orbits, as a function of the star's luminosity (assuming dust bulk density of 2 g cm^{-3}, a unit radiation pressure efficiency, and a standard mass-luminosity $L \propto M^{3.8}$ relation for main-sequence stars). Different linestyles are for different typical eccentricities of parent bodies. Grains between two lines of the same style may be in both types of orbits, depending on where between the periastron and apastron they are ejected. The upper lines separate bound and unbound orbits for ejection at the periastron and the lower ones correspond to ejection at the apastron.

2.3.2 Influence on Orbital Motion

Once the resulting net force on a particle is known, it can be compared to the gravitational pull from the star. The ratio between the norms of those two forces is usually called β ratio and denoted as

$$\beta_{\mathrm{rp}} = \frac{|F_{\mathrm{rp}}|}{|F_{\mathrm{grav}}|}. \tag{2.33}$$

That ratio depends on the size, mass, shape, and composition of the particle, as well as on the central star's SED, as determined by its spectral type, luminosity class, and mass. The radiation pressure on a (non-moving) particle is directed radially outward and, like gravity, has a norm that is proportional to r^{-2}, where r is the distance to the star. For that reason, β is independent of r and we can write

$$F_{\mathrm{rp}} = -\beta_{\mathrm{rp}} F_{\mathrm{grav}}. \tag{2.34}$$

Assuming spherical particles and a wavelength-averaged, size-independent radiation pressure efficiency $\langle Q_{\mathrm{pr}} \rangle$, a handy approximation to β is given by Burns et al. (1979):

$$\beta_{\mathrm{rp}} = \frac{3L\langle Q_{\mathrm{pr}} \rangle}{16\pi \mathrm{G} M c s \rho} = 0.574 \cdot \frac{L}{L_\odot} \cdot \frac{M_\odot}{M} \cdot \frac{1\ \mathrm{g/cm^3}}{\rho} \cdot \frac{1\ \mu\mathrm{m}}{s}. \tag{2.35}$$

As long as the particles are opaque and large compared to the wavelength, geometrical optics is a good representation and $\langle Q_{\mathrm{pr}} \rangle \approx 1$ is a good estimate. Equation (2.35) shows the obvious proportionality to the stellar luminosity and the inverse proportionalities to stellar mass as well as grain radius and bulk density.

Taking a closer look at the resulting total force,

$$F_{\mathrm{total}} = F_{\mathrm{rp}} + F_{\mathrm{grav}} = -\frac{\mathrm{G}M(1-\beta_{\mathrm{rp}})}{r^2}, \tag{2.36}$$

we find that the original form of Newton's law of attraction can be restored by substituting $M(1-\beta_{\mathrm{rp}}) \mapsto M'$. A particle moves as if a central object of mass M' attracts it. As a consequence, the possible orbits are ellipses, classical hyperbolae, and anomalous hyperbolae. The latter occur if the radiation pressure overpowers gravity, and the particles are accelerated outward while leaving the system. In that case, β_{rp} is, by definition, greater than unity. Figure 2.1 illustrates the different types of orbits.

However, in the regime of Rayleigh scattering, the effective absorption cross sections become proportional to geometrical volume instead of geometrical cross section. Therefore, Q_{abs} becomes proportional to particle size and the β_{rp}-ratio constant. For late-type stars, this leads to radiation pressure being too weak to remove material.

Borrowing the terminology from solar system studies (Zook & Berg 1975), dust grains in bound and unbound orbits will be called α-meteoroids and β-meteoroids, respectively. The velocity of the radiation-supported orbital motion is related to the pure gravitational Keplerian velocity by $v_{\text{rp}} = \sqrt{1-\beta_{\text{rp}}}v_{\text{K}}$.

2.3.3 Poynting-Robertson Drag

The above described treatment of stellar radiation pressure is accurate if the object does not move with respect to the source of light. Once objects are considered whose lifetimes are sufficiently long, more subtle effects like the so-called Poynting-Robertson (P-R) drag become important. That drag force was proposed by Poynting (1903) and decribed by Robertson (1937) in terms of special relativity. A qualitative explanation of the P-R drag goes as follows. The radial component $\dot{r}$ of an object's orbital motion leads to a doppler shift of the frequency or the *energy per incidenting photon*. The radiation seems blue-shifted when approaching the star and red-shifted when receding. In addition, the *number of incidenting photons* per unit time changes when the object moves at velocity $\mathbf{v}$. The object feels a "headwind" of photons. Inseparable as they are, these two contributions add to the pure radiation pressure force $\mathbf{F}_{\text{rp}}$ to give (to terms of order v/c; see, e.g., Burns et al. 1979)

$$\mathbf{F}_{\text{rad}} = |\mathbf{F}_{\text{rp}}| \left[\left(1 - \frac{\dot{r}}{c}\right) \hat{\mathbf{r}} - \frac{\mathbf{v}}{c} \right]. \tag{2.37}$$

Another heuristic explanation for P-R drag stresses the fact that a radiator that produces an isotropic radiation field in its own rest-frame will be seen having an anisotropic field from the point of view of a moving observer. This anisotropy is claimed to cause an effective force on the radiatior (Burns et al. 1979). However, this reasoning is unphysical since the choice of the observer's rest-frame is arbitrary. The radiating object cannot be decelerated with respect to *every* conceivable rest-frame, and therefore it is affected by none.

Like the direct radiation pressure, the P-R drag force is proportional to β_{rp}, which leads to a size-dependent collisional lifetime $T_{\text{P-R}} \propto s$. In conjunction with this size dependence, different regimes are conceivable: for sufficiently diluted discs like the Zodiacal Cloud, P-R drag can dominate up to a particle size of hundreds of micrometres (e.g., Grün et al. 1985, 2001). Above that limit, collisional lifetimes are shorter. However, the debris discs observed yet are supposed to be too massive to be significantly influenced by P-R drag at any particle size (Wyatt 2005).

2.4 Other Effects

2.4.1 Planetary Perturbations and Self-Stirring

Planets can affect debris discs at every evolutionary stage. Starting in the planet formation phase, protoplanets and planets sculpt debris discs and limit their spatial extent: by opening a gap in the surrounding protoplanetary cloud and by gravitational stirring and ejection of nearby material. In addition, self-stirring due to large planetesimals and oligarchs can stop the growth phase and initiate the collisional cascade (Ida & Makino 1993; Stewart & Ida 2000; Rafikov 2003; Quillen et al. 2007). Scattering of large amounts of disc material due to a rapid relocation of Neptune's orbit may explain the solar late heavy bombardment 3.8 Gyr ago. The cause might be Saturn crossing the 2:1 resonance with Jupiter (Gomes et al. 2005). In combination with slow migration (e.g., Ida et al. 2000; Gomes et al. 2004) associated with resonance trapping of planetesimals, dynamical "heating" of debris discs becomes important. Resonant scenarios are invoked, e.g., for clumps in the discs around ε Eridani (Greaves et al. 2005; Poulton et al. 2006; Krivov et al. 2007) and Vega (Wyatt 2003, 2006), and for the solar EKB (e.g., Hahn & Malhotra 2005). Furthermore, planets are required for scenarios that explain warped discs (Mouillet et al.

1997) or cometary dust production and falling evaporating bodies (Beust & Morbidelli 2000). However, the statistics of systems with planets *and* debris discs is still poor, impeding assumptions about average influences and correlations. Therefore, only particular systems have been assessed in that way, yet.

2.4.2 Cometary Activity

Star-light-induced evaporation of icy volatiles from and from below the surface of a comet results in gaseous outflows that can drag dust grains along with them. The efficiency of that erosion depends on the size of the comets' nucleus, the mixing ratio of ice and dust, the intensity of the stellar radiation at the given distance, and the individual surface properties of the comet.

The total dust production rate of short- and long-period comets in the inner solar system is estimated to several 10^5 to a few 10^6 g s^{-1} (Leinert & Grün 1990). The size distribution of the dust released from comets is well-fitted by a power-law s^{-p} with a slope $p = -3.4 \pm 0.4$ (Fulle et al. 1997; Epifani et al. 2001; Jorda et al. 2007), and the dominating material is presumably a variety of more or less processed silicates (e.g., Leinert & Grün 1990), forming grains with a porosity that presumably increases with grain size (e.g., Le Sergeant d'Hendecourt & Lamy 1980; Hadamcik & Levasseur-Regourd 2003). Grün & Svestka (1996) pointed out that direct injection of small dust is overlayed by the release of, e.g., metre-sized fragments which are slowly ground down and represent a potentially important mass reservoir for the zodiacal cloud.

2.4.3 Wind Drag

Wind drag acts very similar to P-R drag, except that the wind particles are streaming at speeds well below the speed of light. To be more precise, the solar wind streams outward at $v_{\rm wind} = 300\ldots800$ km s^{-1} and transports $\dot{M}_\odot = 2\times10^{-14}\,M_\odot$ yr^{-1} $= 1.3\times10^{12}$ g s^{-1} (e.g., Allen 1973). In accord with the description of radiation pressure, the ratio between the stellar wind pressure and the stellar gravity can be denoted as

$$\beta_{\rm wp} \equiv \frac{|\mathbf{F}_{\rm wp}|}{|\mathbf{F}_{\rm grav}|}, \tag{2.38}$$

where

$$\beta_{\rm wp} = \frac{3\dot{M}_* v_{\rm wind}}{16\pi G M_* \rho s}, \tag{2.39}$$

assuming an effective cross section equal to the geometrical cross section $\sigma = \pi s^2$. For typical wind speeds and stellar mass loss rates, the direct wind pressure is by three orders of magnitude lower than the direct radiation pressure.

However, wind *drag* scales with $\beta_{\rm sw} c/v_{\rm sw}$, where the ratio $c/v_{\rm sw}$ can compensate those three orders of magnitude. Thus, the total force that stellar wind exerts on a particle is given by

$$\mathbf{F}_{\rm wind} = |\mathbf{F}_{\rm wp}| \left[\left(1 - \frac{\dot{r}}{v_{\rm wind}}\right)\hat{\mathbf{r}} - \frac{\mathbf{v}}{v_{\rm wind}} \right], \tag{2.40}$$

where

$$\frac{|\mathbf{F}_{\rm wp}|}{|\mathbf{F}_{\rm rp}|} = \frac{\beta_{\rm wp}}{\beta_{\rm rp}}. \tag{2.41}$$

Gustafson (1994) estimates a ratio between wind drag and P-R drag of typically around 30 percent for the solar system. For more active, young, or late-type stars, higher ratios are expected due to higher mass-loss rates: for the K2V star ε Eridani, Wood et al. (2002) find mass-loss rates about a factor of 30 above the solar value. AU Microscopii, an M1V star, is another example (Augereau & Beust 2006; Strubbe & Chiang 2006).

2.4.4 Electric Charge

Electric charge and the Lorentz force induced by stellar or planetary magnetic fields are most important for very small grains, where the ratio of surface (charge) and mass is higher. Assuming a balance between the emission of photoeletrons and secondary electron, and the capture of electrons and ions from the stellar wind, the typical grain surface potential is of the order of 3 to 10 volts (Wyatt 1969; Horányi 1996; Kimura & Mann 1998) for the solar system, approximately independent from grain size and composition. However, the relative strength of the different charging mechanisms plays an important role: for example, in the environment of Jupiter and Saturn, particles with a negative surface charge and potential are expected (see, e.g., Horányi 1996) and have been detected by the Cosmic Dust Analyzer aboard the Cassini spacecraft (Kempf et al. 2006). Due to the roughly size-independent surface potential, the Lorentz acceleration is inversely proportional to the squared particle size. Thus, it is negligible for particles larger than 10 µm and important for particles of 0.1 µm and below (Leinert & Grün 1990). For the interaction of possibly colliding dust grains in a debris disc, the electric charge is unimportant – unless the interaction with small, unbound grains becomes important like in the case of very dense discs where dusty avalanches can occur (e.g., Artymowicz 1997). To give an example, the electrostatic potential energy to overcome for two grains of 1 µm, a surface potential of 10 volts, and a bulk density of 3 g cm^{-3} equals the kinetic energy for a collision at the rather low relative speed of 1 m s^{-1}.

2.5 The Solar System

Although hundreds of extra-solar planetary systems are already known, that sheer number cannot hide the fact that the best-studied example is, of course, still the solar system. With its more or less bright and prominent planets and comets, the diffuse zodiacal cloud, as well as main-belt asteroids and the distant Trans-Neptunian Objects (TNOs), the solar system is a rich source for data and a hard benchmark for models.

2.5.1 The Edgeworth-Kuiper Belt

The first, speculative ideas about the existence of material beyond the orbits of Neptune or Pluto were formulated by Edgeworth in 1943 and refined in 1949. Independently, Kuiper suggested the same in 1951 but did not present solid predictions, either.

Nevertheless, it was not until the 1990s that Jewitt & Luu (1993) discovered the first object belonging to the so-called Edgeworth-Kuiper Belt (EKB) and around one thousand more have been found since then. With respect to their individual orbits, the EKB objects (EKBOs) can be grouped into four main categories (see, e.g., Delsanti & Jewitt 2006). (1) The defining property of *resonant objects* is their angular motion being locked to a commensurability with Neptune's motion. Accordingly, they are trapped in defined ranges of semi-major axes. For example, Pluto at $a = 39.5$ AU is the archetypical member of the sub-group called Plutinos, which are locked in 3:2 resonance with Neptune, performing 2 revolutions while Neptune performs 3. (2) The *classical Kuiper belt* is a group of non-resonant objects with semi-major axes predominantly in between 40 AU (the 3:2 resonance with Neptune) and 48 AU (the 2:1 resonance). The group is bimodal, consisting of a dynamically "cold" population with inclinations below 4° and a "hot" population of inclinations up to 40° or higher. The sub-group of "cold" objects shows a stronger reddening in the reflectance spectra, indicative of a different origin or evolution. (3) *Scattered objects* orbit the sun on highly eccentric orbits with perihelia at 35 to 40 AU. Their current state is attributed to slow scattering by Neptune (Duncan & Levison 1997; Morbidelli et al. 2004) with individual residence times of around 50 Myr before they are transported inward or further outward. (4) The population of *detached objects*, which form the *extended scattered disc*, is characterized by perihelia beyond the influence of Neptune. Possibly, a passing star has been involved in the formation of that "group" (Morbidelli & Levison 2004), which had only two known members in 2006.

With a radius of roughly 1200 km, (136199) Eris and (134340) Pluto, formerly known as planet Pluto, are the biggest Trans-Neptunian Objects found so far. The observed size distribution is severely biased by the apparent object magnitude decreasing with distance. Therefore, objects with sizes down to some tens of kilometres (e.g., Delsanti & Jewitt 2006) have been discovered only in the innermost regions of the EKB. Jewitt et al. (1998) give 0.1 Earth masses as an upper limit for the total mass. Trujillo et al. (2001) report the size distribution of planetesimals to follow a size-dependent power law s^{-p} with $p = 4^{+0.6}_{-0.5}$ and a total mass of 0.03 Earth masses. The results by Bernstein et al. (2004) indicate a shallower slope ($p \approx 3$) for sizes below 50–100 km, a steeper slope ($p \approx 5$) for larger objects, and a total mass of 0.01 Earth masses in the classical Kuiper belt. The mass of the more extended exited population and the Plutinos is also roughly estimated to a total of only ≈ 0.03 Earth masses with Pluto alone accounting for already 10% of this mass (Trujillo et al. 2001; Bernstein et al. 2004). Donnison (2006) derives power-law indices of $p = 4.1 \pm 0.2$ for the classical belt, $p = 3.3 \pm 0.4$ for the Plutinos, and $p = 3.0 \pm 0.3$ for the scattered disc.

Since features from various ices have been detected for several EKBOs (e.g, Pluto: Owen et al. 1993), these objects are assumed to be composed of ice and rock, with the latter accounting for two thirds of the mass and, accordingly, a bulk density of 2 to 3 g cm^{-3} (Delsanti & Jewitt 2006).

Since planetesimals inevitably collide occasionally with each other, the Kuiper-belt region must contain dusty debris as well. However, the predicted dust densities are below the current observational limits (Backman et al. 1995). Likewise, in-situ measurements like those performed by Pioneer 10 and 11 (e.g., Humes 1980; Dikarev & Grün 2002) and Cassini spacecraft (Altobelli et al. 2007) provide too small a data set to allow for stringent reduction and conclusion, although Landgraf et al. (2002) deduce a dust (<0.1 g) production rate of 5×10^7 g s^{-1}, evoked by collisions among EKBOs. Moreover, the Kuiper belt is the source of the short-period comets and, therefore, of a fraction of the interplanetary and zodiacal dust (Duncan et al. 1988).

2.5.2 Interplanetary Dust and the Zodiacal Cloud

In the interplanetary space and the inner solar system, the dust detections are much clearer. The best example is the long-known zodiacal light, sunlight scattered from dust particles. From a wealth of observtional data (Leinert et al. 1998) on this scattered light (integrated over the line of sight), constraints on the radial and vertical particle density distribution and on the size distribution have been derived. These observations have been accompanied by in-situ measurements aboard space probes like Helios 1 and 2, Galileo, Ulysses, the Pioneers, Cassini etc. (see, e.g., Leinert & Grün 1990; Grün et al. 2001; Mann et al. 2006, for reviews)

From the analysis of data gathered by the Helios Space Probes, Leinert et al. (1981) derived a mid-plane density of the zodiacal cloud that follows $r^{-1.3}$. The according surface number density would follow $r^{-0.3}$ for an unflared disc. From the same Helios data set and from lunar microcrater records (see, e.g., Schneider et al. 1973; Fechtig et al. 1974; Le Sergeant d'Hendecourt & Lamy 1980), a size distribution has been derived. A clear break between the populations of unbound β- and bound α-meteoroids was found to occur at sizes of around 1 to 5 µm, with a relative depletion of β-meteoroids by 2 to 3 orders of magnitude. The dominating particle size in terms of cross section and brightness is 10 to 100 µm. The observed features in the size distribution can be reproduced with models for a collisional equilibrium under the influence of Poynting-Robertson drag (Le Sergeant d'Hendecourt & Lamy 1981; Leinert et al. 1983; Grün et al. 1985).

The source for the interplanetary dust is mainly asteroidal collisions and cometary activity. However, it has been debated without final conclusion to which extent both mechanisms contribute (e.g., Zook & McKay 1986; Leinert & Grün 1990; Durda & Dermott 1997; Landgraf et al. 2002), indicating that neither might be clearly dominating. The spatial distribution – especially in the vertical direction – is expected to differ for dust of cometary and asteroidal origin, respectively, because of the different parent bodies' distribution (Nesvorný et al. 2006). However, drag forces and (resonant) dynamical interaction with planets partly obliterate this history.

The occurrence of two different groups of particles collected in the stratosphere is also attributed to the different origin: cometary dust has a much lower average density 0.6 to 1.7 g cm^{-3}) than asteroidal dust (1.5 to 4.2 g cm^{-3}; Joswiak et al. 2007).

Another prominent source for statistics of interplanetary dust particles is radar data. For instance, Galligan & Baggaley (2004) used meteor echos recorded with the Advanced Meteor Orbit Radar (AMOR) to derive the slope of the cumulative mass distribution: $q-1 \approx 0.9 \ldots 1.0$ (for particle sizes above 40 µm). The so-called IRAS dust bands have also been confirmed with this technique (Galligan & Baggaley 2005).

In addition, recent empirical models of the meteoritic dust complex took into account data from the Diffuse Infrared Background Experiment aboard the Cosmic Background Explorer (Kelsall et al. 1998; Dikarev et al. 2005).

3 Kinetic Theory and its Implementation

Knowledge of single-particle dynamics and effects of individual binary collisions has now to be translated into the properties of the whole disc, considered as an ensemble of dust grains and larger grains.

A straightforward, N-body approach – to follow dynamics of many individual objects and to perform true collision simulations – remains important for studying "difficult" cases where many other methods fail, such as the final stages of planet formation (e.g., Ida & Makino 1993; Kokubo & Ida 1998; Charnoz et al. 2001; Charnoz & Brahic 2001). It can also be useful when the dynamics are complex, whereas any collisional event is assumed to simply eliminate both colliders (Lecavelier des Etangs et al. 1996). However, this method cannot treat a large number of objects sufficient to cover a broad range of particle masses. On the other hand, hydrodynamics or smoothed particle hydrodynamics are suitable for dense s(e.g., protoplanetary) discs, only.

For the rather dilute debris discs, the kinetic approach of statistical physics is more suitable. It is based on the continuity-like equation for the distribution of dust in an appropriate phase space. The idea is to introduce a multi-dimensional "phase space distribution" of dust, for instance a distribution of grain sizes, coordinates, and velocites, and to write down terms that describe the supply, loss and transport of dust grains due to different mechanisms. The resulting equation can be solved for the phase space distribution as a function of time, from which usual size and spatial distributions can easily be calculated. Many authors used the kinetic approach to model debris discs, including the interplanetary dust cloud and presumed Kuiper belt dust disc (e.g., Dohnanyi 1973, 1978; Rhee 1976; Leinert et al. 1983; Gor'kavyi et al. 1997a,b; Ishimoto 2000a,b). However, in most of these papers the goal was to solve for either size *or* spatial distribution – not both.

This gap is bridged by so-called multi-annulus models, which combine the size distributions obtained from local particle-in-a-box calculations at different radial distances (Krivov et al. 2000). Thébault et al. (2003) developed the method further to account for bound objects on highly eccentric yet bound orbits. However, the budgets of mass bins in different annuli need to be coupled in order to account for such orbits.

The work presented here is based on the more natural implementation of the same idea, introduced and mathematically founded by Krivov et al. (2005). The phase space variables they used are semi-major axes and eccentricities instead of radial distances and eccentricities. (Independently, dell'Oro & Paolicchi (1998) introduced a similar aproach for their study of collision rates among asteroids.) Here, the model is generalized to include radiation pressure and transport mechanisms, which makes it applicable to dust discs. The code of Thébault et al. (2003) and Thébault & Augereau (2007) has the same purpose and a similar scope, while the major differences are: their model of the outcomes of an individual collision is somewhat more refined, while the model presented here is following the dynamical evolution more accurately and in a more generic way.

3.1 The Phase Space

3.1.1 Densities

The distribution of something over something else is a key to statistical treatment of physics and I will define the most frequently used distributions and densities here. The "volume number density" is the number of particles per unit volume and size and is written as $n(x,y,z,s,t)$, where x, y, z are the cartesian coordinates, t is the system time. The object radius s represents the variety of material properties that are all assumed to be purely size-dependent.

A more general quantity is the “phase space number density” $n(\mathbf{k},s,t)$, where $\mathbf{k}$ is the vector that contains the 6 six coordinates that pin an object’s location and velocity in space. A formal definition of $n(\mathbf{k},s,t)$ can be obtained from the expression for the total number of objects,

$$N(t) = \int \cdots \int n(\mathbf{k},s,t)\,\mathrm{d}k_1 \cdots \mathrm{d}k_6 \mathrm{d}s, \tag{3.1}$$

where $k_1, \ldots, k_6$ are the components of the vector $\mathbf{k}$. The quantity $N(t)$ is the total number of objects in the phase space volume integrated over.

For brevity, the same symbol n is used to denote different distributions, indicated by the set of parameters. The distribution $n(s,t)$, for example, is different from $n(\mathbf{k},s,t)$ by its definition

$$N(t) = \int n(s,t)\,\mathrm{d}s, \tag{3.2}$$

whence follows

$$n(s,t) = \int n(\mathbf{k},s,t)\,\mathrm{d}k_1 \cdots \mathrm{d}k_6. \tag{3.3}$$

The transformation of a distribution from one coordinate system to another can be achieved via the appropriate Jacobian J, which accounts for the change in “volume” measure:

$$n(\mathbf{k}',s,t) = J^{-1} \cdot n(\mathbf{k},s,t), \tag{3.4}$$

where

$$\mathrm{d}\mathbf{k}' = J\,\mathrm{d}\mathbf{k} \tag{3.5}$$

or

$$J \equiv \left\| \frac{\partial \mathbf{k}'}{\partial \mathbf{k}} \right\|. \tag{3.6}$$

Following the spirit of equation (3.1), the new distribution can be formally defined as

$$\int \cdots \int n(\mathbf{k}',s,t)\,\mathrm{d}\mathbf{k}' \equiv \int \cdots \int n(\mathbf{k},s,t)\,\mathrm{d}\mathbf{k}. \tag{3.7}$$

In the same way, the transformation from size to mass distribution can be obtained from

$$n(\mathbf{k},m,t) = \left| \frac{\mathrm{d}s}{\mathrm{d}m} \right| \cdot n(\mathbf{k},s,t). \tag{3.8}$$

In addition, let $\varphi(\mathbf{k},s,t)$ denote normalized densities:

$$\varphi(\mathbf{k},s,t) \equiv \frac{n(\mathbf{k},s,t)}{N(s,t)} \equiv \frac{n(\mathbf{k},s,t)}{\int \cdots \int n(\mathbf{k},s,t)\,\mathrm{d}\mathbf{k}}. \tag{3.9}$$

3.1.2 Discretization and Averaging

A reduction of the parameter space is necessitated by the limited computational capacity: storage and memory usage as well as duration of the calculations are possible caveats. Consequentially, the number of discrete points on which calculations are performed needs to be limited. The phase space needs to be binned and all involved functions discretized:

$$\phi(\mathbf{k}) \longrightarrow \phi_i, \tag{3.10}$$

where ϕ is an arbitrary function on the phase space variables $\mathbf{k}$. The quantity ϕ_i can be defined, e.g., as the weighted average of ϕ over bin i or as the value of ϕ at an average value $\mathbf{k}_i$, both definitions being linear approximations. The total number of objects in such a bin reads

$$n_i \equiv \int\limits_{V_i} n(\mathbf{k})\,\mathrm{d}\mathbf{k}, \tag{3.11}$$

with V_i being the bin's volume.

The bins' actual numbering, associated with index i, is arbitrary as long as the bins are countable. For example, the index i can be interpreted as a multi-index

$$i = \{i_a, i_e, i_s\}. \tag{3.12}$$

For brevity, the short notation "i" is used henceforth.

The way this binning is chosen depends on the problem. As long as, e.g., the distribution over one particular coordinate is uniform, the according dimensions can be collapsed into one bin. So, in general, one can split the vector of parameters into a group of "more important" ones and a group of "less unimportant" ones. The more important parameters are discretely resolved by more than one bin, while the others are represented by only one. Following the notation of Krivov et al. (2006), the important parameters shall be denoted by $\mathbf{p}$, the unimportant ones by $\mathbf{q}$, where $\mathbf{k} = (\mathbf{p}, \mathbf{q})$. Then, the averaging can be exemplarily expressed by

$$\phi(\mathbf{p}) \equiv \langle \phi(\mathbf{k}) \rangle_{\mathbf{q}} \equiv \frac{1}{n(\mathbf{p})} \int\limits_{\mathbf{q}} \phi(\mathbf{k}) n(\mathbf{k})\,\mathrm{d}\mathbf{q}, \tag{3.13}$$

where

$$n(\mathbf{p}) \equiv \int\limits_{\mathbf{q}} n(\mathbf{k})\,\mathrm{d}\mathbf{q}. \tag{3.14}$$

As a convention, omitting variables (except for t) from the list of arguments of a function is supposed to denote that averaging procedure. The volume of the subspace of omitted variables is

$$|V_{\mathbf{q}}| \equiv \int\limits_{\mathbf{q}} \mathrm{d}\mathbf{q}. \tag{3.15}$$

Note that, defined in this manner, the volume is finite only as long as the involved dimensions are finite, i.e. for the angular parameters but not for the axis and the eccentricity. Also note that the physical dimension of, e.g., ϕ is unchanged by the averaging while that of $n(\ldots)$ is altered by a factor corresponding to the dimension of the omitted variables. The unit of $n(\ldots)$ changes from "number of objects per full phase space and object size" to "number of objects per reduced phase space and object size".

3.1.3 Phase Space Variables

Following Krivov et al. (2005), the grain size s and a vector of orbital elements $\mathbf{k}$ are chosen as phase space variables. This is a distinct feature of the kinetic approach: usually, coordinates and velocities in a corotating "box" are used instead (e.g. Greenberg et al. 1978; Spaute et al. 1991; Weidenschilling et al. 1997; Thébault et al. 2003). To accommodate systems where large eccentricites and/or inclination cause large radial and/or vertical excursions of particles, standard codes employ multiannulus schemes, whereas our approach treats such cases in a straightforward way. Roughly speaking, we translate from the single-particle dynamics to an ensemble of particles using the idea known for centuries in classical celestial mechanics: to use slowly changing osculating elements instead of rapidly changing coordinates and velocities.

For this work, the particular choice for $\mathbf{p}$ and $\mathbf{q}$ is the following. The distribution $n(\ldots)$ is resolved to only two dimensions, the semi-major axis a and the eccentricity e. The remaining four dimensions, the angles, are averaged over. So, the phase space density most often used is

$$n(a,e,s,t) \quad \equiv \quad \iiiint\limits_{i,\Omega,\omega,\theta} n(a,e,i,\Omega,\omega,\theta,s,t)\,\mathrm{d}\theta\,\mathrm{d}\omega\,\mathrm{d}\Omega\,\mathrm{d}i, \tag{3.16}$$

where $(a,e) = \mathbf{p}$ and $(i,\Omega,\omega,\theta) = \mathbf{q}$. That choice of parameters poses restrictions to the scope of the approach since neither azimuthal nor vertical asymmetries can be modelled.

However, this approximation is justified by the addressed problem. First, collisions in debris discs are sufficiently rare and allow for the averaging over the fast angle, the anomaly. The collisional lifetime of an object is usually significantly longer than one orbital period. Therefore, two consecutive collisions of one object are not correlated. They are randomized with respect to θ. For dense discs, like protoplanetary discs, this might be too crude an approximation. What is more severe, setups with pronounced angular structure lead to inaccuracy as well. An example for stable structures of that kind are object populations in an outer planetary resonance. The inherent deviations of collisional rates and velocities from the symmetric case are addressed by, e.g., dell'Oro & Paolicchi (1998) and Queck et al. (2007). However, their results suggest that the considering the angular modulation separately has no major influence on the evolution.

Second, averaging over the orientation of the apsidal lines, which is described by the angles ω and Ω, again leads to neglecting angular structure. Resonant systems and major break-ups are the most prominent problematic cases here, as well. The justification for the approximation is the same as that for θ.

Third, the distribution of inclinations i as defined by mutual collisions and scattering alone is coupled in thermodynamic equilibrium to the distribution of eccentricities. For instance, Ida (1990) found a 2:1 ratio between orbital eccentricities and inclinations for the case of moderate and high relative velocities. And again, perturbations due to planetary gravitation pose the severest "threat" to the approximation because they can break the coupling between I and e.

3.2 The Master Equation

The general equation for the evolution of the distribution $n(\mathbf{k},s,t)$ is that of its time derivative

$$\frac{\mathrm{d}n}{\mathrm{d}t}(\mathbf{k},s,t) = \underbrace{\left(\frac{\mathrm{d}n}{\mathrm{d}t}\right)_{\text{gain}}}_{\text{sources}} - \underbrace{\left(\frac{\mathrm{d}n}{\mathrm{d}t}\right)_{\text{loss}}}_{\text{sinks}} - \underbrace{\mathrm{div}(n\dot{\mathbf{k}})}_{\text{transport}}. \tag{3.17}$$

In the following subsections, the individual terms for gain, loss, and transport of material are discussed along with the discretisation into a grid.

3.2.1 Gain and Loss

The central process in this approach is binary collisions. Hence, gain and loss of material are directly proportional to the number densities of potential colliders. For example, the gain can be written as

$$\left(\frac{\mathrm{d}n}{\mathrm{d}t}\right)_{\text{gain}} = \iiiint\limits_{\mathbf{k}_\mathrm{t},s_\mathrm{t};\mathbf{k}_\mathrm{p},s_\mathrm{p}} G(\mathbf{k}_\mathrm{t},s_\mathrm{t};\mathbf{k}_\mathrm{p},s_\mathrm{p};\mathbf{k},s)n(\mathbf{r},\mathbf{v}_\mathrm{t},s_\mathrm{t})n(\mathbf{r},\mathbf{v}_\mathrm{p},s_\mathrm{p})\,\mathrm{d}s_\mathrm{p}\,\mathrm{d}\mathbf{k}_\mathrm{p}\,\mathrm{d}s_\mathrm{t}\,\mathrm{d}\mathbf{k}_\mathrm{t} \tag{3.18}$$

and the loss as

$$\left(\frac{\mathrm{d}n}{\mathrm{d}t}\right)_{\text{loss}} = \iint\limits_{\mathbf{k}_\mathrm{p},s_\mathrm{p}} L(\mathbf{k},s;\mathbf{k}_\mathrm{p},s_\mathrm{p})n(\mathbf{r},\mathbf{v},s)n(\mathbf{r},\mathbf{v}_\mathrm{p},s_\mathrm{p})\,\mathrm{d}s_\mathrm{p}\,\mathrm{d}\mathbf{k}_\mathrm{p}. \tag{3.19}$$

The gain function G is a product of two quantities: (i) the probability of collisions between targets and projectiles, denoted by R, and (ii) the number of fragments $(\mathbf{k},s)$ produced in one such collision, denoted by F:

$$G(\mathbf{r},\mathbf{v},s;\mathbf{v}_\mathrm{t},s_\mathrm{t};\mathbf{v}_\mathrm{p},s_\mathrm{p}) = R(\mathbf{r};\mathbf{v}_\mathrm{t},s_\mathrm{t};\mathbf{v}_\mathrm{p},s_\mathrm{p})\,F(\mathbf{r},\mathbf{v},s;\mathbf{v}_\mathrm{t},s_\mathrm{t};\mathbf{v}_\mathrm{p},s_\mathrm{p}). \tag{3.20}$$

First, we start in cartesian coordinates. The rate of collisions for two groups passing through each other at location $\mathbf{r}$ is given by the densities n_t and n_p multiplied by

$$R(\mathbf{r}_\mathrm{t};\mathbf{v}_\mathrm{t},s_\mathrm{t};\mathbf{v}_\mathrm{p},s_\mathrm{p}) = v_\mathrm{imp}(\mathbf{v}_\mathrm{t},\mathbf{v}_\mathrm{p})\sigma(s_\mathrm{t},s_\mathrm{p}) \tag{3.21}$$

(via a local particle-in-a-box treatment). The resulting cartesian version of equation (3.18) is

$$\begin{aligned}\left(\frac{\mathrm{d}n}{\mathrm{d}t}\right)_\mathrm{gain} &= \iiiint\limits_{\mathbf{v}_\mathrm{t},s_\mathrm{t};\mathbf{v}_\mathrm{p},s_\mathrm{p}} \hat{G}(\mathbf{r},\mathbf{v},s;\mathbf{v}_\mathrm{t},s_\mathrm{t};\mathbf{v}_\mathrm{p},s_\mathrm{p})\,\mathrm{d}\mathbf{v}_\mathrm{p}\,\mathrm{d}s_\mathrm{p}\,\mathrm{d}\mathbf{v}_\mathrm{t}\,\mathrm{d}s_\mathrm{t} \\ &= \iiiint\limits_{\mathbf{v}_\mathrm{t},s_\mathrm{t};\mathbf{v}_\mathrm{p},s_\mathrm{p}} F(\mathbf{r},\mathbf{v},s;\mathbf{v}_\mathrm{t},s_\mathrm{t};\mathbf{v}_\mathrm{p},s_\mathrm{p})v_\mathrm{imp}(\mathbf{v}_\mathrm{t},\mathbf{v}_\mathrm{p})\sigma(s_\mathrm{t},s_\mathrm{p}) \\ &\qquad n(\mathbf{r},\mathbf{v}_\mathrm{t},s_\mathrm{t})n(\mathbf{r},\mathbf{v}_\mathrm{p},s_\mathrm{p})\,\mathrm{d}\mathbf{v}_\mathrm{p}\,\mathrm{d}s_\mathrm{p}\,\mathrm{d}\mathbf{v}_\mathrm{t}\,\mathrm{d}s_\mathrm{t}.\end{aligned} \tag{3.22}$$

Here, we do explicitely assume that both colliders and the fragments share the same location in space, $\mathbf{r}$, which is the collisional condition. In order to make that expression symmetric with respect to the locations of all participants, we can use the following identity, valid for all functions ϕ:

$$\int\limits_{\mathbf{x}'} \phi(\mathbf{x}')\,\delta(\mathbf{x}-\mathbf{x}')\,\mathrm{d}\mathbf{x}' = \begin{cases} \phi(\mathbf{x}) \text{ for } \mathbf{x}\in\{x'\}, \\ 0 \text{ else,}\end{cases} \tag{3.23}$$

where δ is Dirac's distribution. Application to the distributions n,

$$n(\mathbf{r},\mathbf{v}_\mathrm{t},s_\mathrm{t}) = \int\limits_{\mathbf{r}_\mathrm{t}} n(\mathbf{r}_\mathrm{t},\mathbf{v}_\mathrm{t},s_\mathrm{t})\delta(\mathbf{r}_\mathrm{t}-\mathbf{r})\,\mathrm{d}\mathbf{r}_\mathrm{t}, \tag{3.24}$$

$$n(\mathbf{r},\mathbf{v}_\mathrm{p},s_\mathrm{p}) = \int\limits_{\mathbf{r}_\mathrm{p}} n(\mathbf{r}_\mathrm{p},\mathbf{v}_\mathrm{p},s_\mathrm{p})\delta(\mathbf{r}_\mathrm{p}-\mathbf{r})\,\mathrm{d}\mathbf{r}_\mathrm{p}, \tag{3.25}$$

results in

$$\begin{aligned}\left(\frac{\mathrm{d}n}{\mathrm{d}t}\right)_\mathrm{gain} &= \int\limits_{\mathbf{r}_\mathrm{t},\mathbf{v}_\mathrm{t},s_\mathrm{t};\mathbf{v}_\mathrm{p},\mathbf{v}_\mathrm{p},s_\mathrm{p}}\!\!\cdots\!\!\int F(\mathbf{r},\mathbf{v},s;\mathbf{v}_\mathrm{t},s_\mathrm{t};\mathbf{v}_\mathrm{p},s_\mathrm{p})v_\mathrm{imp}(\mathbf{v}_\mathrm{t},\mathbf{v}_\mathrm{p})\sigma(s_\mathrm{t},s_\mathrm{p}) \\ &\qquad n(\mathbf{r}_\mathrm{t},\mathbf{v}_\mathrm{t},s_\mathrm{t})n(\mathbf{r}_\mathrm{p},\mathbf{v}_\mathrm{p},s_\mathrm{p})\delta(\mathbf{r}_\mathrm{p}-\mathbf{r})\delta(\mathbf{r}_\mathrm{t}-\mathbf{r}) \\ &\qquad \mathrm{d}\mathbf{r}_\mathrm{p}\,\mathrm{d}\mathbf{v}_\mathrm{p}\,\mathrm{d}s_\mathrm{p}\,\mathrm{d}\mathbf{r}_\mathrm{t}\,\mathrm{d}\mathbf{v}_\mathrm{t}\,\mathrm{d}s_\mathrm{t}.\end{aligned} \tag{3.26}$$

The two δ functions represent the fact that “p” has to meet “t” in order to collide and that both share the same location with possible fragments at the moment of the collision. The latter condition can be wrapped together with F into a new function, the *fragment generating function* f:

$$f(\mathbf{r},\mathbf{v},s;\mathbf{r}_\mathrm{t},\mathbf{v}_\mathrm{t},s_\mathrm{t};\mathbf{r}_\mathrm{p},\mathbf{v}_\mathrm{p},s_\mathrm{p})\delta(\mathbf{r}_\mathrm{p}-\mathbf{r}_\mathrm{t}) \equiv \tag{3.27}$$

$$F(\mathbf{r},\mathbf{v},s;\mathbf{v}_\mathrm{t},s_\mathrm{t};\mathbf{v}_\mathrm{p},s_\mathrm{p})\,\delta(\mathbf{r}_\mathrm{p}-\mathbf{r})\,\delta(\mathbf{r}_\mathrm{p}-\mathbf{r}). \tag{3.28}$$

Now, we can do the final step and replace all functions of cartesian coordinates by the appropriate ones in phase space coordinates. The impact speed v_imp and the cross section σ are invariant scalars and simply transformed as

$$v_{\mathrm{imp}}(\mathbf{v}_{\mathrm{t}},\mathbf{v}_{\mathrm{p}}) = v_{\mathrm{imp}}(\mathbf{v}(\mathbf{k}_{\mathrm{t}}),\mathbf{v}(\mathbf{k}_{\mathrm{p}})), \sigma(m\mathbf{v}_{\mathrm{t}},\mathbf{v}_{\mathrm{p}}) = v_{\mathrm{imp}}(\mathbf{v}(\mathbf{k}_{\mathrm{t}}),\mathbf{v}(\mathbf{k}_{\mathrm{p}})). \tag{3.29}$$

The Jacobians that appear in the transformation of the differentials cancel out with those that transform the distributions n and δ. The final result reads

$$\begin{aligned}\left(\frac{\mathrm{d}n}{\mathrm{d}t}\right)_{\mathrm{gain}}(\mathbf{k},s,t) \quad = \quad & \iiiint\limits_{\mathbf{k}_{\mathrm{t}},s_{\mathrm{t}};\mathbf{k}_{\mathrm{p}},s_{\mathrm{p}}} f(\mathbf{k},s;\mathbf{k}_{\mathrm{t}},s_{\mathrm{t}};\mathbf{k}_{\mathrm{p}},s_{\mathrm{p}})v_{\mathrm{imp}}(\mathbf{v}(\mathbf{k}_{\mathrm{t}}),\mathbf{v}(\mathbf{k}_{\mathrm{p}}))\sigma(s_{\mathrm{t}},s_{\mathrm{p}}) \\ & n(\mathbf{k}_{\mathrm{t}},s_{\mathrm{t}},t)n(\mathbf{k}_{\mathrm{p}},s_{\mathrm{p}},t)\delta(\mathbf{r}(\mathbf{k}_{\mathrm{p}})-\mathbf{r}(\mathbf{k}_{\mathrm{t}})) \\ & \mathrm{d}\mathbf{k}_{\mathrm{p}}\,\mathrm{d}s_{\mathrm{p}}\,\mathrm{d}\mathbf{k}_{\mathrm{t}}\,\mathrm{d}s_{\mathrm{t}}.\end{aligned} \tag{3.30}$$

The new fragment generating function is consequentially given by

$$f(\mathbf{k},s;\mathbf{k}_{\mathrm{t}},s_{\mathrm{t}};\mathbf{k}_{\mathrm{p}},s_{\mathrm{p}}) = J\cdot f(\mathbf{r},\mathbf{v},s;\mathbf{v}_{\mathrm{t}},s_{\mathrm{t}};\mathbf{v}_{\mathrm{p}},s_{\mathrm{p}}), \tag{3.31}$$

which is just an expression of the fact that f is a *distribution* of fragments.

Likewise, the loss terms can be written as

$$\begin{aligned}\left(\frac{\mathrm{d}n}{\mathrm{d}t}\right)_{\mathrm{loss}}(\mathbf{k},s,t) \quad &= \quad \iint\limits_{\mathbf{k}_{\mathrm{p}},s_{\mathrm{p}}} \hat{L}(\mathbf{k},s;\mathbf{k}_{\mathrm{p}},s_{\mathrm{p}})\,\mathrm{d}\mathbf{k}_{\mathrm{p}}\,\mathrm{d}s_{\mathrm{p}} \\ &= \quad \iint\limits_{\mathbf{k}_{\mathrm{p}},s_{\mathrm{p}}} \hat{R}(\mathbf{k},s;\mathbf{k}_{\mathrm{p}},s_{\mathrm{p}})\,\mathrm{d}\mathbf{k}_{\mathrm{p}}\,\mathrm{d}s_{\mathrm{p}} \\ &= \quad \iint\limits_{\mathbf{k}_{\mathrm{p}},s_{\mathrm{p}}} v_{\mathrm{imp}}(\mathbf{v}(\mathbf{k}),\mathbf{v}(\mathbf{k}_{\mathrm{p}}))\sigma(s,s_{\mathrm{p}}) \\ & \qquad n(\mathbf{k},s,t)n(\mathbf{k}_{\mathrm{p}},s_{\mathrm{p}},t)\delta(\mathbf{r}(\mathbf{k})-\mathbf{r}(\mathbf{k}_{\mathrm{p}})) \\ & \qquad \mathrm{d}\mathbf{k}_{\mathrm{p}}\,\mathrm{d}s_{\mathrm{p}}.\end{aligned} \tag{3.32}$$

3.2.2 Discretization

Now, this averaging procedure can be applied to the Master Equation, as exemplified by the gain:

$$\begin{aligned}\left(\frac{\mathrm{d}n}{\mathrm{d}t}\right)_{\mathrm{gain}}(\mathbf{p},s,t) \quad = \quad & \int\limits_{\mathbf{p}_{\mathrm{t}},s_{\mathrm{t}};\mathbf{p}_{\mathrm{p}},s_{\mathrm{p}};\Lambda}\!\!\cdots\!\int f(\mathbf{p},s;\mathbf{p}_{\mathrm{t}},s_{\mathrm{t}};\mathbf{p}_{\mathrm{p}},s_{\mathrm{p}};r(\Lambda))v_{\mathrm{imp}}(\mathbf{v}(\mathbf{p}_{\mathrm{t}},r(\Lambda)),\mathbf{v}(\mathbf{p}_{\mathrm{p}},r(\Lambda))) \\ & \sigma(s_{\mathrm{t}},s_{\mathrm{p}})n(\mathbf{p}_{\mathrm{t}},s_{\mathrm{t}},t)n(\mathbf{p}_{\mathrm{p}},s_{\mathrm{p}},t)\Delta(\mathbf{p}_{\mathrm{t}},\mathbf{p}_{\mathrm{p}};r(\Lambda)) \\ & \mathrm{d}\Lambda\,\mathrm{d}\mathbf{p}_{\mathrm{p}}\,\mathrm{d}s_{\mathrm{p}}\,\mathrm{d}\mathbf{p}_{\mathrm{t}}\,\mathrm{d}s_{\mathrm{t}}.\end{aligned} \tag{3.33}$$

At this point, I have to strain the reader's nerves twice more and draw the attention to Λ and Δ.

The introduced function Δ can be defined as

$$\Delta(\mathbf{p}_{\mathrm{t}},\mathbf{p}_{\mathrm{p}},\Lambda) \equiv \left\langle \delta\left[\mathbf{r}(\mathbf{k}_{\mathrm{p}})-\mathbf{r}(\mathbf{k}_{\mathrm{t}})\right]\right\rangle_{\{\mathbf{q}_{\mathrm{t}},\mathbf{q}_{\mathrm{t}}\}\backslash\{\Lambda\}}. \tag{3.34}$$

It is the average of the δ function over all the unimportant parameters except for the "less unimportant" parameter Λ. Since Δ is an average expression for the collisional condition, it is best interpreted as the geometrical overlap or collisional probability of two orbits. Details and the derivation of Δ are discussed in Sect. 3.3.1.

The parameter Λ shall be defined as the angular distance between the apsidal lines of the two colliders' orbits, as depicted in Figure 3.1. (Formally, one could split up the vector of unimportant, uniformly distributed variables, $\mathbf{q}$, into two sub-sets of variables, $\mathbf{q}'$ and $\mathbf{q}''$. The vector $\mathbf{q}'$ may contain variables

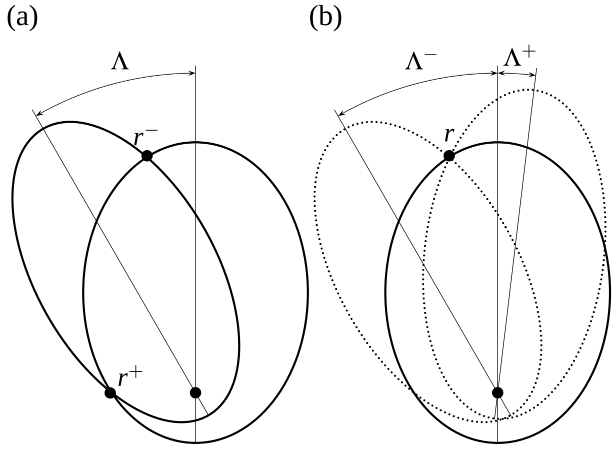

Figure 3.1: Two elliptic orbits crossing in 2D: (a) two cases for fixed difference $\Lambda = \varpi_\mathrm{p} - \varpi_\mathrm{t}$, (b) two cases for fixed $r = r_\mathrm{t} = r_\mathrm{p}$.

like θ_t that have stronger influence on F, v_imp, and Δ or their product, while the vector $\mathbf{q}''$ may be comprised of the remaining parameters.)

For sufficiently eccentric orbits, Λ reflects the dependence of the relative velocity and collisional probability on the radial distance from the central star. Therefore, even though the spatial distribution is azimuthally uniform, different *relative* orientations of the colliders' orbits lead to different distances for the collisions and to different fragment orbits. Having Λ as an argument of functions is convenient because Λ immediately determines the target's true anomaly

$$\begin{aligned}\theta_\mathrm{t} &= \arcsin\frac{p_\mathrm{t} e_\mathrm{p}\sin\Lambda}{\sqrt{p_\mathrm{p}^2 e_\mathrm{t}^2 + p_\mathrm{t}^2 e_\mathrm{p}^2 - 2p_\mathrm{p} p_\mathrm{t} e_\mathrm{p} e_\mathrm{t}\cos\Lambda}}\\ &\pm \arccos\frac{p_\mathrm{p} - p_\mathrm{t}}{\sqrt{p_\mathrm{p}^2 e_\mathrm{t}^2 + p_\mathrm{t}^2 e_\mathrm{p}^2 - 2p_\mathrm{p} p_\mathrm{t} e_\mathrm{p} e_\mathrm{t}\cos\Lambda}}, \end{aligned} \tag{3.35}$$

which, in turn, determines the distance r via the equation of conic section:

$$r = \frac{a(1-e^2)}{1 + e\cos\theta}. \tag{3.36}$$

Thus, the functions are kept explicitely depending on $r(\Lambda)$ while the distribution n is not. Due to the integration over unimportant variables, the interpretation of the functions f, v_imp, and Δ changes. They are now averages for two particles colliding at distance r to the star, i.e. inclinations are averaged over. Note that, in the framework of this approach, the restriction to rotational symmetry is caused wholly by the distribution n.

In a short notation with discrete bins, the Master Equation *without* transport terms reads

$$\dot{n}_i = \frac{1}{2}\sum_{jkl} G_{ijkl} n_j n_k - \frac{1}{2}\sum_{jl} L_{ijl} n_i n_j \tag{3.37}$$

$$= \frac{1}{2}\sum_{jkl} f_{ijkl}\, R_{jkl}\, n_j n_k - \frac{1}{2}\sum_{jl} R_{ijl}\, n_j n_k \tag{3.38}$$

$$= \frac{1}{2}\sum_{jkl} f_{ijkl}\, \Delta_{jkl}\, n_j\, n_k\, v_{jkl}\, \sigma_{jk} - \frac{1}{2}\sum_{jl} \Delta_{ijl}\, n_i\, n_j\, v_{ijl}\, \sigma_{ij}, \tag{3.39}$$

where the index l denotes the summation/integration over Λ. The factor $1/2$ accounts for gain and loss being symmetric with respect to the colliders, i.e. $G_{ijkl} = G_{ikjl}$ and $L_{ijl} = L_{jil}$.

A remarkable property of the quadratic equation (3.37) is that it can be rewritten as

$$\dot{n}_i = \sum_m A_{im} n_m, \tag{3.40}$$

where

$$\begin{aligned} A_{im} &= \frac{1}{2}\frac{\partial \dot{n}_i}{\partial n_m} = \frac{1}{4}\sum_{jkl} G_{ijkl}(n_j\delta_{km} + n_k\delta_{jm}) - \frac{1}{4}\sum_{jl} L_{ijl}(n_i\delta_{jm} + n_j\delta_{im}) & (3.41) \\ &= \frac{1}{2}\sum_{jl} G_{ijml} n_j - \frac{1}{4}\sum_{jl} L_{jml} n_j(\delta_{ij} + \delta_{im}). & (3.42) \end{aligned}$$

Here, δ_{ij} is Kronecker's delta. In principle, one could proceed further and define

$$\dot{n}_i = \sum_{mm'} B_{imm'} n_m n_{m'}, \tag{3.43}$$

where

$$B_{imm'} = \frac{1}{2}\frac{\partial^2 \dot{n}_i}{\partial n_{m'}\partial n_m} = \frac{1}{2}\sum_l \left[G_{imm'l} - L_{mm'l}\delta_{im}\right]. \tag{3.44}$$

Unlike A_{im} This result is time-independent but, unfortunately, a tensor with too many entries to be stored.

3.2.3 The Grid

The chosen numerical implementation of the phase space distribution is a discrete grid with three dimensions for mass/size, semi-major axis, and eccentricity:

$$n_i(t) \equiv \int_{V_i} n(a,e,s,t)\, \mathrm{d}a\, \mathrm{d}e\, \mathrm{d}s, \tag{3.45}$$

with $n(a,e,s,t)$ defined in equation (3.16). Since n_i is an integral of $n(a,e,s,t)$ over the according phase space region, it is no longer a phase space number density but a number (per bin).

The size of objects under investigation spans more than 10 order of magnitude (30 orders in mass) from the submicron regime to tens of kilometres. Therefore, the according mass/size grid necessarily cannot be linear and it was chosen to be based on logarithmic stepping, instead. The required size for a grid to span 30 orders of magnitude at a sufficiently fine stepping with factors between $\mu = 4$ and $\mu = 2$ is 50 to 100 steps (or 51 to 101 bins).

In the first versions of the numerical code, the semi-major axis grid was linear (Krivov et al. 2005, 2006). However, a logarithmic stepping was preferred later on for two reasons. First, some geometrical quantities connected with crossing orbits scale with the ratio of the semi-major axes of the colliders, not with the individual axes. Thus, for two colliders "t" and "p" – for "target" and "projectile", respectively –, the number of free geometrical parameters can be reduced from four, $(a_\mathrm{t}, e_\mathrm{t}, a_\mathrm{p}, e_\mathrm{p})$, to three, $(a_\mathrm{t}/a_\mathrm{p}, e_\mathrm{t}, e_\mathrm{p})$. Thus, pre-calculation of those geometrical quantities is faster. And second, memory usage is reduced. See section 3.3.1 for details.

For the grid of eccentricities, a trade-off between two regimes needs to be considered. On the one hand, there are bigger objects (or damped discs as a whole), which are usually occupying phase space regions with lower eccentricities. On the other hand, smaller particles are affected by radiation and can move along highly eccentric orbits. Consequentially, a linear stepping was used for the eccentricity bins.

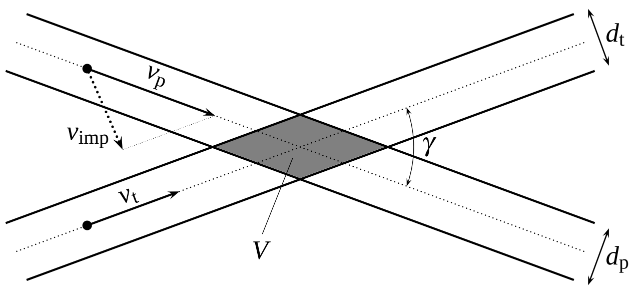

Figure 3.2: Collision of two groups of particles in a small volume of interaction $V = d_t d_p h/|\sin\gamma|$, where h is the height perpendicular to the plane of projection, i.e. the disc's thickness at that point.

3.3 Treatment of Collisions

This section explains the actual calculation of collisional probabilities Δ and velocities v_{imp}, as well as the distribution of fragments over sizes and orbits.

3.3.1 Impact Velocity and Probability

From Section 3.2.1, we know that the rate of collisions between an ensemble of targets "t" and an ensemble of projectiles "p" is a product of both groups' phase space densities, the relative velocity, the binary collisional cross section, and the geometric overlap between the two orbits. In this section, explicit expressions for those quantities will be given.

Consider first a single particle flying a certain distance through an ensemble of targets distributed at a given number density ρ_t with an interaction cross-section σ. The differential hit probability with respect to x, the distance flown, is given by $\sigma\rho_t\,\mathrm{d}x$. If, instead of a single projectile, we consider a second ensemble of a given density ρ_p, interacting with the target ensemble, we get the symmetric expression

$$\mathrm{d}W = \sigma\rho_p\rho_t V\mathrm{d}x \tag{3.46}$$

for the number of collisions, with V being the effective volume of interaction. The actual rate of collisions involving an impact velocity $v_{\text{imp}} = \mathrm{d}x/\mathrm{d}t$ is then

$$\frac{\mathrm{d}W}{\mathrm{d}t} = \sigma\rho_p\rho_t v_{\text{imp}} V. \tag{3.47}$$

In 2D, with inclinations neglected or averaged out, a single bound orbit is fully represented by a triplet of elements: the semimajor axis a, the eccentricity e , and the longitude of the pericentre (or: angular position of the apsidal line) $\varpi = \Omega + \omega$. Under the axisymmetric condition assumed here, the distribution over ϖ is uniform from 0 to 2π. Then, collisions between two orbits (a_t, e_t, ϖ_t) and (a_p, e_p, ϖ_p) occur in one or two volumes of (infinitely) small extent (or: points) if the orbits are grazing or intersecting. The actual size of the volume is given by the two "thicknesses" d_t and d_p of the ellipses, the crossing angle γ, and the vertical thickness or height h of the disc at distance r (Fig. 3.2). This height depends on the disc's geometry and is given by $h = 2r\sin\varepsilon$ for a standard case with semi-opening angle ε.

The linear number density $\hat{\rho}$ of projectiles and targets along their orbits is determined by their phase space densities $n(\mathbf{p}_t, s_t, t)$ and $n(\mathbf{p}_p, s_p, t)$, respectively, together with the elementary phase space volume $\mathrm{d}\mathbf{p} = \mathrm{d}a\,\mathrm{d}e\,\mathrm{d}m$ and the Kepler equation, which gives the individual orbital velocity v and the orbital period P:

$$\mathrm{d}\hat{\rho} = \frac{n}{vP}\,\mathrm{d}\mathbf{p}. \tag{3.48}$$

Thus, the usual number densities at the point of collision and the interaction volume can be written as

$$\mathrm{d}\rho_\mathrm{t} = \frac{n_\mathrm{t}\,\mathrm{d}\mathbf{p}_\mathrm{t}\,\mathrm{d}\varpi_\mathrm{t}}{v_\mathrm{t}P_\mathrm{t}d_\mathrm{t}h}, \quad \mathrm{d}\rho_\mathrm{p} = \frac{n_\mathrm{p}\,\mathrm{d}\mathbf{p}_\mathrm{p}\,\mathrm{d}\varpi_\mathrm{p}}{v_\mathrm{p}P_\mathrm{p}d_\mathrm{p}h}, \qquad V = \frac{d_\mathrm{t}d_\mathrm{p}h}{|\sin\gamma|}, \tag{3.49}$$

containing phase space densities $n(a,e,\varpi) = n(a,e)/(2\pi)$. The involved orbital velocities and periods can be expressed as

$$v_\mathrm{p,t} = \sqrt{GM(1-\beta_\mathrm{p,t})\left[\frac{2}{r} - \frac{1}{a_\mathrm{p,t}}\right]}, \tag{3.50}$$

$$P_\mathrm{p,t} = 2\pi\sqrt{\frac{a^3_\mathrm{p,t}}{GM(1-\beta_\mathrm{p,t})}}, \tag{3.51}$$

and the crossing angle γ implicitely as

$$\cos\gamma = \frac{1+\left(\frac{1}{r}\frac{\partial r}{\partial\theta_\mathrm{p}}\right)\left(\frac{1}{r}\frac{\partial r}{\partial\theta_\mathrm{t}}\right)}{\sqrt{\left[1+\left(\frac{1}{r}\frac{\partial r}{\partial\theta_\mathrm{p}}\right)^2\right]\left[1+\left(\frac{1}{r}\frac{\partial r}{\partial\theta_\mathrm{t}}\right)^2\right]}} \tag{3.52}$$

and

$$|\sin\gamma| = \frac{\left|\frac{1}{r}\frac{\partial r}{\partial\theta_\mathrm{p}} - \frac{1}{r}\frac{\partial r}{\partial\theta_\mathrm{t}}\right|}{\sqrt{\left[1+\left(\frac{1}{r}\frac{\partial r}{\partial\theta_\mathrm{p}}\right)^2\right]\left[1+\left(\frac{1}{r}\frac{\partial r}{\partial\theta_\mathrm{t}}\right)^2\right]}}. \tag{3.53}$$

The resulting variant of equation (3.47) contains the phase space densities n instead of number densities ρ:

$$\begin{aligned}
\mathrm{d}\frac{\mathrm{d}W}{\mathrm{d}t} &= \frac{\sigma n(a_\mathrm{p},e_\mathrm{p},\varpi_\mathrm{p})\,n(a_\mathrm{t},e_\mathrm{t},\varpi_\mathrm{t})\,v_\mathrm{imp}}{v_\mathrm{t}v_\mathrm{p}P_\mathrm{t}P_\mathrm{p}2r\sin\varepsilon|\sin\gamma|}\,\mathrm{d}\mathbf{p}_\mathrm{p}\,\mathrm{d}\varpi_\mathrm{p}\,\mathrm{d}\mathbf{p}_\mathrm{t}\,\mathrm{d}\varpi_\mathrm{t} \\
&= \frac{\sigma n(a_\mathrm{p},e_\mathrm{p})\,n(a_\mathrm{t},e_\mathrm{t})\,\varphi(\Lambda)\,v_\mathrm{imp}}{v_\mathrm{p}v_\mathrm{t}P_\mathrm{p}P_\mathrm{t}2r\sin\varepsilon|\sin\gamma|}\,\mathrm{d}\mathbf{p}_\mathrm{p}\,\mathrm{d}\mathbf{p}_\mathrm{t}\,\mathrm{d}\Lambda,
\end{aligned} \tag{3.54}$$

where $\varphi(\Lambda)$ represents the distribution of pairs of colliders over Λ, which is uniform, as the system is axisymmetric. As all variables in equations (3.50)–(3.53) depend on ϖ_p and ϖ_t through $\Lambda = \varpi_\mathrm{p} - \varpi_\mathrm{t}$ only, $\mathrm{d}\varpi_\mathrm{p}\,\mathrm{d}\varpi_\mathrm{t}/(4\pi^2)$ is transformed to $(\mathrm{d}(\varpi_\mathrm{p}-\varpi_\mathrm{t})\,\mathrm{d}(\varpi_\mathrm{p}+\varpi_\mathrm{t})/(8\pi^2)$, and integrated once over $\varpi_\mathrm{p}+\varpi_\mathrm{t}$ from 0 to 4π, is giving $\mathrm{d}\Lambda/(2\pi)$ or $\varphi(\Lambda)\mathrm{d}\Lambda$. (See Fig. 3.1 for a graphical definition of λ.)

After separating the number densities, the impact velocity, the cross section σ, and the differentials, the remaining term describes the geometric probability of a collision of two such orbits, but averaged over all variables not involved in the above calculations: the inclinations and the absolute orientation of (one of) the orbits. This probability is of unit one per volume and is very similar to the Δ-integral in Krivov et al. (2005), but without averaging over the relative positions of both orbits – there is still a dependence on the distance to the star r at which the collision occurs:

$$\Delta(\mathbf{p}_\mathrm{p},\mathbf{p}_\mathrm{t},\Lambda) = \frac{1}{v_\mathrm{p}v_\mathrm{t}P_\mathrm{p}P_\mathrm{t}2r(\Lambda)\sin\varepsilon|\sin\gamma(\Lambda)|}. \tag{3.55}$$

Except for the special case of grazing orbits with $\gamma = 0$, two orbits in the same plane always cross at two points (Fig. 3.1), or given the target's true anomaly, there are two ways in which the projectile can cross the target's orbit: moving inward or moving outward. Accordingly, both signs have to be treated for the derivative $\partial r/\partial\theta_\mathrm{p}$, giving γ^+ and γ^-. From the absolute values of v_p, v_t and γ we derive the relative velocity

$$v_{\rm imp}(\mathbf{p}_{\rm p},\mathbf{p}_{\rm t},\Lambda) \quad = \quad \sqrt{v_{\rm p}^2+v_{\rm t}^2-2v_{\rm p}v_{\rm t}\cos\gamma(\Lambda)}. \tag{3.56}$$

For sufficiently massive targets, one has to take into account the gravitational attraction and correct the impact velocity to

$$v'_{\rm imp} = \sqrt{v_{\rm imp}^2 + \frac{2Gm_{\rm t}}{r}}. \tag{3.57}$$

However, for an asteroid with $s = 100$ km and $\rho = 3000$ kg m^{-3}, this correction is comparable to typical relative velocities $v_{\rm imp} = 0.1v_{\rm k}$ only very far from the star, at distances of around 500 AU. Therefore, $v'_{\rm imp} \approx v_{\rm imp}$ for typical cases addressed here. The same is true for the equivalent correction to the collisional cross section due to gravitational focussing: $\sigma' \approx \sigma$.

Now, the 3D corrections necessary to account for (small) orbital inclinations are discussed. As the gain and loss terms (e.g., Eq. 3.33) contain integrals of $\Delta(\mathbf{p}_{\rm p},\mathbf{p}_{\rm t},\Lambda)$ and $v_{\rm imp}(\mathbf{p}_{\rm p},\mathbf{p}_{\rm t},\Lambda)$ over Λ, averages were calculated:

$$\Delta(\mathbf{p}_{\rm p},\mathbf{p}_{\rm t}) \quad = \quad \frac{1}{2\pi}\int_0^{2\pi}\Delta(\mathbf{p}_{\rm p},\mathbf{p}_{\rm t};\ \Lambda)\,{\rm d}\Lambda, \tag{3.58}$$

$$v_{\rm imp}(\mathbf{p}_{\rm p},\mathbf{p}_{\rm t}) \quad = \quad \frac{\int_0^{2\pi} v_{\rm imp}(\mathbf{p}_{\rm p},\mathbf{p}_{\rm t};\ \Lambda)\,\Delta(\mathbf{p}_{\rm p},\mathbf{p}_{\rm t};\ \Lambda)\,{\rm d}\Lambda}{\int_0^{2\pi}\Delta(\mathbf{p}_{\rm p},\mathbf{p}_{\rm t};\ \Lambda)\,{\rm d}\Lambda}, \tag{3.59}$$

and the results were compared with those yielded by strict Monte-Carlo integrations in 3D (cf. Krivov et al. 2005). One can see that equation (3.55) does not show any noticeable dependence on the vertical extension of the disc beyond the term $\sin\varepsilon$ in the denominator. The impact velocity turned out to be more sensitive to the possible range of inclinations, and equation (3.56) is corrected to

$$v_{\rm imp}(\mathbf{p}_{\rm p},\mathbf{p}_{\rm t},\Lambda) \quad = \quad \sqrt{v_{\rm p}^2+v_{\rm t}^2-2v_{\rm p}v_{\rm t}\cos\overline{\gamma}} \tag{3.60}$$

with

$$\cos\overline{\gamma} \quad = \quad \frac{\cos\gamma}{\sqrt{1+(B\sin\varepsilon)^2}}. \tag{3.61}$$

The correction constant B was found empirically from the comparison with the Monte-Carlo integration: $B = 2/3$. Figure 3.3 shows examples of both quantities, $\Delta(\mathbf{p}_{\rm p},\mathbf{p}_{\rm t})$ (Eq. 3.58) and $v_{\rm imp}(\mathbf{p}_{\rm p},\mathbf{p}_{\rm t})$ (Eq. 3.59), with integrands given by equations (3.55) and (3.60), as well as their comparison with the Monte-Carlo results.

At this point, we are able to evaluate the gain and loss terms (3.30) and (3.32). For example, the gain term can be written as

$$\begin{aligned}\left(\frac{{\rm d}n}{{\rm d}t}\right)_{\rm gain}(m,\mathbf{p}) \quad &= \quad \int\limits_{\substack{a_{\rm p},e_{\rm p},m_{\rm p}\\ a_{\rm t},e_{\rm t},m_{\rm t}}}\cdots\int\int\limits_{\Lambda}\sigma\left[\overline{f}^{+}{v_{\rm imp}}^{+}\Delta^{+}+\overline{f}^{-}{v_{\rm imp}}^{-}\Delta^{-}\right]\\ &\times \quad n_{\rm p}n_{\rm t}\,\varphi(\Lambda)\,{\rm d}\Lambda\,{\rm d}a_{\rm p,t}\,{\rm d}e_{\rm p,t}\,{\rm d}m_{\rm p,t}.\end{aligned} \tag{3.62}$$

To avoid some ambiguities and singularities during the calculation, it is convenient to switch from

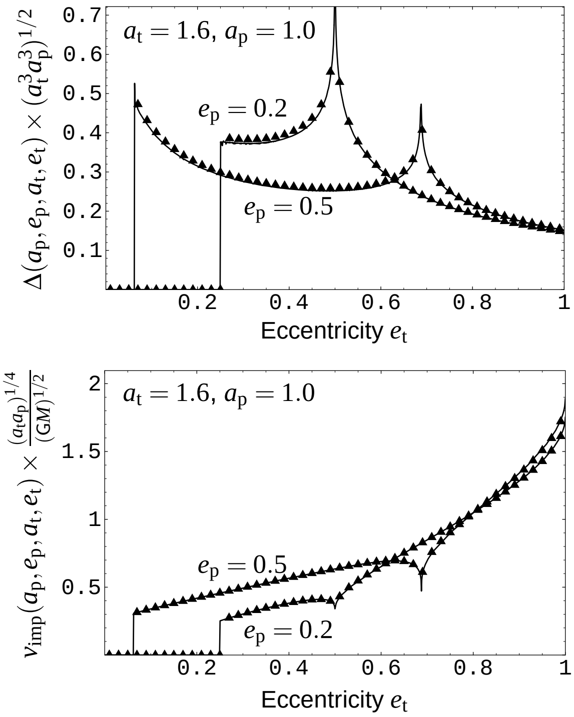

Figure 3.3: The Δ integral (top) and the impact velocities v_{imp} (bottom) for different combinations of semimajor axes and eccentricities of two colliding particles with (a_t, e_t) and (a_p, e_p). The disc's full-opening angle was set to $2\varepsilon = 17°$. For each set of orbits the "exact" values (symbols), obtained with a time-consuming Monte Carlo evaluation, are compared to the 2D-based approximations, equations (3.55) and (3.60) as solid lines. The semimajor axes are: $a_t = 1.6$, $a_p = 1.0$. The projectile's eccentricities are $e_p = 0.2$ and $e_p = 0.5$.

integration over Λ to integration over θ_t. The Jacobian gives

$$\frac{d\Lambda}{d\theta_t} = \frac{d(\theta_t - \theta_p)}{d\theta_t} = 1 - \frac{\partial\theta_p}{\partial\theta_t} = 1 - \frac{\frac{\partial r}{\partial\theta_t}}{\frac{\partial r}{\partial\theta_p}} = \frac{\frac{1}{r}\frac{\partial r}{\partial\theta_p} - \frac{1}{r}\frac{\partial r}{\partial\theta_t}}{\frac{1}{r}\frac{\partial r}{\partial\theta_p}}, \tag{3.63}$$

fitting quite well to $\sin\gamma$ (Eq. 3.53), because their numerators cancel out. The resulting probability can be written as

$$\Delta(\mathbf{p}_p, \mathbf{p}_t;\ \theta_t) = \left[8\pi^2 (a_p a_t)^{3/2} \sin\varepsilon \sqrt{\frac{p_t}{r(\theta_t)}\left(2 - \frac{r(\theta_t)}{a_p} - \frac{p_p}{r(\theta_t)}\right)}\right]^{-1}. \tag{3.64}$$

and is no longer symmetric with respect to the target and the projectile. In the ACE code, the Jacobian was not applied in its differential form, but used together with discretized steps of θ_t as a quotient of differences. Near singularities, that still appear, the program slightly shifts the eccentricity of both colliders to mimic the averaging over a whole bin.

One gets the same result as in equation (3.64) by starting from equation (3.34), reformulating the Dirac functions to depend on one collider's longitude of the pericentre, ϖ_t, as well as θ_t and θ_p. The Jacobian, transforming in 2D from the Cartesian case $\mathbf{r} = (x, y)$ to $r = r(\theta_t) = r(\theta_p)$ and $\Lambda = \theta_t^* - \theta_p^*$, is given by

$$J^{-1} = \left|\frac{\partial(x_t - x_p, y_t - y_p)}{\partial(\theta_t - \theta_t^*, \theta_p - \theta_p^*)}\right| = \frac{p_t p_p \,|e_t e_p \sin\Lambda + e_t \sin\theta_t - e_p \sin\theta_p|}{(1 + e_t\cos\theta_t)^2 (1 + e_p\cos\theta_p)^2}. \tag{3.65}$$

The required normalized densities in equation (3.34) are

$$\begin{aligned} \varphi(\theta_t) &= \frac{(1 - e_t^2)^{3/2}}{(1 + e_t\cos\theta_t)^2}, \\ \varphi(\theta_p) &= \frac{(1 - e_p^2)^{3/2}}{(1 + e_p\cos\theta_p)^2}, \\ \varphi(\varpi_t) &= \frac{1}{2\pi}. \end{aligned} \tag{3.66}$$

Finally, the 2D probability

$$\Delta_{\mathrm{2D}} = \int\limits_{\varpi_\mathrm{t},\theta_\mathrm{t},\theta_\mathrm{p}} \delta(\theta_\mathrm{t}-\theta_\mathrm{t}^*)\,\delta(\theta_\mathrm{p}-\theta_\mathrm{p}^*)\,J\,\varphi(\varpi_\mathrm{t})\;\varphi(\theta_\mathrm{t})\;\varphi(\theta_\mathrm{p})\,\mathrm{d}\varpi_\mathrm{t}\,\mathrm{d}\theta_\mathrm{t}\,\mathrm{d}\theta_\mathrm{p} \tag{3.67}$$

leads again to equation (3.64), after division by $2r\sin\varepsilon$ to account for 3D.

It is worthwile noting that equations (3.50) and (3.64) can be rewritten as

$$v_{\mathrm{p,t}} = \sqrt{\frac{\mathrm{G}M}{a_\mathrm{t}}(1-\beta_{\mathrm{p,t}})\left[\frac{2a_\mathrm{t}}{r}-\frac{a_\mathrm{t}}{a_{\mathrm{p,t}}}\right]}, \tag{3.68}$$

$$\Delta(\mathbf{p}_\mathrm{p},\mathbf{p}_\mathrm{t};\,\theta_\mathrm{t}) = \left[8\pi^2(a_\mathrm{t})^3(a_\mathrm{p}/a_\mathrm{t})^{3/2}\sin\varepsilon\sqrt{\frac{p_\mathrm{t}}{r(\theta_\mathrm{t})}\left(2-\frac{r(\theta_\mathrm{t})}{a_\mathrm{p}}-\frac{p_\mathrm{p}}{r(\theta_\mathrm{t})}\right)}\right]^{-1}. \tag{3.69}$$

One can see that the absolute scaling with the target's (or the projectile's) semi-major axis can be separated into a pre-factor. The remaining part only depends on the eccentricities, the anomaly θ_t, and the *ratio* of the semi-major axes. Thus, if only this remaining part is calculated and stored in advance and if a logarithmic binning of semi-major axes is used, only $2n-1$ combinations of $a_\mathrm{p}/a_\mathrm{t}$ are possible for n bins. Then, the need for memory scales linearly and not quadratically.

3.3.2 Characterization of Outcomes

Once impact velocity and rate are known, the course of a collision and its outcome are to be determined. The impact energy (see Eq. 2.16) sets the individual fates of the two colliders according to the following algorithm. First, it is checked whether half the impact energy suffices to disrupt the projectile, i.e. whether $E_\mathrm{imp}/2 > Q_\mathrm{D}^*(m_\mathrm{p})$. If this is the case, the projectile mass is added to the fragment mass budget and the surplus energy of the projectile's half are assumed to be imparted on the target. Otherwise, the projectile is assumed to be cratered but sticking to the target. Second, the remaining energy – at least half of the total impact energy – can either disrupt or crater the target and lead to the dispersal of either the total mass or part of it, respectively. What comes out is the sum of the two remnants – which can be zero if both are disrupted – and the joint fragment mass – which can be as large as the sum of both colliders. Hence, there are three different combinations for the mass of the combined remnant, m_rem, and of the fragments, m_crat:

$$m_\mathrm{rem} = 0 \quad \text{and} \quad m_\mathrm{crat} = m_\mathrm{p} + m_\mathrm{t}, \tag{3.70}$$

or

$$m_\mathrm{rem} = m_\mathrm{t} - m_\mathrm{crat}(m_\mathrm{t}, E_\mathrm{imp} - m_\mathrm{p}Q_\mathrm{D}^*(m_\mathrm{p})), \tag{3.71}$$

$$m_\mathrm{crat} = m_\mathrm{p} + m_\mathrm{crat}(m_\mathrm{t}, E_\mathrm{imp} - m_\mathrm{p}Q_\mathrm{D}^*(m_\mathrm{p})), \tag{3.72}$$

or

$$m_\mathrm{rem} = m_\mathrm{p} + m_\mathrm{t} - m_\mathrm{crat}(m_\mathrm{p}, E_\mathrm{imp}/2) - m_\mathrm{crat}(m_\mathrm{t}, E_\mathrm{imp}/2), \tag{3.73}$$

$$m_\mathrm{crat} = m_\mathrm{crat}(m_\mathrm{p}, E_\mathrm{imp}/2) + m_\mathrm{crat}(m_\mathrm{t}, E_\mathrm{imp}/2). \tag{3.74}$$

This quasi-equipartition of impact energy to the two colliders can only by assumed if their material strengthes are comparable.

In case of pure cratering, equations (2.28) and (2.29) can be applied for small and large craters, respectively. However, the transition between the two regimes is problematic (Thébault & Augereau 2007). Not only the exponents may differ, but also the coefficients Q_D^* and α. While Q_D^* is usually adopted in a bimodal form with strength regime and gravity regime, the related crater excavation coefficient α is commonly measured and modelled as size-independent – for centimetre-sized targets. But, scalings found by, e.g., Schmidt (1980) indicate a dependence of the crater volume V on the surface gravity g according to roughly $V \propto g^{-0.5\ldots-0.65}$. For constant bulk density, we would have $V \propto s^{-0.5\ldots-0.65}$. This dependence on s or g is not as strong as that of Q_D^* because reaccumulation outside the crater is not accounted for. In general, there is presumably a (size-dependent) functional relation between Q_D^* and α (which to find is beyond the scope of this work). Due to these uncertainties, the assumption is used that equation (2.29) with $\varepsilon = 1.23$ is valid even for small-scale craters.

The mass of the largest fragment is assumed to be given by equations (2.21) and (2.31) for catastrophic disruption and for cratering, repectively. Since the largest remnant can be smaller or larger than the original target, disruption, erosion, and growth can occur. However, this simplified growth model would need a mending if it were to be applied to the coagulation of micron-sized fluffy grains in gaseous, low-velocity environments.

Finally, the distribution of fragments is assumed to follow a single power-law $\mathrm{d}N \propto m^{-\eta}$ with $\eta \approx 1.83$ down to the smallest objects represented in the grid. (See Section 3.3.3.) This simplification is partly supported by the fact that the influence of the bimodal (or trimodal) power law on the resulting overall distribution is only moderate (Thébault et al. 2003).

3.3.3 The Fragment-Mass Distribution

The fragment-generating function f that enters equation (3.30) describes the number of fragments with $(m,\mathbf{p})$ that are produced by a destructive collision of parent bodies with $(m_\mathrm{p},\mathbf{p}_\mathrm{p})$ and $(m_\mathrm{t},\mathbf{p}_\mathrm{t})$. In its partly averaged incarnation, it is a product of two distributions:

$$\begin{aligned} f(m_\mathrm{p},\mathbf{p}_\mathrm{p};\, m_\mathrm{t},\mathbf{p}_\mathrm{t};\, m,\mathbf{p};\, \Lambda) &= g(m;\, m_\mathrm{p},\mathbf{p}_\mathrm{p};\, m_\mathrm{t},\mathbf{p}_\mathrm{t};\, \Lambda) \\ &\times\, h(m,\mathbf{p};\, m_\mathrm{p},\mathbf{p}_\mathrm{p};\, m_\mathrm{t},\mathbf{p}_\mathrm{t};\, \Lambda). \end{aligned} \tag{3.75}$$

Here, g represents the mass distribution characterized in Section 3.3.2:

$$g(m) = (2-\eta)\cdot m_\mathrm{crat}\cdot\left(\frac{m_\mathrm{x}}{m}\right)^\eta\cdot\frac{1}{m_\mathrm{x}^2}\,\Theta(m_\mathrm{x}-m)+\delta(m-m_\mathrm{rem}), \tag{3.76}$$

with $\eta \approx 1.83$, the Heaviside step function $\Theta(x)$, and the Dirac distribution $\delta(x)$. This single power-law is a cruder approximation than the one used by Thébault & Augereau (2007).

Numerically, the cumulative fragment mass distribution is more interesting:

$$M_\mathrm{f}(<m) \equiv \int_0^m \tilde{m}g(\tilde{m})\mathrm{d}\tilde{m}, \tag{3.77}$$

$$M_\mathrm{f}(<m) = \begin{cases} m_\mathrm{crat}\cdot\left(\frac{m_\mathrm{x}}{m}\right)^{2-\eta} & \text{for } m < m_\mathrm{x}, \\ m_\mathrm{crat} & \text{for } m_\mathrm{x} < m < m_\mathrm{rem}, \\ m_\mathrm{t}+m_\mathrm{p} & \text{for } m_\mathrm{rem} < m. \end{cases} \tag{3.78}$$

Assuming bin widths given by a logarithmic grid with steps μ, the fragment mass falling into bin i is given by

$$M_{\mathrm{f},i} = M_\mathrm{f}(<\mu^{\frac{1}{2}}m_i) - M_\mathrm{f}(<\mu^{-\frac{1}{2}}m_i), \tag{3.79}$$

where

$$\frac{M_\mathrm{f}(<\mu^{\frac{1}{2}}m)}{M_\mathrm{f}(<\mu^{-\frac{1}{2}}m)} = \mu^{2-\eta} = \mathrm{const} \quad \text{for } \mu m < m_\mathrm{x}. \tag{3.80}$$

Thus, one can start with calculating $M_\mathrm{f}(<\mu^{-\frac{1}{2}}m_1)$, i.e. the mass in fragments that are too small for the grid, and $M_{\mathrm{f},1}$, the mass in the lowest mass bin. Then, every subsequent mass bin receives by a factor of $\mu^{2-\eta}$ more mass in fragments than its predecessor. The upper limit on the total fragment mass is m_crat.

If there exists a remnant, i.e. if the target is only cratered, some of the objects in the target bin $m_i = m_\mathrm{t}$

are growing or are eroded to an adjacent bin. For erosion ($m_{\rm rem} < m_i$), this corresponds to mass changes in bins m_i and m_{i-1} given by

$$M'_i = M_i - \frac{\ln(m_1/m_{\rm rem})}{\ln\mu}, \quad (3.81)$$

$$M'_{i-1} = M_{i-1} + \frac{\ln(m_i/m_{\rm rem})}{\ln\mu}. \quad (3.82)$$

For growth ($m_{\rm rem} > m_i$), the changes are given by

$$M'_i = M_i - \frac{\ln(m_{\rm rem}/m_i)}{\ln\mu}, \quad (3.83)$$

$$M'_{i+1} = M_{i+1} + \frac{\ln(m_{\rm rem}/m_i)}{\ln\mu}. \quad (3.84)$$

The according numbers of particles in the bins are $N_i = M_i/m_i$. With the exception of fragments that are too small, this procedure naturally preserves the total mass.

The fragments' distribution of orbital elements, $\overline{h}$, is detailed in Section 3.3.4.

3.3.4 Orbital Elements of Fragments

Initially, a cloud of fragments, produced by a disruptive collision, carries the sum of the momenta of both colliders in roughly one and the same direction. Let the function h denote the resulting orbital element distribution of the fragments (averaged over unimportant variables). This function evaluates whether or not a fragment of mass m, produced in a collision between $(m_{\rm p}, \mathbf{p}_{\rm p})$ and $(m_{\rm t}, \mathbf{p}_{\rm t})$ at the apsidal angle Λ, can have orbital elements $\mathbf{p} = (a, e)$. The fragments have zero relative velocities, as we assume maximal collisional damping. Therefore, $h(m, a, e;\ m_{\rm p}, \mathbf{p}_{\rm p};\ m_{\rm t}, \mathbf{p}_{\rm t};\ \Lambda)$ is proportional to

$$\delta[a - a(m_{\rm p}, \mathbf{p}_{\rm p};\ m_{\rm t}, \mathbf{t}_{\rm p};\ m;\ \Lambda)] \quad (3.85)$$

and

$$\delta[e - e(m_{\rm p}, \mathbf{p}_{\rm p};\ m_{\rm t}, \mathbf{t}_{\rm p};\ m;\ \Lambda)], \quad (3.86)$$

where $a(m_{\rm p}, \mathbf{p}_{\rm p};\ m_{\rm t}, \mathbf{p}_{\rm t};\ m;\ \Lambda)$ and $e(m_{\rm p}, \mathbf{p}_{\rm p};\ m_{\rm t}, \mathbf{p}_{\rm t};\ m;\ \Lambda)$ are given by equations (3.93) and (3.94). The function h is normalized to unity:

$$\int h(m, a, e;\ m_{\rm p}, \mathbf{p}_{\rm p};\ m_{\rm t}, \mathbf{p}_{\rm t};\ \Lambda)\, \mathrm{d}a\, \mathrm{d}e = 1. \quad (3.87)$$

The resulting momentum is that of the centre of mass and, in the 2D case, is described by two conservation laws, one for the radial component and one for the angular:

$$m_{\rm sum}\dot{r} = m_{\rm p}\dot{r}_{\rm p} + m_{\rm t}\dot{r}_{\rm t}, \quad (3.88)$$

$$m_{\rm sum} r\dot{\theta} = m_{\rm p} r\dot{\theta}_{\rm p} + m_{\rm t} r\dot{\theta}_{\rm t}, \quad (3.89)$$

where $m_{\rm sum} = m_{\rm p} + m_{\rm t}$. Krivov et al. (2005) considered the angular momentum only. The fragments were all placed on the orbit of the centre of mass and remained there due to their being too large to show significant response to radiation pressure. Now that we concentrate on micron-sized dust, we extend the fragment-generating function to consider the distance $r = r_{\rm p} = r_{\rm t}$, at which the parent particles p and t collide, and to include radiation pressure described by the β-ratios. Using the equation of conic section (Eq. 3.36) with $p = a(1 - e^2)$ and the derivatives

$$r\dot{\theta} = \frac{L}{mr}, \qquad \dot{r} = \frac{L}{mr}\left(\frac{1}{r}\frac{\partial r}{\partial \theta}\right) \quad (3.90)$$

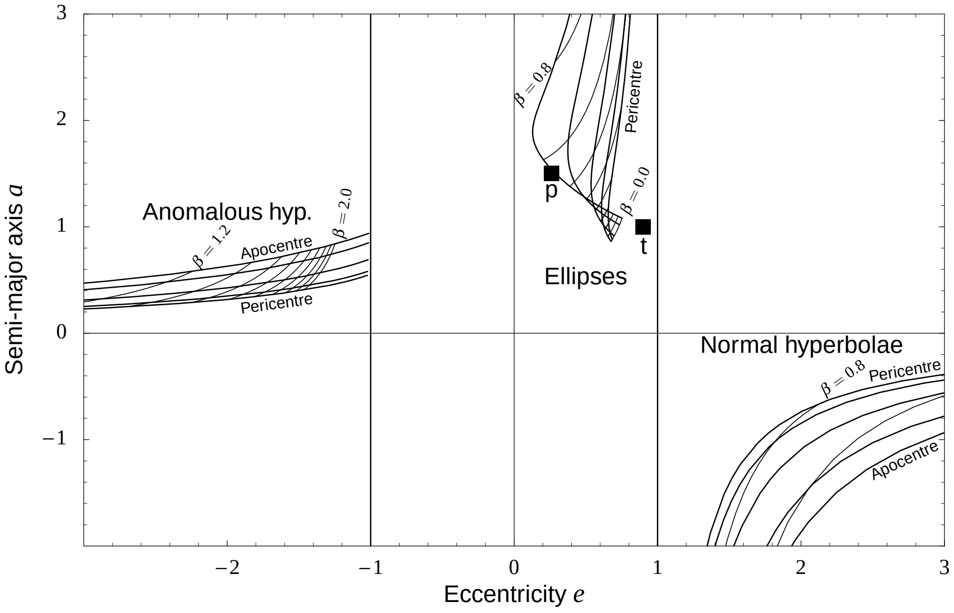

Figure 3.4: Fragments' orbits produced by collision of two particles ($m_\mathrm{t} = 2m_\mathrm{p} = 2$, $a_\mathrm{t} = 1$, $e_\mathrm{t} = 0.9$, $\beta_\mathrm{t} = 0$, $a_\mathrm{p} = 1.5$, $e_\mathrm{p} = 0.26$, $\beta_\mathrm{p} = 0$) whose locations are shown by the two boxes. Lines of equal β-ratio (at steps of 0.1 from 0.0 to 2.0, $\beta = 1$ is excluded) and a running ejection point are shown, as are lines of equal ejection point (at true anomaly steps of 45°starting at the pericentre) and running β. The upper-left part contains anomalous hyperbolae, the ellipses are located in the middle, and the normal hyperbolae are found at the lower-right. The constant GM is set to unity.

with

$$
\begin{aligned}
L &= m\sqrt{\mathrm{G}M(1-\beta)p}, && (3.91)\\
\frac{1}{r}\frac{\partial r}{\partial \theta} &= \pm\sqrt{\frac{r}{p}\left(2-\frac{r}{a}-\frac{p}{r}\right)} && (3.92)
\end{aligned}
$$

for the colliders and the resulting fragments, a lengthy but straightforward algebra results in

$$
\begin{aligned}
\frac{r}{a} &= 2-\frac{m_\mathrm{p}^2}{m_\mathrm{sum}^2}\cdot\frac{1-\beta_\mathrm{p}}{1-\beta}\left[2-\frac{r}{a_\mathrm{p}}\right]-\frac{m_\mathrm{t}^2}{m_\mathrm{sum}^2}\cdot\frac{1-\beta_\mathrm{t}}{1-\beta}\left[2-\frac{r}{a_\mathrm{t}}\right]\\
&\quad -2\frac{m_\mathrm{p}m_\mathrm{t}}{m_\mathrm{sum}^2}\frac{\sqrt{(1-\beta_\mathrm{p})(1-\beta_\mathrm{t})}}{1-\beta}\left[\frac{1}{r}\sqrt{p_\mathrm{p}p_\mathrm{t}}\right.\\
&\quad \left.\pm\sqrt{\left(2-\frac{r}{a_\mathrm{p}}-\frac{p_\mathrm{p}}{r}\right)\left(2-\frac{r}{a_\mathrm{t}}-\frac{p_\mathrm{t}}{r}\right)}\right], && (3.93)\\
e &= \pm\left[1-\frac{1}{a}\left(\frac{m_\mathrm{p}^2}{m_\mathrm{sum}^2}\frac{1-\beta_\mathrm{p}}{1-\beta}p_\mathrm{p}+\frac{m_\mathrm{t}^2}{m_\mathrm{sum}^2}\frac{1-\beta_\mathrm{t}}{1-\beta}p_\mathrm{t}\right.\right.\\
&\quad \left.\left.+2\frac{m_\mathrm{p}m_\mathrm{t}}{m_\mathrm{sum}^2}\frac{\sqrt{(1-\beta_\mathrm{p})(1-\beta_\mathrm{t})}}{1-\beta}\sqrt{p_\mathrm{p}p_\mathrm{t}}\right)\right]^{\frac{1}{2}}. && (3.94)
\end{aligned}
$$

Here, the sign of e is equal to that of $(1-\beta)$, yielding anomalous hyperbolae with $e < 0$ for $\beta > 1$. Given $a_\mathrm{p,t}$, $e_\mathrm{p,t}$, $\beta_\mathrm{p,t}$, and $m_\mathrm{p,t}$ for the colliders, we are now able to calculate a and e for all fragments (all β) and positions r. The influence of θ (or r) and β on the fragments' orbital elements is demonstrated in Fig. 3.4.

The actual algorithm calculates for each step of θ (or r) the according a and e (together with Δ and v_{imp}), then assigns the approriate bins and finally interpolates linearly between the steps. (The latter is necessary only for barely bound and unbound grains where orbital differences are greater.)

3.4 Transport Mechanisms

3.4.1 General Description

Unlike collisions, transport of material in the phase space is local, i.e. the change of orbital elements of an individual object can be characterized by time derivatives, e.g., $\dot{a}$ and $\dot{e}$. In the statistical/kinetic approach, this shift of individual objects corresponds to the displacement of a portion of the "content" of one bin to one or more adjacent bins. The material "streams" through the grid. Formally, this mechanism is described by the transport term in the continuity equation (3.17), the integral/discrete formulation of which is

$$\dot{n}_i = \dot{n}_i|_{\mathrm{gain}} - \dot{n}_i|_{\mathrm{loss}} - \oint\limits_{(S_i)} n(\mathbf{p})\mathbf{u}(\mathbf{p})\mathrm{d}\mathbf{S}, \tag{3.95}$$

where S_i is the surface of bin i, $\mathbf{S}$ the normal vector to this surface, and $\mathbf{u} \equiv \dot{\mathbf{p}}$ the velocity of the flux through the phase space.

For usual rectangular grids like the ones used here, this equation simplifies to

$$\dot{n}_i = \dot{n}_i|_{\mathrm{gain}} - \dot{n}_i|_{\mathrm{loss}} - n_i \sum_j \frac{\dot{p}_{ij}}{\Delta p_j} + \sum_{jh} n_h \frac{\dot{p}_{hj}}{\Delta p_j}, \tag{3.96}$$

where $\dot{p}_{ij}$ denotes the rate of change of phase space variable j for bin i, and Δp_j the width of the bins along variable j. The sum over h denotes the *influx* of material from neighbouring bins h – at most twice as many bins as there are phase space variables.

Once the change of phase space variables due to specific drag forces is known, i.e. once the $\dot{p}_{ij}$ are known, the forces can readily be implemented in the kinetic theory.

Note that the cratering described by equations (3.82) and (3.84) can also be considered as the implementation of this method for transport within the logarithmic *mass* grid.

3.4.2 Poynting-Robertson and Wind Drag

Following Burns et al. (1979), P-R drag results in a change of semi-major axis and ecentricity given by

$$\dot{a}_{\mathrm{P-R}} = -\frac{\beta \mathrm{G} M}{ca} \frac{2+3e^2}{(1-e^2)^{3/2}}, \tag{3.97}$$

$$\dot{e}_{\mathrm{P-R}} = -\frac{5\beta \mathrm{G} M}{2ca^2} \frac{e}{(1-e^2)^{1/2}}. \tag{3.98}$$

For use with the logarithmic semi-major-axis grid, we need

$$\left.\frac{\mathrm{d}(\ln a)}{\mathrm{d}t}\right|_{\mathrm{P-R}} = -\frac{\beta \mathrm{G} M}{ca^2} \frac{2+3e^2}{(1-e^2)^{3/2}}. \tag{3.99}$$

Similary, the equations for wind drag are

$$\dot{a}_{\mathrm{wd}} = \dot{a}_{\mathrm{P-R}} \frac{\beta_{\mathrm{wp}} c}{\beta_{\mathrm{rp}} v_{\mathrm{w}}}, \tag{3.100}$$

$$\dot{e}_{\mathrm{wd}} = -\dot{e}_{\mathrm{P-R}} \frac{\beta_{\mathrm{wp}} c}{\beta_{\mathrm{rp}} v_{\mathrm{w}}}. \tag{3.101}$$

Confer equation (2.39) and note that the effect of wind drag is independent of the wind speed.

3.5 The Integrator

The basic first-order Euler scheme for integration translates differential coefficients to difference quotients:

$$\frac{\mathrm{d}\mathbf{n}}{\mathrm{d}t} = \frac{\Delta\mathbf{n}}{\Delta t}. \tag{3.102}$$

For a linear system with $\dot{\mathbf{n}} = \mathbf{A}\mathbf{n}$ with matrix $\mathbf{A}$, this leads to the explicit expression

$$\mathbf{n}_{m+1} = \mathbf{n}_m + (t_{m+1} - t_m)\mathbf{A}_m\mathbf{n}_m \tag{3.103}$$

for the progression from time step m to time step $m+1$. For a proper definition of $\mathbf{A}$, see section 3.2.2. In constrast, implicit integration is based on

$$n_{m+1} = \left[\mathbf{1} - (t_{m+1} - t_m)\mathbf{A}_m\right]^{-1}\mathbf{n}_m. \tag{3.104}$$

Both methods are accurate to the first order in Δt. The advantage of the fully implicit method is that it is stable even for so-called stiff systems, where short timescales and long timescales coexist (Press et al. 1992) – like in a collisionally evolving disc with dust and planetesimals. The disadvantage is the necessity of inverting the matrix $\mathbf{1} - \mathbf{A}\Delta t$ for each time step. The dimension of this (time-dependent) matrix is $N \times N$ for a number of N bins, which can easily exceed a total of 10^9 entries.

An approach using a more accurate fourth-order Runge-Kutta integration scheme (Press et al. 1992) also failed because the stiffness could not be overcome.

As a compromise, the following scheme is used:

$$\frac{\mathrm{d}\mathbf{n}}{\mathrm{d}t} = \left.\frac{\mathrm{d}\mathbf{n}}{\mathrm{d}t}\right|_{\mathrm{const}} + \mathbf{A}'\mathbf{n}, \tag{3.105}$$

where $\mathbf{A}'$ is defined as diagonal matrix:

$$A'_{jk} \equiv A_{jk}\delta_{jk}. \tag{3.106}$$

Thus, A'_{jk} basically represents the terms in the master equation that are linear in n_j. The term labelled with "const" sums the off-diagonal elements of the full matrix. As a result of this (still linear) simplification, the set of equations (3.105) is mutually independent and can easily be integrated. Then, the j^{th} component of $\mathbf{n}$ for timestep $m+1$ reads

$$n_{j,m+1} = \left(\dot{n}_{j,m}|_{\mathrm{const}} + n_{j,m}\right)\exp(A'_{jk,m}\cdot\Delta t) - \frac{1}{A'_{jk,m}}\dot{n}_{j,m}|_{\mathrm{const}}. \tag{3.107}$$

In asymptotic approximation, one would obtain the Eulerian standard

$$n_{j,m+1} = n_{j,m+1} + \dot{n}_{j,m}|_{\mathrm{const}}\Delta t \tag{3.108}$$

for $\Delta t \to 0$ and the constant

$$n_{j,m+1} = \frac{1}{A'_{jk,m}}\dot{n}_{j,m}|_{\mathrm{const}} \tag{3.109}$$

for $\Delta t \to \infty$.

In order to make this clearer, one should note that the major contribution to the linear term comes from the loss terms, while the constant term is dominated by the gain: this reads

$$\dot{n}_j\big|_{\rm const} \approx \dot{n}_j\big|_{\rm gain}, \tag{3.110}$$

$$A'_{jk} \approx \frac{\dot{n}_j\big|_{\rm loss}}{n_j} \tag{3.111}$$

and leads to

$$n_{j,m+1} \approx \frac{\dot{n}_{j,m}\big|_{\rm gain}}{\dot{n}_{j,m}\big|_{\rm loss}} n_{j,m} \tag{3.112}$$

for $\Delta \longrightarrow \infty$. Thus, convergence towards a (temporary) equilibrium is guaranteed. From the equations for A_{jk} one can see that $A'_{jj} = T_j^{-1}$, i.e. the inverse collisional lifetime.

Due to the different timescales T_j for small and large objects and for short- and long-term evolution, an adaptive step size control is used, which monitors the maximum change per bin and time step. As a result, the ratio between step size and current system age is roughly kept constant at a value of around 10^{-3} (except for the initial phase).

3.6 The ACE Code

For all the presented numerical runs, a C++-based collisional code was used (ACE, Analysis of Collisional Evolution). The code numerically solves the Boltzmann-Smoluchowski kinetic equation to evolve a disc of solids in a broad range of sizes (from sub-micrometres to about one hundred kilometres), orbiting a primary in nearly-Keplerian orbits (gravity + direct radiation pressure + drag forces) and experiencing disruptive collisions. Collisions are simulated with available material- and size-dependent scaling laws for fragmentation and dispersal in both strength and gravity regime. The current version implements a 3-dimensional kinetic model, with masses, semi-major axes, and eccentricities as phase space variables. This approach automatically enables a study of the simultaneous evolution of mass, spatial, and velocity distribution of particles. The code is fast enough to easily follow the evolution of a debris disc over Gyr timescales. Typical long runs presented here are done within a few days on a desktop computer.

4 Dust in Collisional Equilibrium

4.1 Introduction: Vega as an Example

The so-called Vega phenomenon for main-sequence stars refers to a mid-infrared excess in the observed spectrum over the purely stellar emission. It was discovered in 1983 by the IRAS mission, at first for Vega itself (Aumann et al. 1984), and was soon attributed to a population of cold dust surrounding the star. From the analysis of the spectral energy distribution in the spectral range from 12 µm (Aumann et al. 1984; Beichman et al. 1988) to 1.3 mm (Chini et al. 1990), conclusions about the properties of the assumed disc were made, for instance, the existence of an inner gap was inferred from the absence of hot grains. The first spatially resolved submillimetre images of the Vega disc were obtained with the SCUBA camera on the JCMT on Hawaii (Holland et al. 1998), followed by other groups (Koerner et al. 2001; Wilner et al. 2002), who concentrated on finding asymmetries. Recently, Su et al. (2005) observed the Vega system at 24, 70, and 160 µm with the Spitzer space telescope and found radial profiles of the Vega disc to be nearly rotationally symmetric and featureless. The rings reported by Marsh et al. (2006) at wavelength of 350 and 450 µm fall in between clumps and featureless symmetry. The absence of angular asymmetries and substructure in the infrared makes the Vega disc an ideal application of our approach.

(This chapter is primarily based on work done for “Krivov et al. (2006)”, though containing updated and extended discussion.)

4.2 Description of Numerical Runs

The initial size distribution is set to the well-known relation $n(s) \propto s^{-3.5}$, starting at a minimum radius of ≈ 0.1 µm. The total mass strongly depends on the upper mass cut-off (proportional to $\sqrt{s_{\max}}$). To conform with previous mass estimates (Holland et al. 1998; Su et al. 2005), the total observable mass was set to be made up of grains up to a limiting radius of 1.5 mm. Grains larger than this – the population of parent bodies – follow the same power law, but deliver additional mass. The mass range used was 10^{-14} g to 3.56×10^{14} g. Thus, setting an observable mass of $\approx 0.5\ M_{\text{Moon}}$ (Lunar masses) leads to a total initial mass of close to 300 M_{Moon} or 3.5 $M_{\oplus}$ (Earth masses). This range was covered by a grid of 70 bins with logarithmic steps with a step factor of 2.6. The equivalent size grid has steps with factors of 1.37.

To model the distribution of orbital elements, from which then the spatial distribution of dust material was calculated, a mesh of the semimajor axes from -400 to 400 AU with linear steps of 20 AU, and eccentricity bins from -3 to 3 with width of 0.125 was used, as depicted in Fig. 4.7. According to Su et al. (2005) and Dent et al. (2000), for the Vega disc, an initial distribution of semimajor axes between 80 AU and 120 AU was adopted and chosen in such a way that, for zero eccentricities, the normal optical depth τ would be constant in this distance range. The distribution of semimajor axes outside $a = 120$ AU was taken to be a power law, corresponding to an optical depth $\tau(a) \propto a^{\alpha}$. Different values of the index α were tested, see below. No material was placed initially inside $a = 80$ AU. The initial distribution of eccentricities both in the “ring” between 80 AU and 120 AU and in the outer disc outside 120 AU was set uniform from zero to an upper limit of $e_{\max} = 1/8$ or $3/8$, depending on the run. The vertical extension of the disc is defined by a full-opening angle, which was arbitrarily set to $2\varepsilon = 17°$.

The optical and mechanical properties of dust in the disc are wildly unknown, and two types of grains are adopted here: “rocky” and “icy” ones. Assuming a mixture of 70% astronomical silicate of 3.5 g/cm^3 (Laor & Draine 1993), 30% amorphous carbon of 1.85 g/cm^3 (Zubko et al. 1996) and porosity close to zero, the effective grain bulk density used here for “rocky” grains is 3.0 g/cm^3. The mean radiation pressure efficiency $\langle Q_{\mathrm{pr}} \rangle$, describing the momentum transfer from radiation to grain, is set to unity. The dependence of the critical energy for disruption on the grain size is given by equation (2.27). For rocky material, the value of Q_{D}^{*} at a size of 1 m was set to 10^6 erg/g, and the slope b_{s} for this strength regime was set to -0.24, although these values are not well defined by theoretical and laboratory work. To check how strongly the results depend on the adopted material, one run was done for "icy" grains of low bulk density (1 g/cm^3) and mechanical strength ($Q_{\mathrm{D}}^{*} = 2 \times 10^5$ erg/g at a size of 1 m). In equation (2.21), $c = 1.24$ was used for rock (Paolicchi et al. 1996) and $c = 0.91$ for ice (Arakawa 1999).

The values used here for Q_{D}^{*} have been criticized by Thébault & Augereau (2007) as being too low. The strength of the material and the derived lifetimes against disruptive collisions should thus be considered as lower limits.

4.3 Size Distribution

4.3.1 The Lack of Unbound Grains

The resulting size distributions show strong fingerprints of the radiation pressure. The most noticeable feature is connected with the particle size where $\beta = 1$, so that the radiation pressure equals gravity. Below this size, bound orbits are impossible (Fig. 4.1), and the grains are blown away on a short timescale. This strong depletion results in a jump in the size distribution. The height of this jump at the blowout radius can be described in the following way. The equilibrium number of objects of type x is given by their gain rate $\dot{n}|_{\mathrm{gain}}$ and their lifetime T_x:

$$n_x = \frac{\dot{n}|_{\mathrm{gain}}}{T_x}. \tag{4.1}$$

For collision-dominated populations, the lifetime is inversely proportional to the number of potentially catastrophic colliders; for drag forces and radiative blowout, it is only depending on object size. Therefore, a discontinuity in the size distribution is introduced: the cut-off at the blowout limit. Since the production rate can be assumed continuous, the height of the saltus is determined by equation (4.1) and the ratio of the lifetimes at both sides. Hence, we find

$$\frac{n_\beta}{n_\alpha} = \frac{T_\beta}{T_\alpha}. \tag{4.2}$$

While the blowout grains leave the system on orbital timescales, i.e. $T_\beta \sim 10^2 \ldots 10^3$ yr, the actual values for T_α depend on the collisional timescales and are discussed in section 4.3.2.

Although the height of the jump discontinuity in the size distribution is variable, it would vanish only if the collisional lifetime of small α-meteoroids were comparable with the blowout timescale, i.e. with orbital timescales. Thus, a continuous (power-law) size distribution that bridges the blowout size can be sustained by a collisional cascade *only* in very dense discs. (See section 4.5 for a more detailed discussion.)

4.3.2 The Wave

Due to the lack of smaller impactors, grains slightly above the blowout limit are overabundant, thereby collisionally reducing the number of grains of the next larger population, and so on. This dependence produces a well-known wavy pattern in the *size or mass distribution* (e.g., Campo Bagatin et al. 1994; Durda & Dermott 1997; Thébault et al. 2003), whose "wavelength" depends on the ratio of the average impact energy available and the critical specific energy Q_{D}^{*} needed to disrupt a given target. The first is controlled by impact velocities, which depend on the disc's layout. The range of inclinations and especially the range of eccentricities are important, because they determine the orbits' crossing angles. The critical energy Q_{D}^{*}, on the other hand, is determined by material properties.

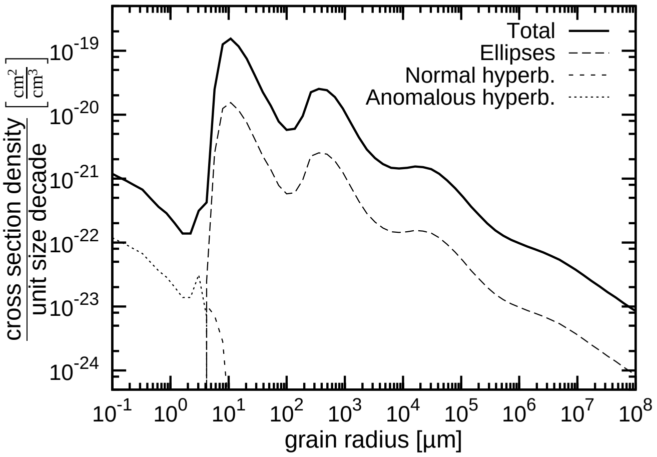

Figure 4.1: Grain size distribution at 100 AU after 10 Myr for a rocky disc with an initial outer profile $\propto r^{-4}$ and eccentricities from 0 to 0.375 (solid line). The contributions from the three different types of orbits, shifted down by one order of magnitude for better visibility, are shown by long-dashed (ellipses), short-dashed (normal hyperbolas), and dotted (anomalous hyperbolas) lines.

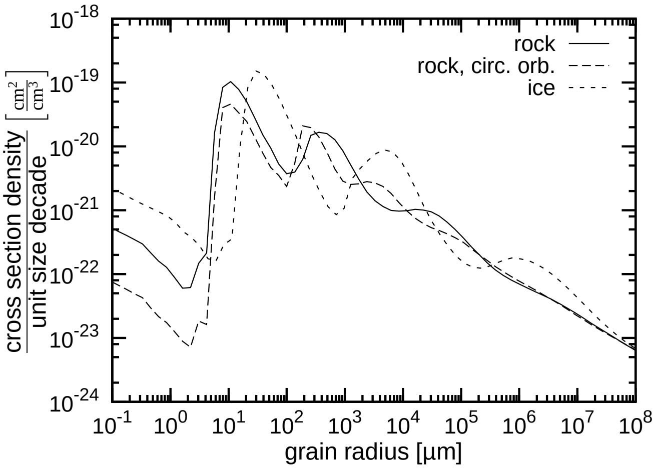

Figure 4.2: Grain size distribution at 100 AU and 10 Myr (4.5 Myr for "ice") for different eccentricity ranges: 0.0 to 0.375 for "rock" and "ice", and only 0.0 to 0.125 for "circular" orbits. The dashed lines are rescaled to coincide with the solid at large radii. The horizontal shift of the maximum for icy grains is largely due to a different bulk density.

As shown in Fig. 4.2, the disc's and the dust's set-up can have a noticeable influence on the size distribution. Low maximum eccentricities shorten the pattern's wavelength due to lower impact velocities leading to the critical impactor's size coming closer to the given target's. In contrast, the fluffy constitution of icy grains enlarges the gap between the target mass and the minimum mass needed to disrupt it at a given impact velocity. Furthermore, it shifts the lower cut-off of the particle radius to higher values, according to the ratio of bulk densities, which is here 3:1. The example of the inner disc of β Pictoris (Thébault et al. 2003), where the relative velocities are presumably high compared to the outer Vega disc, shows that the wave can easily reach into the macroscopic size regime. In their models, which include cratering collisions, the second peak is located at a size of around 1 m. (See section 4.3.4.)

It should be noted that a realistic disc cannot be built up of perfectly homogeneous material, which implies a dispersion of densities, fragmentation energies etc. This could weaken or smear the waviness of the size distribution. This smearing is artificially reproduced in part due to the numerics on a discrete grid: dispersion due to limited accuracy accumulates and mimics the damping of the wave towards larger objects. This effect can partly explain differences in the waviness between this work and the work by Thébault & Augereau (2007).

The latter provide an empirical fit to the wave up to the second peak at around one hundred times the blow-out radius, i.e. the size of the largest grain still blown out. They show that this deviation from a simple power law can measurably influence the observable fluxes in Spitzer's MIPS bands and Herschel's PACS and SPIRE bands. However, this empirical fit is not valid for larger objects and, therefore, does not provide a link between dust and planetesimals.

The *temporal evolution* of the particle size distribution of a modelled Vega disc is shown in Fig. 4.3 and the size-dependent collisional lifetimes in Fig. 4.4. The larger the particles, the longer the collisional

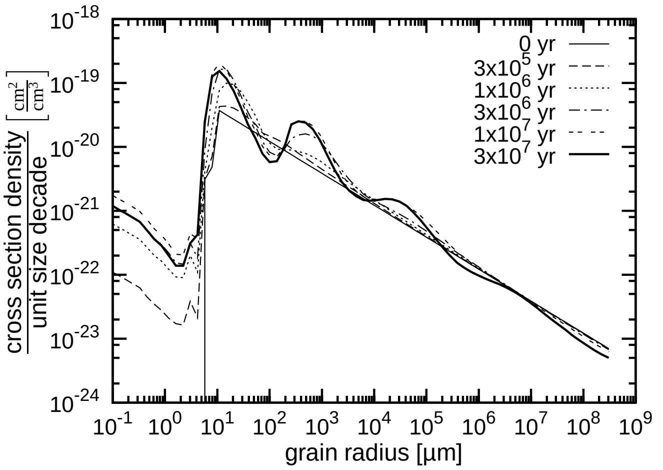

Figure 4.3: Evolution of the size distribution of the disc of Fig. 4.1 at a distance of 100 AU.

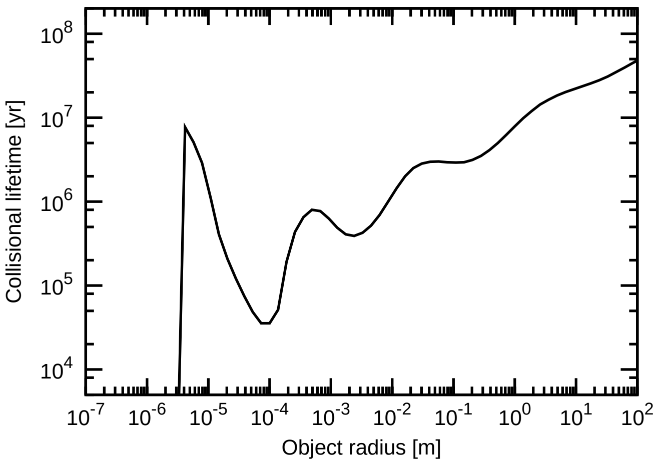

Figure 4.4: Size dependence of the collisional lifetime of the material in the disc of Fig. 4.1.

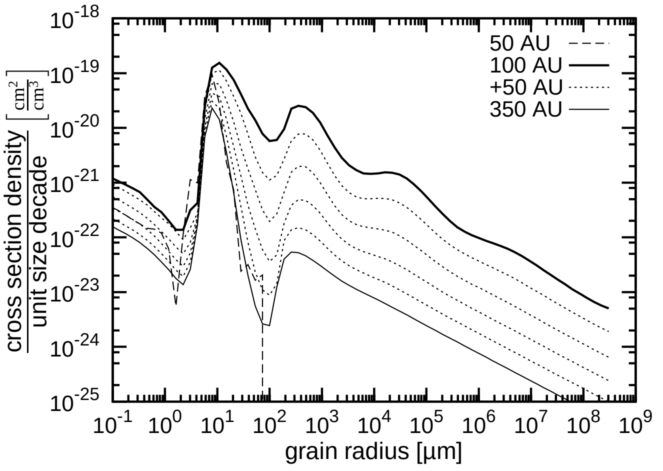

Figure 4.5: Grain size distribution at distances from 50 AU to 350 AU in steps of 50 AU after 30 Myr. The initial disc is the same as in Fig. 4.1. The inner boundary of semimajor axes was placed at 80 AU. Therefore, only a small fraction of grains on sufficiently eccentric orbits contribute to the density at 50 AU.

timescales – except for the case of the barely bound grains – and the more time does it take for the size distribution to deviate significantly from the initial power law and to converge towards a quasi-steady state distribution whose absolute values are subject to change due to the amount of material delivered by collisions of larger bodies. Similarly, the comparison of different radial distances at the same time (Fig. 4.5) shows slower evolution at regions that are farther out with lower number densities and decreased impact velocities, where the latter also result in a reduced wavelength of the pattern. Concerning the average, one can conclude that around 1–10 Myr are necessary for the population of grains up to a few hundred micron in size to reach the quasi-steady state. Confer Chapter 5 for a detailed

Table 4.1: Masses of the modelled discs producing $0.5 M_{\mathrm{Moon}}$ of dust.

Model			Quasi-steady state	
Material	Slope α	$e_{\max}$	Total mass	Mass-loss rate
rock	2	0.125	$2.5\ M_{\oplus}$	$0.9\ M_{\oplus}/\mathrm{Gyr}$
rock	2	0.375	$1.4\ M_{\oplus}$	$1.7\ M_{\oplus}/\mathrm{Gyr}$
rock	4	0.375	$1.1\ M_{\oplus}$	$2.9\ M_{\oplus}/\mathrm{Gyr}$
rock	∞	0.375	$0.7\ M_{\oplus}$	$9.0\ M_{\oplus}/\mathrm{Gyr}$
ice	2	0.375	$1.6\ M_{\oplus}$	$19.8\ M_{\oplus}/\mathrm{Gyr}$

analysis of the the size distribution's temporal change and of the timescales and scaling laws.

4.3.3 Disc Mass and Mass Loss

The *total masses* of the model discs are listed in Table 4.1 for different runs. The "rocky" discs are made up of grains from 0.1 µm to 300 m, the "icy" particles span a size range from 0.14 µm to 430 m, so that the same mass range is covered. The given masses and loss rates for ice are probably less realistic, as the real dust is assumed to be a mixture of silicates and carbonaceous material. The derived total mass, which determines the absolute values of ordinates, is very sensitive to where the upper cut-off is set, especially when considering the wave pattern. However, this upper cut-off, which is unknown, has *no* influence on the absolute mass loss, since mass is lost only through production and blowout of β-meteoroids.

The relative mass loss, $\dot{M}/M$, shows that all discs provide enough material to sustain the *current* debris production over at least 80 Myr up to 2.8 Gyr. A higher mass-loss rate of the icy disc stems from the fact that ice is easier to destroy than rock (smaller Q_{D}^{*} and, therefore, shorter collisional lifetimes). The existence of even larger parent bodies would further prolong the disc's half-life and increase the total mass (confer Section 5.4.2).

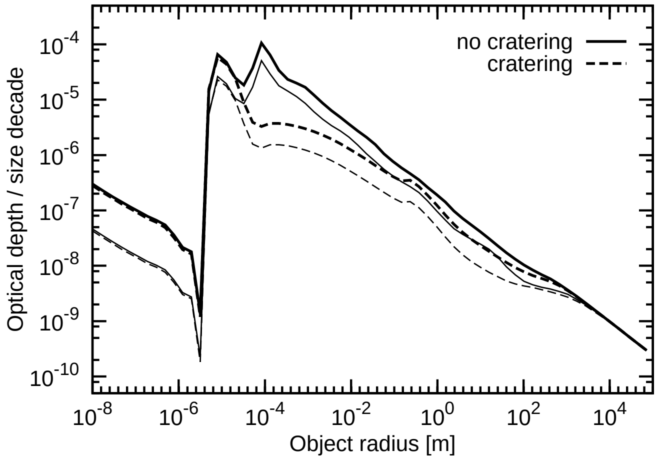

Figure 4.6: Quasi-steady-state size distribution when considering only disruptive collisions (*solid*) or also cratering collisions (*dashed*). Thick lines denote an age of 300 Myr, thin lines an age of 3 Gyr.

While Su et al. (2005) estimate the current mass loss due to blowout of small grains as 6×10^{14} g/s or 3200 $M_\oplus$/Gyr, we conclude that mass-loss rates of 1 to 20 $M_\oplus$/Gyr (Table 4.1) are consistent with an observed amount of 0.5 M_Moon of submillimetre-sized dust. A linear extrapolation by 350 Myr back in time would lead to initital disc masses several orders of magnitude below the 330–3300 Jupiter masses given by Su et al. (2005). Their estimation is based on the short lifetime of unbound β-meteoroids, which they assume to be responsible for the observable flux. The lifetime of small α-meteoroids on bound orbits is, however, determined by the rate of destructive collisions and is much longer for optically thin discs. Given the observed amount of material and the longer lifetime, the necessary production rate and the total mass therefore decrease to the more plausible values given here.

4.3.4 Cratering Collisions

The influence of cratering collisions on the size distribution is shown in Figure 4.6 for two additional runs with increased size range, decreased mass binning (steps of a factor of 4), a decreased maximum eccentricity of 0.2, and a Q_D^* that was higher by a factor of 10. (A newer version of the ACE code was used, based on a logarithmic semi-major-axis grid instead of a linear one.) Both new runs have exactly the same initial set-up, the only difference being the modelling of collisional outcomes.

In quasi-steady state, the population of unbound and barely bound grains is nearly unaffected by cratering. In contrast, the size distribution is drastically changed at sizes 10 to 10^4 times larger than the blowout radius. Particles in this size range get efficiently eroded in collisions with smaller particles, especially with the barely bound grains. Note that, in particular, the prominent second peak at sizes of around 100 µm is completely absent when cratering is considered. This can have strong implications for thermal emission at (sub-)millimetre wavelengths, which is predominantly produced by grains in that size range.

4.4 Spatial Distribution

4.4.1 Distribution of Orbital Elements

As an example for an evolved disc, the actual distribution of the cross sectional area over the phase space of a and e is plotted in Fig. 4.7 for rocky material with an initial maximum eccentricity of 0.375 and a radial slope $\alpha = 2$. Near the inner edge (in terms of semi-major axis!) of the disc this surface area is dominated by eccentricities in the range of the parent population's, whereas in the outer region the maximum contribution comes from small grains on more eccentric orbits, because a higher eccentricity at the same semimajor axis implies an origin closer to the star, where the density of parent bodies is higher. The small α-meteoroids with sizes near the blowout limit reside on highly eccentric orbits due

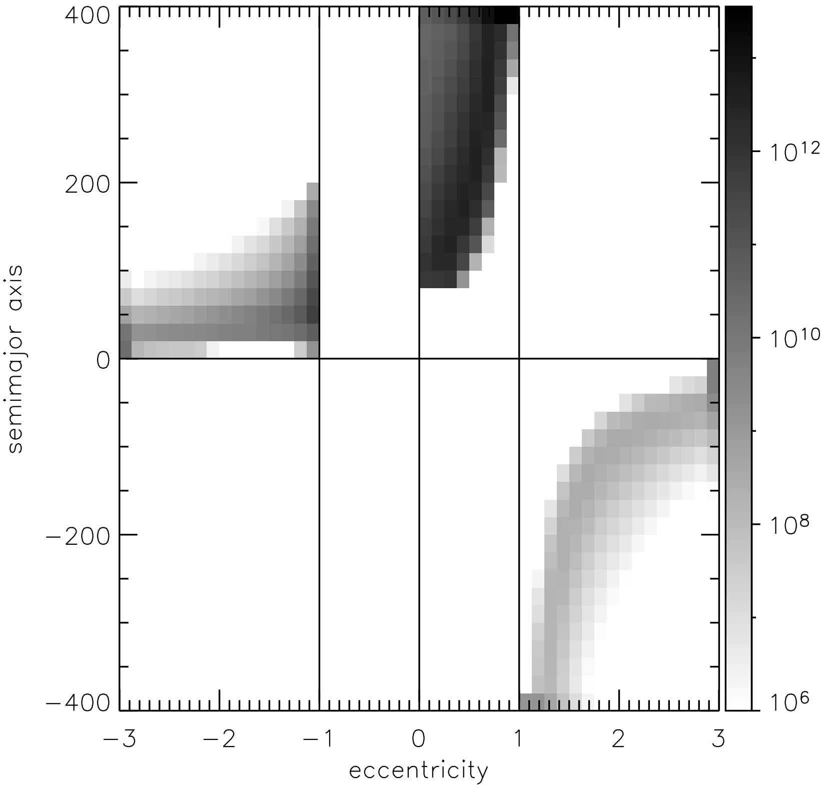

Figure 4.7: The phase space distribution for the Vega disc of Fig. 4.1 at a quasi-steady state after 10 Myr. Each bin in the *e*-*a*-grid represents the surface area (in cm^2 per phase space bin-volume) covered by the grains of all masses belonging to it.

to their being highly susceptible to radiation pressure. Thus, the fragments created near the disc's inner edge produce the major fraction of optical depth out to a considerable distance.

4.4.2 Radial Profiles

Because the semimajor axis a and the eccentricity e are used as variables, all quantities involving the radial distance r are computed by integrating the distributions over all the orbits crossing or grazing this distance (cf. Krivov et al. 2005, their Eq. 2.18).

The radial distribution of the optical thickness at the end of the integration is shown in Fig. 4.8 for four different runs, corresponding to a source ring of constant surface density with and without adjacent outer part with different slopes and assuming different eccentricity distributions. As can be seen, the average slopes of all four profiles are comparable inside and outside the ring, which is located at 80–120 AU. The average outer slope is 1.5, but the ring-only configuration drops more sharply at the edge of the ring (1.7) and flattens more at larger distances (1.2), thereby deviating more strongly from a single power law. This flattening is caused partly by the fact that the outermost semimajor axis bin is overpopulated, because it represents orbits from 380 AU to infinity. The two power-law profiles make a smoother turn-over.

The convergence of one such radial profile towards a steady state is illustrated in Fig. 4.8. This plot demonstrates the transition from a steep profile $\tau(r) \propto r^{\alpha}$ with $\alpha \lesssim -3$ to a flattened one with $\alpha \approx -1.5$. At the beginning of the simulation, the optical depth grows, reflecting overproduction of the smallest α-meteoroids. The timescale for this convergence is of the order of 10 Myr. (See Section 4.3 for the evolution of the size distribution.) Then, the optical depth starts to slowly decrease due to ongoing collisional depletion of large bodies and, therefore, decreased production of collisional fragments at dust

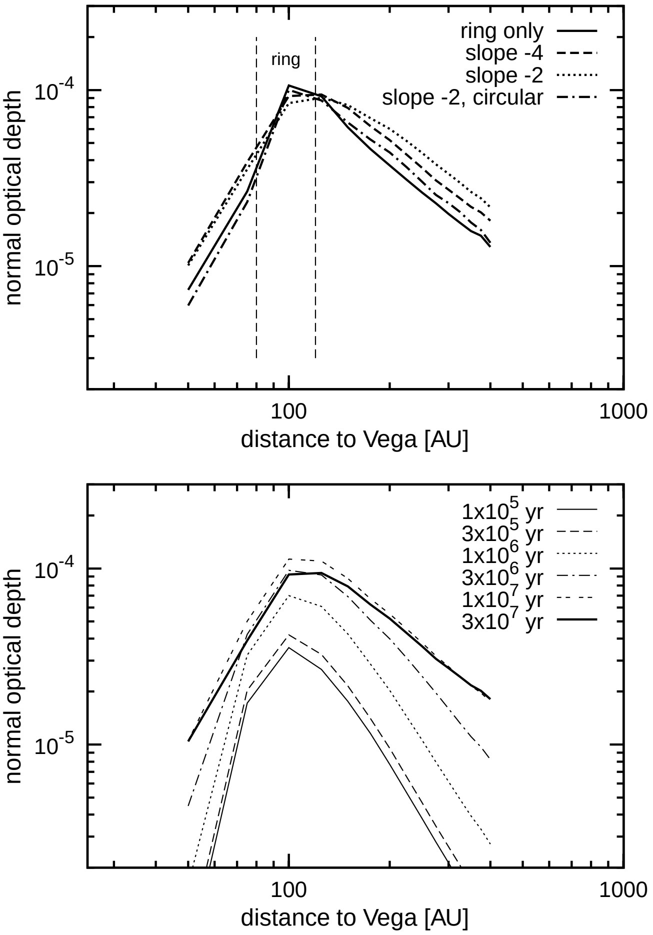

Figure 4.8: *Top:* Radial profiles of the normal optical depth after 10 Myr: one for an initially ring-like disc only (solid), one for the ring followed by the semimajor axis distribution $\propto a^{-4}$ (dashed), and two for the ring followed by the $\propto a^{-2}$ profile (dotted for a maximum eccentricity $e_{\max} = 0.375$ and dash-dotted for $e_{\max} = 0.125$). The ring boundaries at 80–120 AU are shown by vertical lines. Note that these values are the minimum and maximum semimajor axes, so that the ring in space extends somewhat inside $r = 80$ AU and outside $r = 120$ AU. *Bottom:* Convergence of the radial profile of the normal optical depth for a rocky disc with an outer slope of -4.

sizes. The rate at which this depletion occurs depends on the size of the largest objects in the disc (through those objects' collisional lifetime; see Chapter 5). In the case shown, the decay occurs at a timescale of around 100 Myr, according to the collisional lifetimes plotted in Fig. 4.4.

Figure 4.8 also shows how the radial location of the peak optical depth is slightly shifted outward due to higher rates of mass loss in the inner regions. In extension of that, and in contrast to the more ring-like configurations discussed here, Thébault & Augereau (2007) discussed discs with a larger radial extent. They report a flat profile within the disc and a drop-off with $r^{-1.5}$ beyond the outer edge. The inner, flat profile is due to the inner regions' being more rapidly depleted.

4.4.3 Surface Brightness

The resulting steady-state slopes of surface density found, between 1 and 2, have to be compared to observations. For large grains in thermal equilibrium the temperature is proportional to $r^{-1/2}$. For wavelengths much larger than the peak flux wavelength for grains of 50–100 K (60–30 µm), the emitted black-body energy is proportional to the temperature itself (in Rayleigh-Jeans approximation). In this case, the total surface brightness I of the thermal emission, which is a product of the surface density or the optical depth and the intensity in the observed spectral range, varies as $I \propto r^{\alpha-1/2}$. At wavelengths close to the maximum of the Planck function, the maximum intensity goes as the fifth power of the temperature, giving $I \propto r^{\alpha-5/2}$. However, for wavelengths shorter than the peak wavelength, i.e. for 24 µm, Wien's approximation results in an exponential temperature dependence and a steeper slope in the radial brightness profile, especially for the colder outer region beyond 100–200 AU. Therefore, a radial profile of surface brightness (in thermal emission) with indexes in a broad range between about -2 and, more probably, -4 (or even steeper) may be consistent with the model presented here, depending on the temperature distribution and the wavelength of the observations.

Su et al. (2005) report that the observed surface brightness of the (outer) Vega disk follows a power law with index $\approx -3\ldots-4$ for wavelengths of 24 and 70 µm, and ≈ -3.5 for 160 µm. But, they suggest that small particles, $\approx$ 2 µm, which sweep out through the disc with an ideal $\alpha = -1$, are responsible for the observed flux. The latter contradicts the kinetic model: the contribution of grains of 2 µm is by two orders of magnitude less than that of grains of 10 µm (Fig. 4.3).

So, the main contribution is expected to come from α-meteoroids, i.e. 10 µm and larger grains for A stars, 1 µm and larger for G stars. As mentioned above, this may be compatible with the observations, since the steeper slope of the surface density profile of bound meteoroids is compensated by a weaker dependence of surface brightness on temperature. For a more conclusive comparison to the observational data, realistic calculations of grain temperatures and thermal fluxes need to be applied to the results, this work being in progress in collaboration with S. Müller and A. V. Krivov.

[Addendum. — For scattered light (assuming isotropical scattering), the radial profile is predicted to follow $r^{\alpha-2}$, i.e. $r^{-3.5}$. Indeed, for a (marginal) majority of resolved disks, the reported slopes are in agreement with that value. Confer, e.g. , the list compiled by Thébault & Wu (2008). That list also contains prominent examples that exhibit significantly steeper slopes right at the “outer edge” of the presumed planetesimal belt (HR 4796A: 7.5, Fomalhaut: 6.1, . . .).]

Therefore, based on recent work, Thébault & Wu (2008) proposed another scenario according to which the population of dust can be split up into two regimes: (I) the unbound β-meteoroids, (II) small but bound objects whose eccentricity is set by the radiation pressure and (III) large bound objects with eccentricities set by the state of the disc’s gravito-dynamical excitation. (Wyatt (2006) introduced a similar classification, but the classes were separated with respect to whether the azimuthal distribution of grains is affected by mean-motion resonance with a planet.) The *gain* of objects of the second category is directly proportional to the rate of catastrophic collisions among objects of the third catagory, which decreases with decreasing excitation. The *loss* rate in the second category, however, depends only on the radiation-induced eccentricities (and the number of second-category objects). Thus, the equilibrium number of small α-meteoroids (and β-meteoroids even more so) is smaller in dynamically colder systems. In those cases, the emission is dominated by objects with $e \sim \beta$, i.e. objects on near-circular orbits. The overlayed extended emission from small objects on highly eccentric orbits is dimmed and the edges of the region of parent bodies are more pronounced. Thébault & Wu (2008) find a value $e \approx 0.0035$ when fitting their models to the observed radial profile of the disc around HR 4796.

There are other physical mechanisms that could affect the radial profiles. For example, the radial profile may be steepened by a mechanism that continuously removes grains from orbits with higher eccentricities, for instance a planet interior or exterior to the belt of parent bodies. A simple cut-off criterion forbidding planet crossing orbits only for parent bodies would have no impact on the results, either, but a continuous removal of small fragments on orbits of high eccentricity and short pericentric distances, which exist (Fig. 4.5, 50 AU; Fig. 4.7), could steepen the profile. Such removal can, for example, be caused by Poynting-Robertson drag – although only for rather faint discs (Wyatt 2005, e.g.,). The influence of an outer planet could be similar.

4.5 Discussion of the Vega Problem

The results of Su et al. (2005) have indicated that a significant number of small, unbound grains are required to reproduce the observed spectral energy distribution and, especially, the radial profiles of the surface brightness. Due to the short residence time within the disc, the production rate of β-meteoroids and, therefore, the total mass loss rate of the disc need to be very high ($\sim$ 5 Earth masses per Myr). The inferred high initial disc mass (0.3 to 3.0 *solar* masses) and short lifetime for such a disc are other problematic consequences (Su et al. 2005).

According to equation (4.2), the jump discontinuity in the size distribution at the blowout size can vanish – as suggested by the authors – only if the orbital timescales at which the unbound β-meteoroids leave the system are comparable to the lifetime of the gravitationally bound grains. This lifetime of small α-meteoroids is limited by mutual collisions, drag, and possibly erosive UV sputtering. However, even for icy grains, the latter mechanism is not efficient enough (Grigorieva et al. 2007b), and Poynting-Robertson drag is also negligible compared to mutual collisions (Wyatt 2005). Thus, collisions are expected to pose the strongest limitations on particle lifetime, and a rather dense disc would be required for the lifetime to be sufficiently short.

In addition, even for a disc as young and massive as that of the 12-million-year-old A5V star β Pictoris, polarimetric data seem inconsistent with a continuous distribution but suggests a break (Krivova et al. 2000).

And then, such dense discs would automatically suffer from avalanche processes that are induced by collisions between β-meteoroids and α-meteoroids (Artymowicz 1997; Krivov et al. 2000; Grigorieva et al. 2007a). As shown in the numerical runs of the collisional evolution, the moderate mass in submillimetre dust deduced from the observations of Vega's disc (Holland et al. 1998) do not imply sufficiently high densities – unless the unknown vertical *and* radial extent is by 1–2 orders of magnitude lower than assumed here.

This is the case in the "sharp-edge" scenario proposed by Thébault & Wu (2008), where the average planetesimal eccentricities (and according inclinations) might be very low: $e \approx 0.001$. This scenario, which may be connected to the observed discs around HR 4796A and Fomalhaut (α Pisces Australis), implies relative velocities of around 5 m s^{-1} at a distance of 100 AU from a main-sequence A-type star, although collision *rates* are increased. Under such conditions, collisions can disrupt only objects with critical specific energies $Q_{\mathrm{D}}^{*} \lesssim 0.5(5\ \mathrm{m\ s^{-1}})^2 \approx 13\ \mathrm{J\ kg^{-1}} = 1.3 \times 10^5\ \mathrm{erg\ g^{-1}}$, which implies material that is very weak compared to, e.g., even the lowest values Benz & Asphaug (1999) reported for ice. For objects smaller than around 1 m or larger than 1–10 km, such low velocities are insufficient for disruptive collisions even in the weakest assumed material prescriptions (Durda et al. 1998). Therefore, only cratering could slowly erode the dust population, and the effective mass loss and production of β-meteoroids would be drastically reduced.

As another consequence, even small planetesimals would still grow: estimates of the timescale for a disc to reach the state of oligarchic growth (assuming a disc between of 90 and 100 AU) give 130 to 1300 Myr for initial total disc masses of 100 and 10 Earth masses, respectively (Lissauer 1987; Goldreich et al. 2004; Kenyon et al. 2008). Although these timescales are compatible with Vega's estimated current age of around 400 Myr, they contradict to the scenario of a perturbing inner planet, which is invoked to explain the observed inner gap and potentially resonant structures (Wyatt 2003).

Other alternative scenarios can be excluded for the same reason: the erosion of small α-meteoroids by interstellar grains or by grains produced in a potential inner belt (Absil et al. 2006). In order to exhibit an observable local enhancement of β-meteoroid production, again, a more massive outer disc is required.

A single collision can also be ruled out, since even a massive planetesimal of 100–1000 km radius can produce visible amounts of dust only out to a distance of a few AU from the star (Kenyon & Bromley 2005; Wyatt 2006). The actually observed ~ 0.01 Earth masses of submillimetre dust would only be the visible tip of the much more massive fragment iceberg, requiring an improbably large sole parent body. Therefore, cold discs like that of Vega are unlikely to exhibit that kind of transience.

Finally, a phase like the Late Heavy Bombardment in the solar system has no qualitative difference to "normal" collisional grinding and, thus, requires the same unlikely high disc densities in order to sustain the production of the assumed number of blowout grains.

Hence, the size distribution in the dust ring around Vega *must* feature a break around the blowout limit, and while the exact blowout size is undetermined, a reasonable lower limit can be deduced from the assumption that the grains are compact, perfectly light-absorbing (i.e. $Q_{\mathrm{pr}} = 1$) spheres with a bulk density of 3.5 g cm^{-3}. For Vega's luminosity and mass, as inferred from the pole-on view ($L = 58L_{\odot}$, $M = 2.75M_{\odot}$), equation (2.35) gives a blowout size ($\beta = 0.5$) of 7 µm. Taking into account a reduced mass and equatorial luminosity ($M = 2.3M_{\odot}$, $L \approx 30L_{\odot}$), the result is 4.3 µm. Still, this value is well above the 1–2 µm lower limit that Su et al. (2005) derived in their best fit. Thus, a continuous size distribution with grains from 1 to 50 µm replenished in a collisional cascades seems physically unjustified.

But do we need micrometre-sized grains? Or do we just need grains that emit *like* micrometre-sized grains? Such grains could be 10 µm in size with surface structure on a sizescale of one micron. They would have the absorption and radiation pressure efficiency of a blank 10-µm grain but a higher surface temperature due to a reduced emission efficiency at mid- and far-infrared wavelengths. This higher temperature would result in a relative increase in flux at 24 µm compared to 70 µm. A low thermal conductivity would increase this effect. What is more, such grains would still be gravitationally bound to Vega and, therefore, sufficiently long-lived and abundant, in contrast to merely porous grains of 10 µm. The existence of structured grains is obvious, but no sytematic studies have been undertaken concerning the influence on *absolute* emission/absorption efficiency and temperature.

So, no definite positive answer can be provided for the problem with the Vega system's infrared excess at 24 µm, but the assumption of unbound grains in abundance can be rejected with high certainty.

5 Long-Term Evolution

5.1 Introduction: Observational Statistics and Models

All authors point out a decay of the observed infrared excesses with system age. However, the values reported for the slope of the decay, assuming a power-law dependence $t^{-\alpha}$, span a wide range. Greaves & Wyatt (2003) suggest $\alpha \lesssim 0.5$, Liu et al. (2004) give $0.5 < \alpha < 1.0$, Spangler et al. (2001) report $\alpha \approx 1.8$, and Greaves (2005) and Moór et al. (2006) derive $\alpha \approx 1.0$. Fits of the upper envelope of the distribution of luminosities over the age yield $\alpha \approx 1.0$ as well (Rieke et al. 2005), which is in broad agreement with the recent review of Spitzer detections at 70 µm presented by Hillenbrand et al. (2008). Trilling et al. (2008) found a rather shallow slope to best fit their 24- and 70-µm Spitzer data of 200 FGK stars, focussing on systems older than 1 Gyr. Besides, the dust fractional luminosity exhibits a large dispersion at any given age.

In an attempt to gain theoretical understanding of the observed evolution, Dominik & Decin (2003) assumed that equally-sized "comets" produce dust through a cascade of subsequent collisions among ever-smaller objects. If this dust is removed by the same mechanism, the steady-state amount of dust in such a system is proportional to the number of comets. This results in an $M/M_0 \approx T/t$ dependence for the amount of dust and for the number of comets or the total mass of the disc. Under the assumption of a steady state, this result is valid even for more complex systems with continuous size distributions from planetesimals to dust. Material in tenuous discs, where the lifetime of dust grains is not limited by collisions but by transport processes like the Poynting-Robertson drag (Artymowicz 1997; Krivov et al. 2000; Wyatt 2005), follows $M \propto t^{-2}$ rather than $M \propto t^{-1}$.

More recently, Wyatt et al. (2007a) lifted the most severe simplifying assumption of the Dominik-Decin model, that of equal-sized parent bodies, and included them into the collisional cascade. A debris disc they consider is no longer a two-component system "comets + dust". Instead, it is a population of solids with a continuous size distribution, from planetesimals down to dust. A key parameter of the description by Dominik & Decin (2003) is the collisional lifetime of comets, T. Wyatt et al. (2007a) replaced it with the lifetime of the largest planetesimals and worked out the dependencies on this parameter in great detail. Since the collisional timescale is inversely proportional to the amount of material, $T \propto 1/M_0$, the asymptotic disc mass becomes independent of its initial mass. Only dynamical quantities, i.e. the disc's radial position and extent, the orbiting objects' eccentricities and inclinations, and material properties, i.e. the critical specific energy and the disruption threshold, as well as the type of the central star determine the very-long-term evolution.

Still, there are two important simplifications made in the model by Wyatt et al. (2007a): (i) the disc is assumed to be in collisional equilibrium at all sizes, from dust up to the largest planetesimals and (ii) the minimum specific energy needed to disrupt colliding objects is independent of their size. As a consequence of (i) and (ii), the size distribution of solids is a single power-law. To check how reasonable these assumptions are, realistic simulations of the discs with collisional codes are necessary (e.g., Thébault et al. 2003; Krivov et al. 2005, 2006; Thébault & Augereau 2007).

Aiming at finding characteristic parameters for the long-term evolution of debris discs around (G2-type) stars, this chapter presents results from numerical runs with the ACE code and a newly developed analytic model. The results are then compared and shown to be compatible with observational data from Spitzer. (This chapter is based on work done for "Löhne et al. (2008)", but it is updated and complemented in some places.)

Table 5.1: Description of numerical runs.

Run	Distance [AU]	$e_{\max}$
Nominal runs		
ii-0.3	7.5–15	0.3
i-0.3	15–30	0.3
o-0.3	30–60	0.3
oo-0.3	60–120	0.3
Additional runs		
i-0.1	15–30	0.1
i-0.2	15–30	0.2
i-0.4	15–30	0.4

5.2 Description of Numerical Runs

5.2.1 Commons for All Runs

All disc models presented here are set up around a star of solar mass and luminosity. Parameters of the central star affect the disc evolution in various ways. They determine the size limit for grain blowout by radiation pressure and orbital velocities at a given distance, thereby altering impact velocities and rates. For late-type stars, strong stellar winds may affect the dust dynamics (Augereau & Beust 2006; Strubbe & Chiang 2006). On the observational side, dust temperatures and brightnesses are influenced. Here, the focus is on the scalings for a fixed spectral type (G2V), and not on scalings between different types.

The discs themselves all share the same material properties and shapes. The material is adopted as described by a bulk density $\rho = 2.5$ g cm^{-3}, the Mie-calculated radiation pressure efficiency of astronomical silicate (Bohren & Huffman 1983; Laor & Draine 1993), and a critical fragmentation energy as specified in Sect. 2.2.1. The Poynting-Robertson effect was switched off, since it is unimportant for the debris discs under study, as well as stellar wind drag, which plays only a minor role around G-type stars. The fragments produced in an individual collision are distributed according to a single power law, $\mathrm{d}N \propto s^{-3.5}\mathrm{d}s \propto m^{-11/6}\mathrm{d}m$. The biggest fragment size is assumed to scale with specific impact energy to the power of 1.24 (for details, see Krivov et al. 2006). The initial mass distribution is given by $\mathrm{d}N \propto m^{-q}$, with $q = 1.87$, a value that accounts for the modification of Dohnanyi's (1969) classical $q = 1.833$ through the size dependence of material strength (see, e.g., Sect. 5.4.7 or Durda & Dermott 1997). The particle masses range from 4.2×10^{-15} g, corresponding to a radius of 74 nm, to 4.2×10^{21} g, corresponding to 74 km. The stepping between the 60 mass bins is logarithmic with a factor of ≈ 4 between neighbouring bins. The initial radial profile of the particle density was given by a slope of the normal optical depth of -1.0. The initial total mass of each disc was set to 1 $M_{\oplus}$ (Earth mass).

5.2.2 Specifics of Individual Runs

Four "nominal" runs have been made, each of which corresponds to a certain radial part of the disc between 7.5 and 120 AU from the star (Table 5.1). In these runs, initial eccentricities of planetesimals were assumed to be uniformly distributed between $e_{\min} = 0.0$ and $e_{\max} = 0.3$, spanning three bins centred at 0.05, 0.15 and 0.25. In addition, three runs with altered maximum eccentricity of 0.1, 0.2, and 0.4 were made for the 15–30 AU ring. In all the runs, the orbital inclinations were set to $I = e/2$.

5.3 Numerical Results and Scaling Laws

5.3.1 Evolution of Discs of Different Masses

In this subsection, analytical laws are derived for the scaling of collision timescales with disc masses. The results of the numerical runs are shown not to be consistent with a steady state for a typical disc as a whole.

As long as objects are both created and lost *only* in two-particle collisions, their gain and loss rates are given by

$$\begin{aligned}\frac{\mathrm{d}}{\mathrm{d}t}\left[n(\mathbf{p},s,t)\right] &= \iiiint \left[G(\mathbf{p},s,\mathbf{p}_1,s_1,\mathbf{p}_2,s_2)\right.\\ &\quad \left.-L(\mathbf{p}_1,s_1,\mathbf{p}_2,s_2)\delta(\mathbf{p}-\mathbf{p}_1)\delta(s-s_1)\right]\\ &\times\ \tilde{n}(\mathbf{p}_1,s_1,t)\,\tilde{n}(\mathbf{p}_2,s_2,t)\\ &\times\ \mathrm{d}\mathbf{p}_1\mathrm{d}s_1\mathrm{d}\mathbf{p}_2\mathrm{d}s_2, \qquad (5.1)\end{aligned}$$

where the function $G(\mathbf{p},s,\mathbf{p}_1,s_1,\mathbf{p}_2,s_2)$ describes the gain in population $(\mathbf{p},\mathbf{s})$ due to collisions between $(\mathbf{p}_1,s_1)$ and $(\mathbf{p}_2,s_2)$ and the function $L(\mathbf{p}_1,s_1,\mathbf{p}_2,s_2)$ accounts for the loss in population $(\mathbf{p}_1,s_1)$ in collisions with $(\mathbf{p}_2,s_2)$.

A direct consequence of equation (5.1) is the invariance under the transformation

$$(n(\mathbf{p},s,t),t)\longmapsto\left(\frac{n'(\mathbf{p},s,t')}{x},t'x\right) \qquad (5.2)$$

with $x=\text{const}$:

$$\begin{aligned}\frac{\mathrm{d}}{\mathrm{d}(xt')}\left[\frac{n'(\mathbf{p},s,t')}{x}\right] &= \iiiint \left[G(\mathbf{p},s,\mathbf{p}_1,s_1,\mathbf{p}_2,s_2)\right.\\ &\quad \left.-L(\mathbf{p}_1,s_1,\mathbf{p}_2,s_2)\delta(\mathbf{p}-\mathbf{p}_1)\delta(s-s_1)\right]\\ &\times\ n'(\mathbf{p}_1,s_1,t')x^{-1}\,n'(\mathbf{p}_2,s_2,t')x^{-1}\\ &\times\ \mathrm{d}\mathbf{p}_1\mathrm{d}s_1\mathrm{d}\mathbf{p}_2\mathrm{d}s_2\\ &= \frac{\mathrm{d}}{\mathrm{d}t'}\left[n'(\mathbf{p},s,t')\right]. \qquad (5.3)\end{aligned}$$

From the definition of the total disc mass,

$$M_{\mathrm{disc}}(t)\equiv\iint n(\mathbf{p},s,t)\mathrm{d}\mathbf{p}\mathrm{d}s, \qquad (5.4)$$

one can easily conclude that the transformation

$$(M(t),t)\longmapsto\left(\frac{M'(t')}{x},t'x\right) \qquad (5.5)$$

is also invariant. Therefore, the mass scale of a system under collisional evolution is inversely proportional to its timescale. For example, doubling the initial total mass halves the collisional lifetime of the system ("$x=0.5$"). All curves in the $M_{\mathrm{disc}}(t)$ plots can be shifted along lines of equal $t\cdot M_{\mathrm{disc}}$.

A debris disc is said to be in a quasi-steady state or quasi-equilibrium if the amounts of particles with different sizes on different orbits, while changing with time (therefore "quasi"), stay constant relative to each other. (For brevity, "quasi" will often be omitted and simply "steady state" or "equilibrium" used.) Hence, the assumption of a quasi-steady state can now be expressed as

$$n(\mathbf{p},s,t)=\tilde{n}(\mathbf{p},s)\,f(t). \qquad (5.6)$$

The total disc mass,

$$M_{\rm disc}(t) = \iint n(\mathbf{p},s,t)\mathrm{d}\mathbf{p}\mathrm{d}s, \tag{5.7}$$

can be rewritten as

$$M_{\rm disc}(t) = f(t)\iint \tilde{n}(\mathbf{p},s)\mathrm{d}\mathbf{p}\mathrm{d}s \tag{5.8}$$

or, setting $f(0) = 1$,

$$M_{\rm disc}(t) = f(t)M_0, \tag{5.9}$$

where M_0 is the initial disc mass.

The disc mass changes at a rate

$$\dot{M}_{\rm disc}(t) = \iint \dot{n}(\mathbf{p},s,t)\mathrm{d}\mathbf{p}\mathrm{d}s \tag{5.10}$$

or

$$\dot{M}_{\rm disc}(t) = \dot{f}(t)\iint \tilde{n}(\mathbf{p},s)\mathrm{d}\mathbf{p}\mathrm{d}s. \tag{5.11}$$

From equations (5.1) and (5.10), one finds that $\dot{M}_{\rm disc}(t) \propto f^2(t)$, while equation (5.11) suggests $\dot{M}_{\rm disc}(t) \propto \dot{f}(t)$. Hence, $\dot{f}(t) \propto f^2(t)$. Integration yields

$$f = \frac{1}{1+t/T}. \tag{5.12}$$

Using equation (5.9), one obtains

$$M_{\rm disc}(t) = \frac{M_0}{1+t/T} \tag{5.13}$$

and

$$\dot{M}_{\rm disc}(t) = -CM_{\rm disc}^2, \tag{5.14}$$

where $1/C = M_0 \cdot T$, i.e. the product of the initial mass and a characteristic time.

Dominik & Decin (2003) used this approach and equated the characteristic time T with the collisional lifetime of their “comets”. At the initial phase $t \ll T$, equation (5.13) gives

$$M_{\rm disc}(t) \approx M_0\left(1 - t/T\right). \tag{5.15}$$

If the system is old enough so that $t \gg T$, the total mass will be just proportional to t^{-1}. Particles whose lifetimes are independent of the total mass are exempt from the asymptotic one-over-t behavior. Examples would be the β-meteoroids that are blown out and small particles in discs tenuous enough for the Poynting-Robertson effect to be more efficient than collisions. The total mass of such particles is $\propto t^{-2}$ (Dominik & Decin 2003).

As shown above, for the systems that undergo a steady-state collisional evolution, the factor C in equation (5.14) (or T) should be constant. To check this, $C = -\dot{M}_{\rm disc}/M_{\rm disc}^2$ was evaluated for every two subsequent time steps of the numerical runs. The results are given in Fig. 5.1.

Instead of being constant at later times, C decreases, roughly following a power law $C \propto t^{-2/3\ldots-4/5}$. The explanation is simple: the systems did not reach an equilibrium where $t \gg T$ or at least $t \approx T$ during their lifetime. The evolution of the total mass in Fig. 5.2 demonstrates that as well.

5.3.2 Dependence on Distance from the Star

Rings of identical mass but at different distances have different collisional timescales. The comparison in Fig. 5.1 shows that doubling the distance requires a 20-fold increase in disc mass to have the same timescale. This corresponds to a power-law dependence

$$C \propto r^{-4.3}. \tag{5.16}$$

Figure 5.1: The coefficient C from equation (5.14) as a function of time for four nominal runs. The total disc mass and time in the runs are scaled according to $M_{\rm disc} \propto t^{-1}$ to compensate for the difference in dynamical timescale. Note that the near-constancy of C at the beginning of the evolution is an artefact of the double-logarithmic plotting. The double-linear inset shows that the decrease of C is fastest at earlier times.

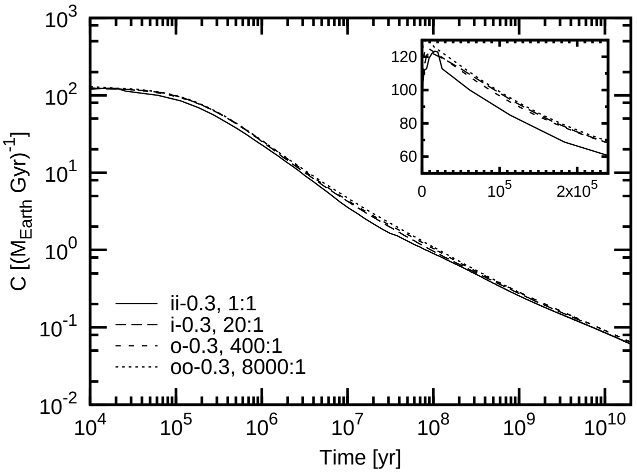

Figure 5.2: The evolution of the total mass in the four nominal runs. Again, the plateau at the beginning of the evolution is an artefact of the logarithmic plotting of time. In fact, the mass decay is strongest at the very beginning (see inset and Eqs. 5.13, 5.15).

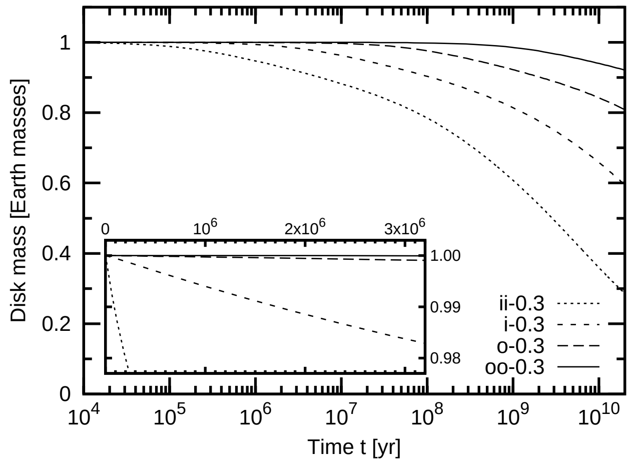

In a thorough analytic approach based on a Dohnanyi-type collisional cascade, Wyatt et al. (2007a) came up with $C \propto r^{-13/3}$, which is in good agreement with our numerical result. This index is made up of three contributions. First, the density in the rings drops with r^{-3} as their circumference, height, and width increase linearly. Second, the relative velocities have an $r^{-1/2}$ dependence. Third, these impact velocities affect the minimum required mass for a projectile to be disruptive and thereby the total number of such projectiles. That gives another r^{1-q}, where q is the slope in the appropriate mass distribution, e.g., $q = 11/6$ for the classical Dohnanyi case. See Sect. 5.4.2 for details.

5.3.3 Dependence on Eccentricities of Parent Bodies

The intrinsic collisional probability of planetesimals is nearly independent of their eccentricities, as long as they are not too high (see, e.g. Krivov et al. 2006). Nevertheless, eccentricities determine impact velocities and, through that, the minimum size of a disruptive projectile. Therefore, higher planetesimal eccentricities imply a larger rate of catastrophic collisions and thus a faster collisional evolution. To quantify the dependence, runs have been made with maximum eccentricities of 0.1, 0.2, 0.3, and 0.4 (Table 5.1) and the values of C determined. The results suggest a power law $C \propto e_{\rm max}^{9/4}$ as shown in Fig. 5.3.

This result comes as a slight surprise. Wyatt et al. (2007a) derive $C \propto e^{5/3}$. A similar scaling is inherited by our analytic model and leads to $C \propto e^{1.75}$, see equation (5.37) below. However, the particle-in-a-box assumptions used are valid only locally. The globally integrated combination of collision rates and velocities behaves differently, as show the numerical results.

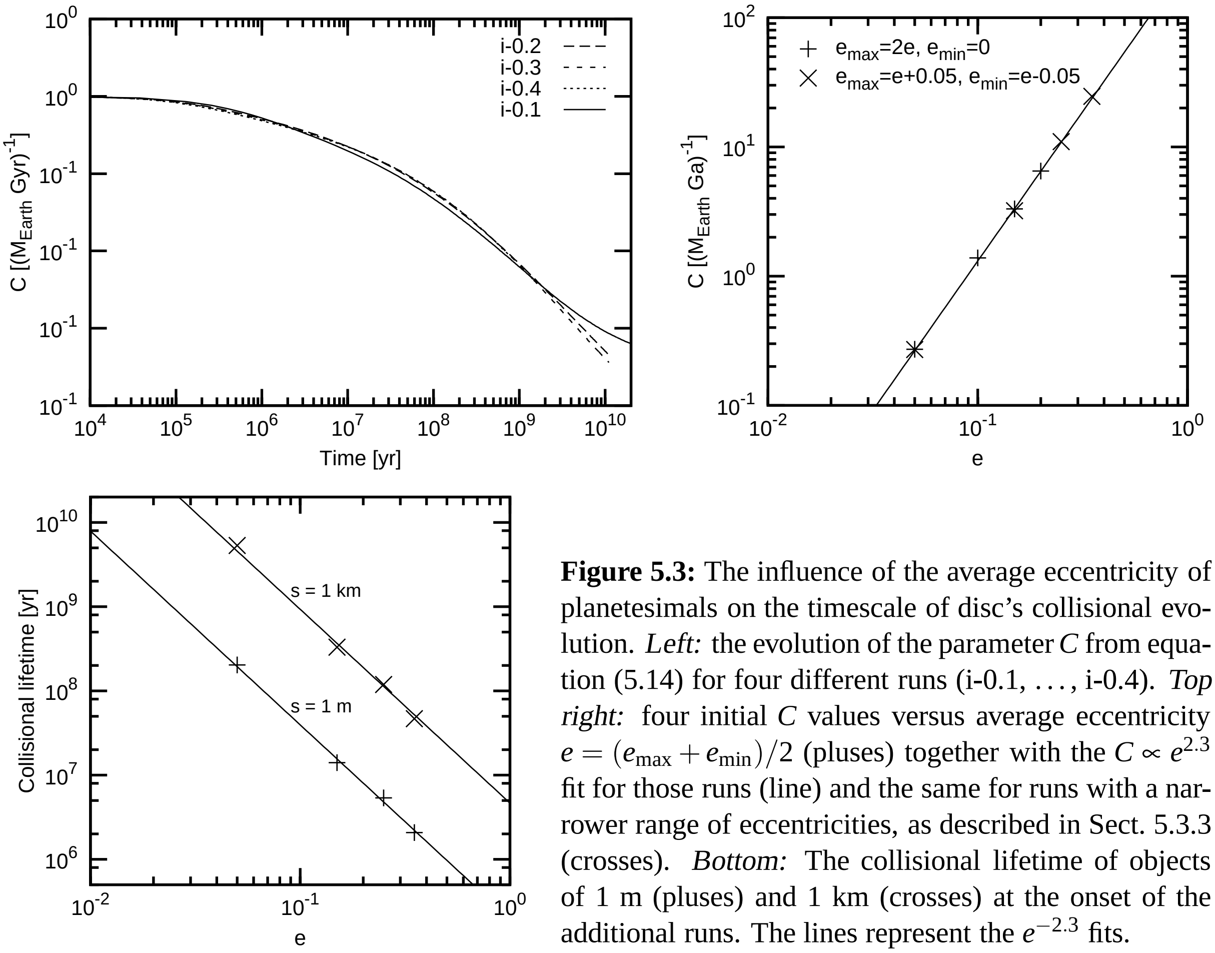

Figure 5.3: The influence of the average eccentricity of planetesimals on the timescale of disc's collisional evolution. *Left:* the evolution of the parameter C from equation (5.14) for four different runs (i-0.1, ..., i-0.4). *Top right:* four initial C values versus average eccentricity $e = (e_{\max} + e_{\min})/2$ (pluses) together with the $C \propto e^{2.3}$ fit for those runs (line) and the same for runs with a narrower range of eccentricities, as described in Sect. 5.3.3 (crosses). *Bottom:* The collisional lifetime of objects of 1 m (pluses) and 1 km (crosses) at the onset of the additional runs. The lines represent the $e^{-2.3}$ fits.

5.4 Analytic Model for Evolution of Disc Mass and Dust Mass

5.4.1 Three-Slope Distribution

The combination of material strength at smaller sizes and self-gravity at larger ones, with a turnover at around 100 m, causes the size distribution in a collisionally evolving system to strongly deviate from a single-slope power law, especially for object sizes of around 1 km. This is illustrated by Fig. 5.4, that shows how a disc evolves from the first-guess power law to a more realistic size distribution. The speed of this evolution is determined by the collisional timescales of populations of different-sized particles in the disc. Populations of smaller particles with sufficiently short lifetimes consist mostly of fragments of disruption of larger bodies. They will have reached collisional equilibrium with each other soon, according to their production rate by populations with longer lifetimes. Those latter populations of bigger particles will still be on their way to a steady state. As time goes by, more and more long-lived populations will undergo the transition from primordial to reprocessed material.

As this transitional mass moves towards larger objects with time, the smaller particles follow to a new "intermediate steady state". The lower panel of Fig. 5.4 shows the development of the characteristic wavy shape in the size distribution at the small-size end near the blowout limit due to radiation pressure. (See section 4.3) for details. Once established, this shape remains constant. Only the absolute level changes because this distribution at smaller sizes acts as the trail of the distribution at larger sizes. In the upper panel of Fig. 5.4, the number of smaller particles is constant for some time and then goes down, as soon as the distribution in the gravity regime starts to deviate from its primordial one.

These arguments suggest that an overall size distribution $n(s)$ can be approximated by a combination of three power laws (Fig. 5.5). For particles large enough to be only barely affected by collisions at time t, n shall be assumed to follow s^{-p_p}. Here, $p_\mathrm{p} = 2 - 3q_\mathrm{p}$ is the "primordial" slope determined by

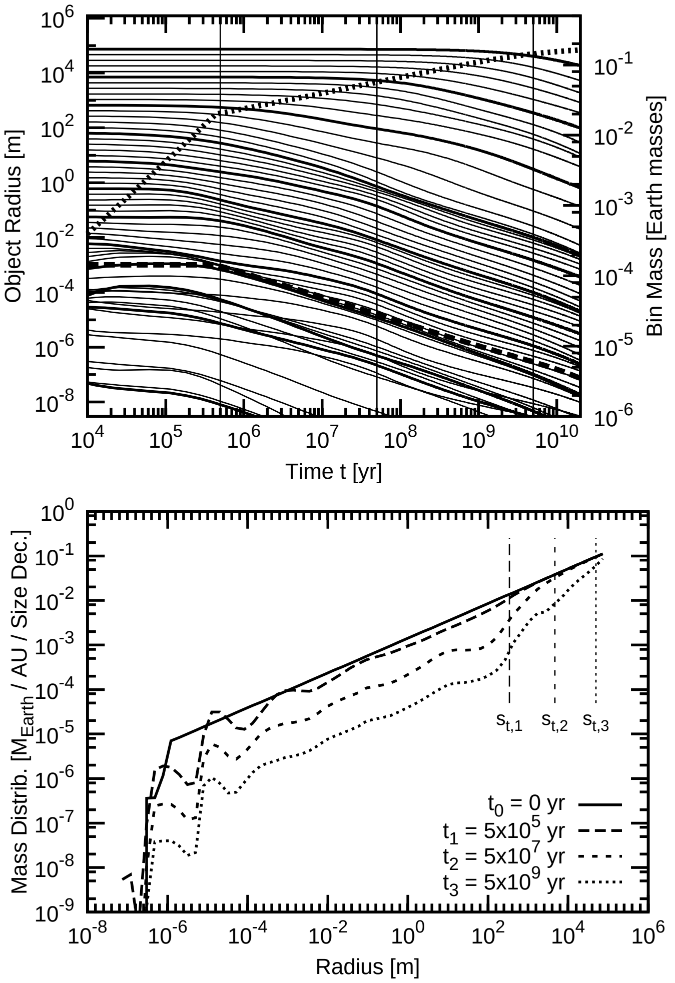

Figure 5.4: Results of the ii-0.3 run. *Top*: Time evolution of mass in individual mass bins, from the largest bodies of 74 km in radius to the smallest, 74 nm in radius. The mass ratio between adjacent bins is 4. Each solid line corresponds to one individual bin and gives the mass contained in that bin (see the right axis) as a function of time. The left axis can be used to find the line that corresponds to a given object size. The thick dashed curve corresponds to ≈ 1 mm radius, i.e. to the largest solids still treated as dust. The thick dotted curve, which goes roughly through the turning points of the curves, is the transition size $s_t(t)$; see equation (5.38). *Bottom*: Size/mass distribution at four specific instants of time shown in the top panel with vertical lines: initially, after 5×10^5 years when s_t has reached s_b, and after 5×10^7 and 5×10^9 yr when significant dust depletion has already occurred.

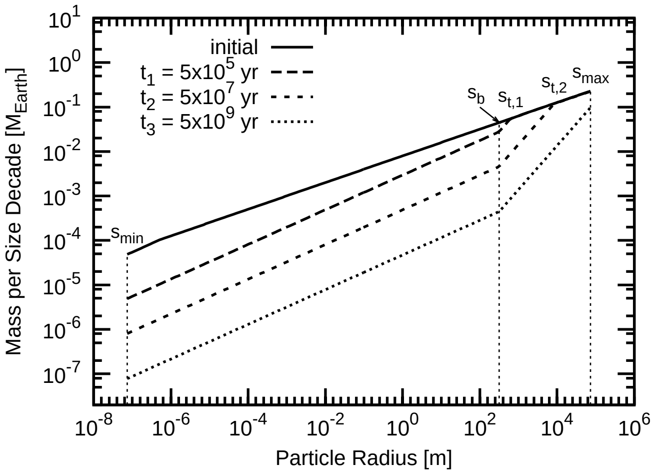

Figure 5.5: Schematic plot of the three regimes in the mass distribution and its time evolution. The mass s_t divides second generation material in collisional equilibrium ($s < s_t$) from primordial material ($s > s_t$), while s_b divides the material strength regime ($s < s_b$) from the gravity regime ($s > s_b$).

the processes in which these planetesimals have formed. Small particles that are in quasi-steady state are separated from bigger primordial objects by a transition zone, characterized by a time-dependent size $s_t(t)$. To distinguish between the strength and gravity regimes, two more power laws are introduced and the mass distribution is assumed to follow $n \propto s^{2-3q_g}$ for gravity-dominated quasi-steady state and $n \propto s^{2-3q_s}$ for strength-dominated quasi-steady state. The two regimes are separated by an object size s_b, which will be called breaking radius, hereinafter. Thus, the waviness is neglected, but the effect of a size-dependent Q_D^* is kept.

The resulting size distribution is given by

$$n(s) = n_{\mathrm{max}} \left(\frac{s_{\mathrm{max}}}{s} \right)^{3q_{\mathrm{p}}-2} \tag{5.17}$$

for $s_{\mathrm{t}} \leq s < s_{\mathrm{max}}$,

$$n(s) = n_{\mathrm{max}} \left(\frac{s_{\mathrm{max}}}{s_{\mathrm{t}}} \right)^{3q_{\mathrm{p}}-2} \left(\frac{s_{\mathrm{t}}}{s} \right)^{3q_{\mathrm{g}}-2} \tag{5.18}$$

for $s_{\mathrm{b}} \leq s < s_{\mathrm{t}}$, and

$$n(s) = n_{\mathrm{max}} \left(\frac{s_{\mathrm{max}}}{s_{\mathrm{t}}} \right)^{3q_{\mathrm{p}}-2} \left(\frac{s_{\mathrm{t}}}{s_{\mathrm{b}}} \right)^{3q_{\mathrm{g}}-2} \left(\frac{s_{\mathrm{b}}}{s} \right)^{3q_{\mathrm{s}}-2} \tag{5.19}$$

for $s_{\mathrm{min}} < s < s_{\mathrm{b}}$, where $n_{\mathrm{max}} \equiv n(s_{\mathrm{max}})$, with s_{max} being the size of the largest planetesimals. From this distribution, two important quantities can be derived. One is the total *disc* mass,

$$M_{\mathrm{disc}} = \int_{s_{\mathrm{min}}}^{s_{\mathrm{max}}} n(s) \frac{4}{3} \pi \rho s^3 \mathrm{d}s, \tag{5.20}$$

and the other is *dust* mass (that determines the infrared luminosity and, therefore, provides a link to observations),

$$M_{\mathrm{dust}} = \int_{s_{\mathrm{min}}}^{s_{\mathrm{d}}} n(s) \frac{4}{3} \pi \rho s^3 \mathrm{d}s, \tag{5.21}$$

where $s_{\mathrm{min}} \leq s_{\mathrm{d}} < s_{\mathrm{b}}$.

5.4.2 Collisional Lifetimes of Planetesimals

As seen from equations (5.17)–(5.21), the evolution of M_{disc} and M_{dust} is controlled by $n_{\mathrm{max}}(t)$ and $s_{\mathrm{t}}(t)$.

We start with n_{max} and assume, according to equations (5.6) and (5.12):

$$n_{\mathrm{max}}(t) = \frac{n_{\mathrm{max}}(0)}{1 + t/T_{\mathrm{max}}}, \tag{5.22}$$

where T_{max} is the collisional lifetime of these largest bodies. Equation (5.22) closely reproduces the disc evolution as soon as the whole system has reached the quasi-steady state at all sizes or, in other words, as soon as $s_{\mathrm{t}}(t)$ has reached s_{max}.

The second quantity needed, $s_{\mathrm{t}}(t)$, could easily be obtained by inverting the function $T(s)$, the collisional lifetime of planetesimals of a given size s. To obtain $T(s)$, we begin with the lifetime of the largest objects in a disc. Assuming that $q > 5/3$, Wyatt et al. (2007a, their Eq. 12) approximated it as

$$T_{\mathrm{max}} = \frac{4\pi}{\sigma_{\mathrm{tot}}} \cdot \left(\frac{s_{\mathrm{max}}}{s_{\mathrm{min}}} \right)^{3q_{\mathrm{p}}-5} \cdot \frac{r^{5/2} \mathrm{d}r}{(\mathrm{G}M_*)^{1/2}} \frac{I}{f(e,I) G(q,s)}. \tag{5.23}$$

where e and I are the effective orbital eccentricities and inclinations, σ_{tot} is the initial cross sectional area of the disc material, G the gravitational constant, r the radial distance of the ring of parent bodies, and $\mathrm{d}r$ its width. The slope q in their single-power-law approach corresponds to the primordial slope q_{p} in our nomenclature. The functions f and G are given, respectively, by

$$f(e,I) = \sqrt{\frac{5}{4} e^2 + I^2} \tag{5.24}$$

and

$$\begin{aligned} G(q,s) &= \left[X_\mathrm{c}(s)^{5-3q} - \left(\frac{s_\mathrm{max}}{s}\right)^{5-3q}\right] \\ &+ 2\frac{q-5/3}{q-4/3}\left[X_\mathrm{c}(s)^{4-3q} - \left(\frac{s_\mathrm{max}}{s}\right)^{4-3q}\right] \\ &+ \frac{q-5/3}{q-1}\left[X_\mathrm{c}(s)^{3-3q} - \left(\frac{s_\mathrm{max}}{s}\right)^{3-3q}\right], \end{aligned} \tag{5.25}$$

with

$$X_\mathrm{c}(s) = \left(\frac{2Q_\mathrm{D}^*(s)\,r f(e,I)^{-2}}{\mathrm{G}M_*}\right)^{1/3}. \tag{5.26}$$

While $f(e,I)$ describes the dependence of the impact velocities on eccentricities and inclinations, the functions G and X_c characterize the disruption of planetesimals by smaller projectiles. Namely, $X_\mathrm{c}(s)$ is minimum size ratio between the *smallest* disruptive projectile and the target, and $G(q,s)$ is the number of disruptive projectiles.

We need the lifetime of objects of an arbitrary size, $T(s < s_\mathrm{max})$. To derive it, we can simply substitute s_max by s in equation (5.23), obtaining

$$T(s) = \frac{4\pi}{\sigma_\mathrm{tot}} \cdot \left(\frac{s}{s_\mathrm{min}}\right)^{3q_\mathrm{p}-5} \cdot \frac{r^{5/2}\mathrm{d}r}{(\mathrm{G}M_*)^{1/2}} \frac{I}{fG(q_\mathrm{p},s)}. \tag{5.27}$$

In order to replace the dependence on the initial cross sectional area of objects, σ_tot, with their initial total mass, M_0, we need to derive both quantities from the initial size distribution in equation (5.17). The area is given by

$$\sigma_\mathrm{tot} = n_\mathrm{max}(0) \cdot \frac{\pi s_\mathrm{max}^3}{3q_\mathrm{p}-5}\left[\left(\frac{s_\mathrm{max}}{s_\mathrm{min}}\right)^{3q_\mathrm{p}-5} - 1\right]. \tag{5.28}$$

Since it is dominated by s_min for $q_\mathrm{p} > 5/3$, we obtain

$$\sigma_\mathrm{tot} = n_\mathrm{max}(0) \cdot \frac{\pi s_\mathrm{max}^3}{3q_\mathrm{p}-5}\left(\frac{s_\mathrm{max}}{s_\mathrm{min}}\right)^{3q_\mathrm{p}-5}. \tag{5.29}$$

The initial total disc mass is

$$M_0 = n_\mathrm{max}(0) \cdot \frac{4\pi\rho s_\mathrm{max}^4}{3(6-3q_\mathrm{p})}\left[1 - \left(\frac{s_\mathrm{min}}{s_\mathrm{max}}\right)^{6-3q_\mathrm{p}}\right]. \tag{5.30}$$

For $q_\mathrm{p} < 2$, it is dominated by s_max. However, since a primordial slope $q_\mathrm{p} \geq 2$ is not unrealistic (see Sect. 5.4.8) no further approximation is used. Then, the area and the mass are related through

$$\sigma_\mathrm{tot} = M_0 \cdot \frac{3(2-q_\mathrm{p})}{4(q_\mathrm{p}-5/3)} \cdot s_\mathrm{max}^{-1} \cdot \left(\frac{s_\mathrm{max}}{s_\mathrm{min}}\right)^{3q_\mathrm{p}-5}\left[1 - \left(\frac{s_\mathrm{min}}{s_\mathrm{max}}\right)^{6-3q_\mathrm{p}}\right]^{-1}. \tag{5.31}$$

Inserting equation (5.31) into equation (5.27) results in

$$\begin{aligned} T(s) &= \frac{16\pi\rho}{3M_0} \cdot \left(\frac{s}{s_\mathrm{max}}\right)^{3q_\mathrm{p}-5} \frac{s_\mathrm{max} r^{5/2}\mathrm{d}r}{(\mathrm{G}M_*)^{1/2}} \\ &\times \frac{q_\mathrm{p}-5/3}{2-q_\mathrm{p}}\left[1 - \left(\frac{s_\mathrm{min}}{s_\mathrm{max}}\right)^{6-3q_\mathrm{p}}\right] \frac{I}{f(e,I)G(q_\mathrm{p},s)}, \end{aligned} \tag{5.32}$$

which gives the collisional lifetime of an object with radius s. Note that

$$\frac{1}{2-q_\mathrm{p}}\left[1-\left(\frac{s_\mathrm{min}}{s_\mathrm{max}}\right)^{6-3q_\mathrm{p}}\right] \longrightarrow 3\ \ln\frac{s_\mathrm{max}}{s_\mathrm{min}} \tag{5.33}$$

for $q_\mathrm{p} \rightarrow 2$.

If the mean impact velocities in the system are high enough to allow planetesimals of radius s to get disrupted in a collision, i.e. $X_\mathrm{c}(s) \ll s_\mathrm{max}/s$, $G(q_\mathrm{p},s)$ reduces to

$$G(q_\mathrm{p},s) \approx \frac{q_\mathrm{p}-5/3}{q_\mathrm{p}-1}\cdot X_\mathrm{c}(s)^{3-3q_\mathrm{p}}, \tag{5.34}$$

and $T(s)$ to

$$\begin{aligned} T(s) &= \frac{16\pi\rho}{3M_0}\cdot\left(\frac{s}{s_\mathrm{max}}\right)^{3q_\mathrm{p}-5}\cdot r^2\mathrm{d}r\cdot\left(\frac{r}{\mathrm{G}M_*}\right)^{q_\mathrm{p}-1/2} \\ &\times \frac{q_\mathrm{p}-1}{2-q_\mathrm{p}}\left[1-\left(\frac{s_\mathrm{min}}{s_\mathrm{max}}\right)^{6-3q_\mathrm{p}}\right](2Q_\mathrm{D}^*)^{q_\mathrm{p}-1}\,\frac{I}{f(e,I)^{2q_\mathrm{p}-1}} \end{aligned} \tag{5.35}$$

Now, we take into account the dependence of Q_D^* on the object size s, as was done by O'Brien & Greenberg (2003). If we are only interested in the gravity regime, $s > s_\mathrm{b}$, equation (2.27) is simplified to

$$Q_\mathrm{D}^*(s) \approx Q_\mathrm{D,b}^*\cdot\left(\frac{s}{s_\mathrm{b}}\right)^{3b_\mathrm{g}}, \tag{5.36}$$

where $Q_\mathrm{D,b}^*$ is the critical specific energy at the breaking radius, i.e. around the minimum of $Q_\mathrm{D}^*(s)$. Assuming further that $I \propto e$, we can write down the dependencies of the collisional lifetime,

$$T(s) \propto \sigma_\mathrm{tot}^{-1}\cdot s^{3q_\mathrm{p}-5+3(q_\mathrm{p}-1)b_\mathrm{g}}\cdot r^{3/2+q_\mathrm{p}}\cdot\mathrm{d}r\cdot e^{2-2q_\mathrm{p}}. \tag{5.37}$$

O'Brien & Greenberg (2003) yield the same size dependence on s in their equation (11). The dependence on the orbital eccentricities is given by $T \propto e^{-1.75}$ for $q_\mathrm{p} = 1.87$.

To find $s_\mathrm{t}(t)$, the object size below which a steady state is reached, the populations are assumed to move from their primordial state to the quasi-steady state instantaneously when the system age reaches their initial mean collisional lifetime, $T(s_\mathrm{t}) = t$. Inverting that, the resulting mass of objects in transition can be retrieved as a function of system age. Keeping the assumption $X_\mathrm{c} \ll s_\mathrm{max}/s$, the relation is

$$s_\mathrm{t}(t) \quad\propto\quad t^{1/(3q_\mathrm{p}-5+3(q_\mathrm{p}-1)b_\mathrm{g})} \tag{5.38}$$

for $t > T(s_\mathrm{b}) \equiv T_\mathrm{b}$. This transitional size is also plotted in Fig. 5.4.

Pan & Sari (2005) followed a similar approach in their study of the Kuiper-belt size distribution. Describing the propagation of the shock wave through the target, they introduce a parameter β that varies between $3/2$ (if all energy of a projectile goes to the shock wave) and 3 (if all its momentum does). Their β equals $1/b_\mathrm{g}$ in our nomenclature, and $b_\mathrm{g} = 0.5$ leads to $\beta = 2$. Additionally, one has to replace their slope q_0 with $3q_\mathrm{p} - 2$. Then, given their equations (6), (7), and $N_{>s} \propto s^{3-3q_\mathrm{p}}$, the same exponent as in our equation (5.38) is yielded. Note that what Pan & Sari (2005) call "breaking radius" is our "transition radius" s_t, and their "radius of equilibrium" is our "breaking radius" s_b.

5.4.3 Evolution of Disc Mass

Now, the full expression for the time-dependent total disc mass is derived. Using the size distribution given by equation (5.19), n_max from equation (5.22) and expressing $n_\mathrm{max}(0)$ through M_0 with the aid of equation (5.30), one can perform the integration in equation (5.20). Then, the resulting time-dependent

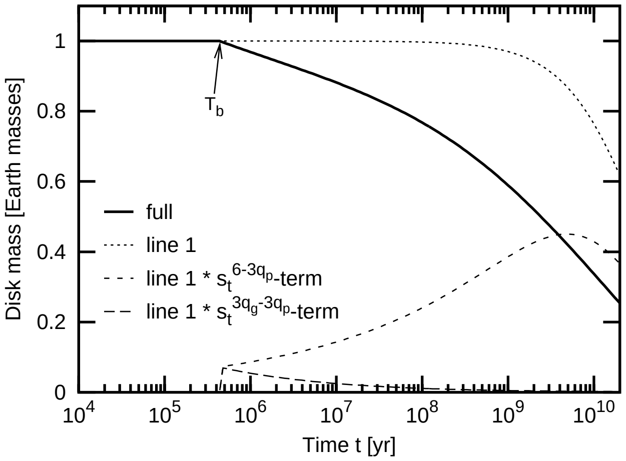

Figure 5.6: The contributions of different terms in equation (5.39) (dotted and dashed lines) and their total (solid line).

disc mass is

$$
\begin{aligned}
M_{\rm disc}(t) &= \frac{M_0}{1+t/T_{\rm max}}\left[1-\left(\frac{s_{\rm min}}{s_{\rm max}}\right)^{6-3q_{\rm p}}\right]^{-1} \\
&\times \left[1-\left(\frac{s_{\rm t}(t)}{s_{\rm b}}\right)^{6-3q_{\rm p}}\left(\frac{s_{\rm b}}{s_{\rm max}}\right)^{6-3q_{\rm p}}\left(1-\frac{2-q_{\rm p}}{2-q_{\rm g}}\right)\right. \\
&+ \left(\frac{s_{\rm t}(t)}{s_{\rm b}}\right)^{3q_{\rm g}-3q_{\rm p}}\left(\frac{s_{\rm b}}{s_{\rm max}}\right)^{6-3q_{\rm p}}\left(\frac{2-q_{\rm p}}{2-q_{\rm s}}-\frac{2-q_{\rm p}}{2-q_{\rm g}}\right) \\
&- \left.\left(\frac{s_{\rm t}(t)}{s_{\rm b}}\right)^{3q_{\rm g}-3q_{\rm p}}\left(\frac{s_{\rm b}}{s_{\rm max}}\right)^{3q_{\rm s}-3q_{\rm p}}\left(\frac{s_{\rm min}}{s_{\rm max}}\right)^{6-3q_{\rm s}}\left(\frac{2-q_{\rm p}}{2-q_{\rm s}}\right)\right]
\end{aligned}
\tag{5.39}
$$

for $T_{\rm b} < t < T_{\rm max}$. To make equation (5.39) valid for earlier phases, i.e. for $t < T_{\rm b}$, $s_{\rm b}$ should be replaced by $s_{\rm t}(t)$. The sizes involved are the maximum object size $s_{\rm max}$, the transition size between the primordial and reprocessed material $s_{\rm t}$, the breaking radius between the gravity and strength regime $s_{\rm b}$. The lower limit in the size distribution, $s_{\rm min}$, is crucial for the dust emission and it is usually taken to be the radiation pressure blowout limit. As long as $q_{\rm p} < 2$, it is fairly unimportant for the mass budget. However, we are interested in $q_{\rm p} \geq 2$ as well. Therefore, we can safely set $s_{\rm min} = 0$ only in the last line of equation (5.39), where it enters through $s_{\rm min}/s_{\rm max}$ to the power of $6-3q_{\rm s}$, with $q_{\rm s} \approx 11/6 < 2$.

The relative importance of the terms in equation (5.39) is illustrated in Fig. 5.6. A combination of the classic Dominik-Decin behavior in the first line of equation (5.39) together with the second line is a reasonably accurate approximation to $M_{\rm disc}(t)$ for most of the time. With the aid of equation (5.38), equation (5.39) transforms to

$$
\begin{aligned}
M_{\rm disc}(t) &\approx \frac{M_0}{1+t/T_{\rm max}}\left[1-\left(\frac{s_{\rm min}}{s_{\rm max}}\right)^{6-3q_{\rm p}}\right]^{-1} \\
&\times \left[1-\left(\frac{s_{\rm b}}{s_{\rm max}}\right)^{6-3q_{\rm p}}\cdot\left(\frac{t}{T_{\rm b}}\right)^{\frac{2-q_{\rm p}}{q_{\rm p}-5/3+(q_{\rm p}-1)b_{\rm g}}}\left(1-\frac{2-q_{\rm p}}{2-q_{\rm g}}\right)\right]
\end{aligned}
\tag{5.40}
$$

for $T_{\rm b} < t < T_{\rm max}$. At $t \ll T_{\rm max}$, and assuming $q_{\rm p} = 1.87$, a further approximation is

$$
M_{\rm disc}(t) \approx M_0\left(1-{\rm const}\cdot t^{0.2}\right). \tag{5.41}
$$

The evolution of the disc mass, both from the numerical runs and from the analytic solution (5.39), is plotted in Fig. 5.7, showing a good agreement between analytics and numerics. A deviation is only seen

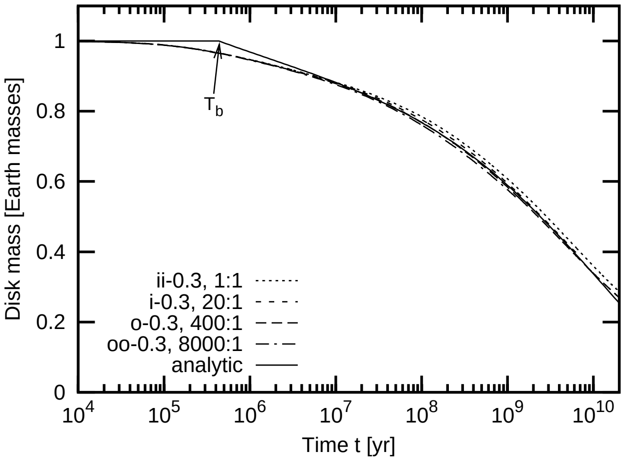

Figure 5.7: Evolution of total masses with (scaled) time, obtained in four numerical runs and with the analytic model.

around $t = T_{\rm b}$ where the transition from primordial to reprocessed state sets on for gravity-dominated objects. The reason is that, to ease the analytic treatment, the smooth natural transition from material strength to self-gravity given by equation (2.27) is neglected, and a sharp break between the two power laws is assumed instead.

5.4.4 Evolution of Disc Mass at Latest Stages

As soon as the age of the system has reached the collisional lifetime of the largest bodies, i.e. at $t > T_{\rm max}$, the solids of all sizes in the disc reach quasi-steady state, and the change in total mass will be dominated by $1/t$. At this latest phase, the projectiles that can destroy objects of size $s_{\rm max}$ no longer follow a size distribution with the primordial slope, $2-3q_{\rm p}$. Instead, they have the slope of a collisional cascade under gravity regime, $2-3q_{\rm g}$. The slightly longer collisional lifetime can neither be expressed through equation (5.23) that uses the *initial* cross section $\sigma_{\rm tot}$ nor through equation (5.32) that contains the initial disc mass M_0 and slope $q_{\rm p}$. The correct way to evaluate $T_{\rm max}$ is to use the initial number density of biggest objects, $n_{\rm max}(0)$, and the slope $q_{\rm g}$. Expressing $\sigma_{\rm tot}$ in equation (5.23) through $n_{\rm max}$ with the help of equation (5.29) and replacing then $q_{\rm p}$ with $q_{\rm g}$, we obtain

$$T_{\rm max} = \frac{12q_{\rm g}-20}{n_{\rm max}(0)\cdot s_{\rm max}^3}\cdot\frac{r^{5/2}{\rm d}r}{(GM_*)^{1/2}}\cdot\frac{I}{f(e,I)G(q_{\rm g},s_{\rm max})}. \tag{5.42}$$

Expressing now $n_{\rm max}(0)$ through M_0 by virtue of equation (5.30) yields

$$\begin{aligned} T_{\rm max} &= \frac{16\pi\rho}{3M_0}\cdot s_{\rm max}\cdot\frac{r^{5/2}{\rm d}r}{(GM_*)^{1/2}} \\ &\times \frac{q_{\rm g}-5/3}{2-q_{\rm p}}\left[1-\left(\frac{s_{\rm min}}{s_{\rm max}}\right)^{6-3q_{\rm p}}\right]^{-1}\frac{I}{f(e,I)G(q_{\rm g},s_{\rm max})}, \end{aligned} \tag{5.43}$$

where both slopes, $q_{\rm p}$ and $q_{\rm g}$, appear (cf. Eqs. 5.23 and 5.32).

5.4.5 Evolution of Mass in Dynamically “Cold” Discs

All the treatment above applies to planetesimal belts where relative velocities are high enough for the biggest objects to be destroyed by mutual collisions. This might not be the case in dynamically “cold” discs with low eccentricities and inclinations and/or very far from the star.

Consider again the lifetime of objects $T(s)$. As s increases, $X_{\rm c}(s)$ (Eq. 5.26) increases too and at a certain point reaches $s_{\rm max}/s$. At this point, G (Eq. 5.25) becomes zero and $T(s)$ (Eq. 5.32) goes to infinity. This means that, for a given impact velocity, objects above a certain critical size cannot be

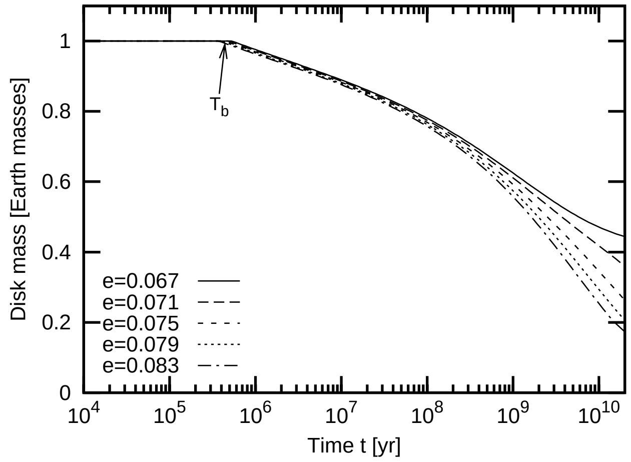

Figure 5.8: Influence of the effective eccentricity assumed in the analytic model for a disc of 1 $M_\oplus$ at $r = 10$ AU with a radial extent d$r = 7.5$ AU. The $I = e/2$ relation between eccentricity and inclination is assumed.

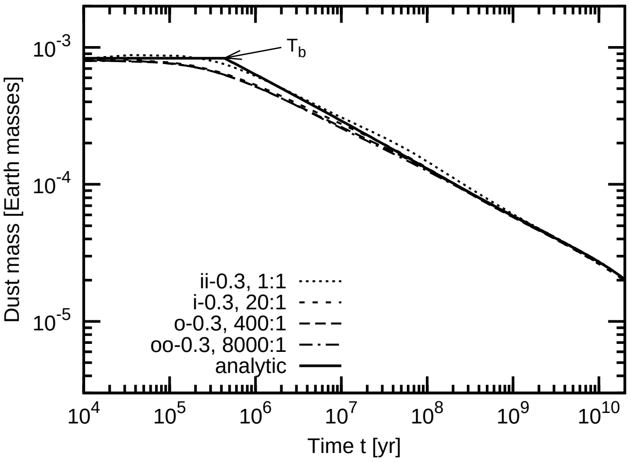

Figure 5.9: Similar to Fig. 5.7 but for dust masses, i.e. masses in particles with radii below 1 mm.

disrupted anymore. In systems with low relative velocities, that critical size may happen to be smaller than $s_{\rm max}$. This will affect the mass evolution. Specifically, when $s_{\rm t}$ reaches that critical size, the overall mass decay ceases in the analytic model.

To illustrate such effects, Fig. 5.8 shows the influence of the effective e and I on the evolution of the total mass of a disc of initially 1 $M_\oplus$ at an effective distance of 10 AU, calculated with our analytic model. For colder discs, the curves start to flatten. This happens because the largest planetesimals (that dominate the total mass) stay intact, which slows down the mass loss.

5.4.6 Evolution of Dust Mass

The dust mass can be evaluated in a similar way as the disc mass. We use now equations (5.19), (5.21), (5.22), (5.30), and (5.38). Neglecting the minimum mass $s_{\rm min}$ only when it enters the formula through $s_{\rm min}/s_{\rm max}$, we obtain

$$
\begin{aligned}
M_{\rm dust}(t) = {} & \frac{M_0}{1+t/T_{\rm max}} \cdot \left(\frac{t}{T_{\rm b}}\right)^{\frac{q_{\rm g}-q_{\rm p}}{q_{\rm p}-5/3+(q_{\rm p}-1)b_{\rm g}}} \cdot \frac{2-q_{\rm p}}{2-q_{\rm s}} \\
& \times \left(\frac{s_{\rm b}}{s_{\rm max}}\right)^{2-q_{\rm p}} \left[\left(\frac{s_{\rm d}}{s_{\rm b}}\right)^{2-q_{\rm s}} - \left(\frac{s_{\rm min}}{s_{\rm b}}\right)^{2-q_{\rm s}}\right]^{-1} \qquad (5.44)
\end{aligned}
$$

for $T_{\rm b} < t < T_{\rm max}$. Before that, i.e. at $t < T_{\rm b}$, we have $q_{\rm s}$ and $b_{\rm s}$ instead of $q_{\rm g}$ and $b_{\rm g}$, respectively. If the assumed primordial slope, $q_{\rm p}$, equals the steady-state slope in the strength regime, $q_{\rm s}$, the dust mass stays constant, which is the case for the first part of the numerical integration. However, as soon as the transitional zone reaches objects large enough to be influenced by self-gravity, equation (5.44) starts to work. It shows that the evolution of dust mass depends most strongly on the difference between q_p and q_g. The dust mass decay, obtained both from the numerical runs and analytic solution (5.44), are shown in Fig. 5.9. For $t > T_\mathrm{b}$, we roughly have $M_\mathrm{dust} \propto t^\xi$ with $\xi \approx -0.3$.

Finally, one should note that equation (5.44) is valid as long as the collisional lifetime of the largest planetesimals exceeds the age of the system. When $t > T_\mathrm{max}$, t/T_b in that equation must be replaced by $T_\mathrm{max}/T_\mathrm{b}$.

5.4.7 The Slope of the Steady-State Size Distribution

If one assumes the size distribution to follow a power law

$$\mathrm{d}N = n_0 \frac{m}{m_0}^{-q} \mathrm{d}m, \tag{5.45}$$

the total mass of such a system can be obtained by integrating $\mathrm{d}M = m\mathrm{d}N$ and is given by

$$M = \frac{n_0 m_\mathrm{max}^{2-q}}{m_0^{-q}(2-q)} \tag{5.46}$$

for $q < 2$ and $m_0 \ll m_\mathrm{max}$. In order to derive an equilibrium slope q, for which the distribution evolves in a self-similar way, the mass loss of such a system can be used:

$$\dot{M} = \frac{M}{T} = \frac{M}{T_\mathrm{max}}, \tag{5.47}$$

where T is the lifetime of the disc, which equals the lifetime of the unreplenished biggest objects, i.e. $T = T_\mathrm{max}$. Assuming $n_0 = \mathrm{const}$, i.e. a fixed amount of dust, and using equation (5.37) with $m \propto s^3$, the dependence of $\dot{M}$ on m_max can be resolved:

$$\dot{M} \propto \frac{m_\mathrm{max}^{2-q}}{m_\mathrm{max}^{q-5/3+b(q-1)}} = m_\mathrm{max}^{11/3-2q-b(q-1)}. \tag{5.48}$$

However, if collisions are the dominating process, mass can only be removed from a debris disc in the form of small particles that get blown out of the system by the stellar radiation pressure. Therefore, $\dot{M}$ should be independent from the actual size of the biggest objects (as long as the dust mass is fixed). This statement is equivalent to

$$11/3 - 2q - b(q-1) \overset{!}{=} 0. \tag{5.49}$$

Thus, the resulting power-law index for quasi-steady state is

$$q = \frac{11+3b}{6+3b}. \tag{5.50}$$

The approach used by O'Brien & Greenberg (2003) leads to the same result, although it is less handy because it invokes not only the lifetime, i.e. the loss of material, but also the gain. As shown above, the latter is not necessary.

5.4.8 Model Parameters

Our analytic model contains several parameters that either differ from similar parameters in the numerical model (such as e) or are absent there (such as q_s and q_g). To use the analytic model, they have got to be specified. In what follows, a description of how this can be done is given, explaining, in particular, the choice of parameters used to plot analytic curves in Figs. 5.6–5.9.

Two important free parameters of the analytic model are q_s and q_g. With the dependence of the critical

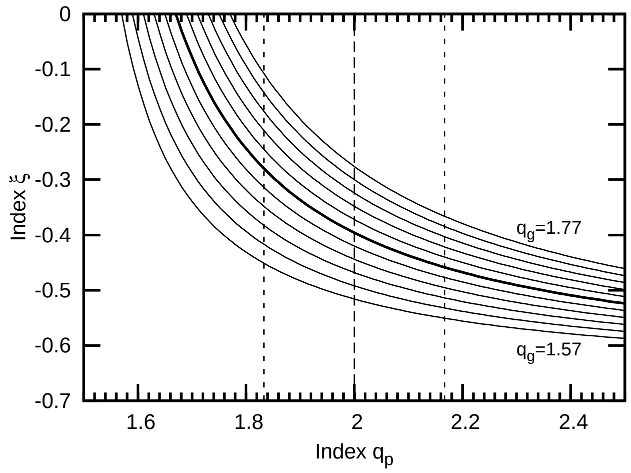

Figure 5.10: Index ξ of the power-law evolution of the dust mass, $M_{\rm d} \propto t^{\xi}$. The horizontal axis gives the dependence on the slope of the primordial mass distribution, $q_{\rm p}$, for values from $q_{\rm g} = 1.57$ (bottom) to $q_{\rm g} = 1.77$ (top) for the slope in the gravity regime. The bold line is for $q_{\rm g} = 1.67 \approx 5/3$. Vertical lines indicate the mean value and error estimates for $q_{\rm p}$ from Trujillo et al. (2001).

specific energy on the object size given in equation (2.27), and using $b = b_{\rm s} = -0.1$ for the strength regime, we find $q = q_{\rm s} = 1.877$ from equation (5.50). Similarly, with $b = b_{\rm g} = 0.5$ for the gravity regime, the result is $q_{\rm g} \approx 5/3$. It is these values that were used in equation (5.39) to produce Figs. 5.6–5.8 and in equation (5.44) to plot Fig. 5.9.

In contrast to $q_{\rm s}$ and $q_{\rm g}$, the primordial slope, $q_{\rm p}$, is a free parameter not only in the analytic model, but also in the numerical one. As stated in Sect. 5.2.1, in all "nominal" runs it was assumed that $q_{\rm p} = 1.87$, which corresponds to $p_{\rm p} = 3q_{\rm p} - 2 = 3.61$ in the size scaling. In principle, $q_{\rm p}$ describes the mass distribution at the onset of the collisional grinding of the disc and, therefore, represents a link to the planetesimal formation process. The outcome of the agglomeration phase is the input to the phase of disruptive collisions. The Kuiper belt is the only source for observational constraints to this parameter so far, and recent surveys suggest a value of $p_{\rm p} = 4.0 \pm 0.5$ (e.g., Trujillo et al. 2001; Bernstein et al. 2004) or $q_{\rm p} = 2.00 \pm 0.17$. Simulations by Kenyon & Bromley (2004) yield $p_{\rm p} = 4.0$–4.5 or $q_{\rm p} = 2.00$–2.17. According to equation (5.44), where we have $M_{\rm dust} \propto t^{\xi}$, and together with $q_{\rm g} \approx 1.67$, this would change the dust mass evolution from $M_{\rm dust} \propto t^{-0.32}$ for $q_{\rm p} = 1.87$ to $M_{\rm dust} \propto t^{-0.40}$ for $q_{\rm p} = 2.00$. Fig. 5.10 shows the rather moderate dependence of the index ξ on the two mass distribution slopes, $q_{\rm g}$ and $q_{\rm p}$.

While the dust size limit, $s_{\rm d}$, has little influence on the mass budget, the breaking size, $s_{\rm b}$, the maximum size, $s_{\rm max}$, and the ratio of the two are relevant to the evolution as they define the lifetime of the largest bodies $T_{\rm max}$ relative to $T_{\rm b}$. What is more, the ratio $s_{\rm b}/s_{\rm max}$ determines the rate of the mass decay in equation (5.40). From Sect. 2.2.1 we know the location of the breaking radius to be 316 m for the material properties assumed, and the upper size limit of all the runs was set to $s_{\rm max} = 74$ km.

Another parameter in the analytic model is the collisional lifetime of objects of breaking radius, $T_{\rm b} = T(s_{\rm b})$. Equation (5.32) expresses it through other parameters critical for the efficiency of collisions: the radial distance to the star r, the disc radial extension dr, and the effective eccentricity e and inclination I. Both the effective distance and the disc extension were chosen to be fixed at $r = \frac{4}{3}{\rm d}r = 10$ AU when reproducing analytically the results of the ii-0.3 run, 20 AU for i-0.3, 40 AU for o-0.3, and 80 AU for oo-0.3. Further, the inclination can be coupled to eccentricity by assuming the equilibrium condition $I = e/2$. Thus, only e remains as a free parameter. The best fit to, e.g., the ii-0.3 run is achieved if $e \approx 0.075$ is assumed in the analytic model, which is approximately one quarter of $e_{\rm max} = 0.3$. With these choices, it is found that $T(s_{\rm b}) \approx 4 \times 10^5$ years.

Alternatively, $T_{\rm b}$ can be directly retrieved from the break in the evolution of the dust mass (see Fig. 5.9). This method gives $T(s_{\rm b}) \approx 5 \times 10^5$ years, which is approximately $4/3$ times the value calculated with equation (5.32). This discrepancy is probably a result of the particle-in-a-box assumptions made in derivation of equation (5.23). Thus, the empirical scaling is preferred and the factor of $4/3$ applied to all analytically estimated timescales.

5.5 Evolution of Disc Luminosity

5.5.1 Fractional Luminosity for a Given Age

Following Wyatt et al. (2007a), let the fractional luminosity of dust be defined as

$$f_{\rm d} \equiv \sigma_{\rm tot}/(4\pi r^2), \tag{5.51}$$

which assumes that dust grains are black bodies, absorbing and re-emitting all the radiation they intercept. Wyatt et al. (2007a, their Eq. 20) found that there is a maximum possible fractional luminosity $f_{\rm max}$ for a given age, whose value is independent of the initial disc mass, but depends on other model parameters such as the distance r of the disc centre from the star, its width dr, size of the largest planetesimals $D_{\rm c}$, critical fragmentation energy $Q_{\rm D}^*$, orbital eccentricity of planetesimals e (with their inclination being $I = e/2$), as well as the stellar mass M_* and luminosity L_*.

Now $f_d(t)$ shall be explored, and it shall be checked whether it has an upper limit in the framework of the analytic model. To this end, equation (5.51) is used and $\sigma_{\rm tot}$ calculated with the aid of equation (5.44) for the dust mass. A solar-type star with $M_* = L_* = 1$ is assumed and discs are probed with $M_{\rm disc} = 1, 3, 10$, and $30 M_\oplus$; $r = 3, 10, 30$, and 100 AU; d$r/r = 1/8, 1/4, 1/2$, and 1; $e = 0.05, 0.10, 0.15$, and 0.20. The results are presented in Fig. 5.11 (thick lines). As a standard case, $M_{\rm disc} = 10 M_\oplus$, $r = 30$ AU, d$r/r = 1/2$, and $e = 0.10$ is adopted. It is shown with a thick solid curve in each of the panels.

In the same Fig. 5.11, the dust luminosity $f_{\rm d}$ computed with equations (14), (19), and (20) of Wyatt et al. (2007a) is overplotted with thin lines, for comparison. In that calculation, we assumed $Q_{\rm D}^* =$ 300 J/kg (constant in their model), $D_{\rm c} = 60$ km, and the same values of those parameters that are common in their and our model (M_*, L_*, r, dr/r, and e).

Analysis of Fig. 5.11 allows us to make a number of conclusions. First, as expected, our model yields more gently sloping curves than that by Wyatt et al. As discussed above, the $1/t$ law will be asymptotically reached in our model, too, but this does rarely happen at ages $t < 10$ Gyr. Only the first signs of the curves' steepening appear at Gyr ages, and that only for the cases when the collisional evolution is faster (higher masses, closer-in or more confined dust rings, higher eccentricities). As a consequence of the slope difference between the two models, our model places more stringent upper limits on $f_{\rm d}$ at earlier ages, and conversely, it allows the Gyr-old systems to have a somewhat higher $f_{\rm d}$ than the model by Wyatt et al. does.

Next, the dependence of $f_{\rm max}$ on the initial disc mass, which cancels out in their model, is retained in our nominal runs (the top left panel). In fact, the maximum possible $f_{\rm d}$ is then determined by the maximum initial disc mass that still appears physically plausible in the framework of theories of planetesimal accretion and planet formation.

Another point to mention is that, whereas the dependence on the disc width (bottom right) and planetesimal eccentricities is relatively weak and monotonic, the dependence on the disc location (top right) is rather strong and more intricate. That the dependence is strong is the consequence of equation (5.16) that predicts the timescales to very sensitively depend on the distance from the star, and of equation (5.51) that contains a "dilution factor" r^2. At the beginning of the evolution, the innermost ring is always the brightest because the dilution factor r^2 in equation (5.51) is the smallest. At the end of the evolution, the opposite is true: the outermost ring will become the brightest, because its collisional evolution is the slowest and it retains more mass than inner discs. Therefore, all four curves intersect each other at a certain point; the 30 and 100 AU curve do that after 10 Gyr, i.e. outside that right edge of the plot. After that, all the curves go parallel to each other in the "Dominik-Decin regime", following a $1/t$ law and finally t^{-2} when P-R drag dominates. Note that inner rings reach the $1/t$ regime more quickly: already at 10 AU it is established in around 100 Myr for an initial mass of 10 $M_\oplus$.

Although the existence of a "maximum fractional luminosity for a given age", as suggested by Wyatt et al. (2007a), no longer holds in our model as a robust mathematical statement, in practice our model still suggests that $f_{\rm d}(t)$ cannot exceed a certain limit, unless the model parameters take extreme values, incompatible with our understanding of the planetesimal discs. For instance, we do expect $f_{\rm d} < 10^{-4}$ at

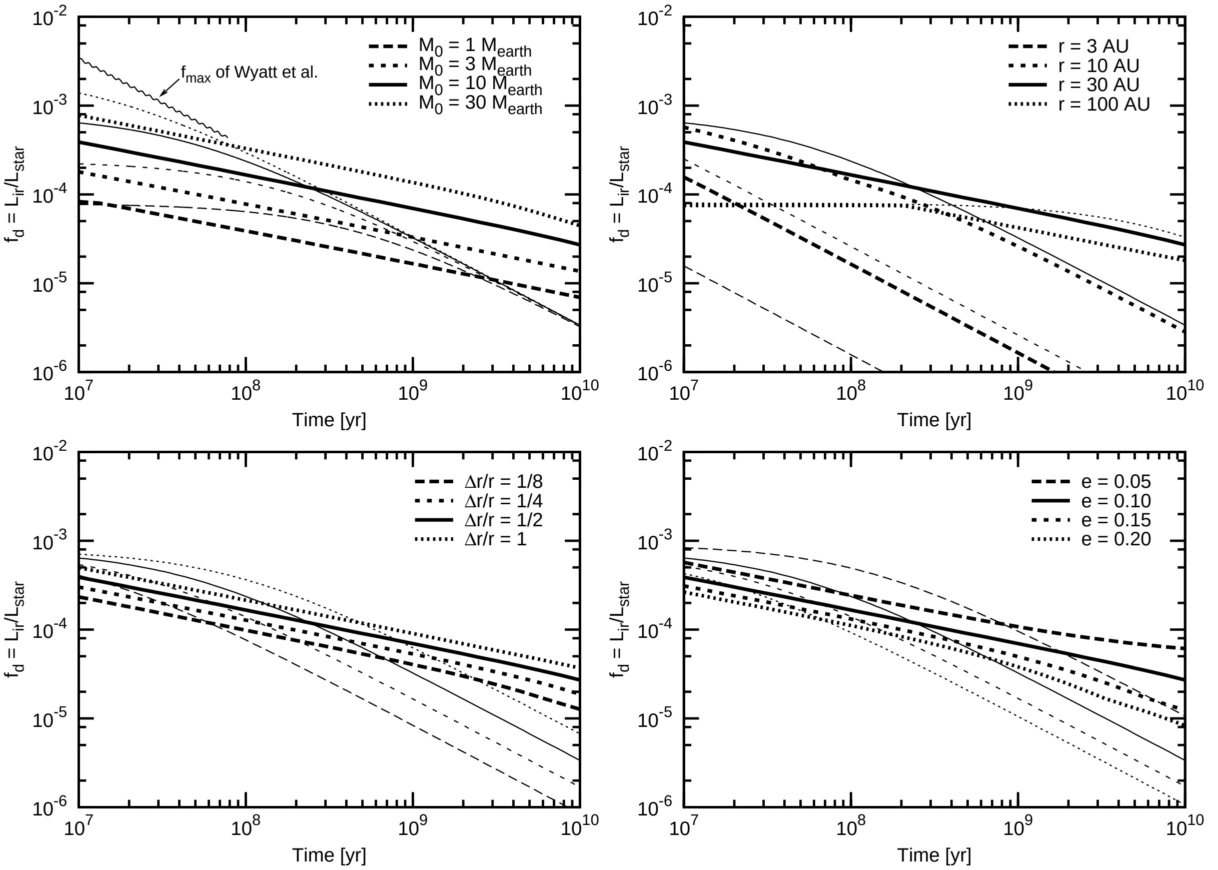

Figure 5.11: Fractional luminosity of dust around a solar-like star as a function of age. Thick lines: our analytic model; thin lines: $f_{\rm d}$ of Wyatt et al. (2007a). Different panels demonstrate dependence on different parameters: $M_{\rm disc}$ *(top left)*, r *(top right)*, $\mathrm{d}r/r$ *(bottom left)*, and e *(bottom right)*. A standard case with $M_* = L_* = 1$, $M_{\rm disc} = 10 M_\oplus$, $r = 30$ AU, $\mathrm{d}r/r = 1/2$, and $e = 0.10$ is shown with solid lines (common in all panels).

$t = 10$ Gyr, provided that the initial disc did not contain more than 30 Earth masses of solids and that the mean orbital eccentricity of planetesimals is not lower than 0.1 (corresponding to the mean inclination larger than 3°). Therefore, plots such as Fig. 5.11 can be used to check whether or not $f_{\rm d}$ observed for a certain system with a known age is compatible with a "smooth", unperturbed collisional evolutionary scenario. In case it is not, it will be an indication that other mechanisms (delayed stirring, recent giant break-ups, non-collisional dust production etc.) should be thought of to explain the observations.

5.5.2 24 and 70 Micron Fluxes from Partial Rings

In order to produce directly observable quantities from the derived dust masses, the focus is now set to dust luminosities at particular infrared wavelengths. The dust temperature and the thermal emission integrated over the whole disc are calculated with a more accurate, yet sufficiently simple, model, assuming that the absorption/emission efficiency is constant up to wavelengths of 2π times the size of the particles, s, and proportional to s^{-1} beyond that (Backman & Paresce 1993). Then the spectral flux densities of dust emission $F_{\rm d}$ and of the stellar radiation F_* are computed at a certain wavelength, as well as their ratio $F_{\rm d}/F_*$. As the size distribution in the dust regime quickly reaches its steady state, the luminosity $F_{\rm d}$ is directly proportional to the dust mass. Therefore, the same initial constancy and subsequent t^ξ decay with $\xi = -0.3 \ldots -0.4$ apply.

Fig. 5.12 shows the evolution of the excess emission at the Spitzer/MIPS wavelengths 24 and 70 μm,

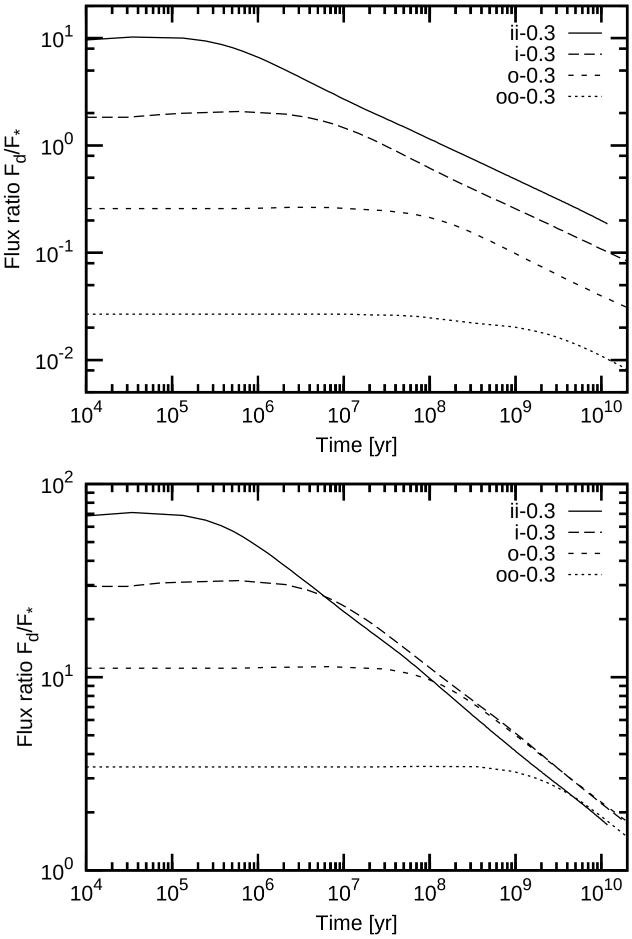

Figure 5.12: Flux ratio versus time for *(top)* 24 µm and *(bottom)* 70 µm.

obtained from the four nominal runs. Since all discs have the same initial total mass (1 $M_\oplus$), the discs closer to the star are brighter and start to decay earlier. The difference between the excesses at 24 and 70 µm, a measure of the discs' effective temperature, is varying with radial distance as well. Thus, the convergence of just the 70 µm fluxes at later times is only coincidental. It is a result of the radial dependence of temperature and the collisional timescale.

5.5.3 Fluxes from Extended Discs

Since resolved debris discs suggest that the parent body reservoir in the discs is usually confined to a toroidal region (a planetesimal belt), or is made up of several such tori, it seems appropriate to simply combine individual rings without taking into account possible interactions between particles that belong to different rings. Thus, the fluxes from the four main runs were summed up. Different radial distributions in the whole disc were simulated by "weighting" the individual rings:

$$F_\mathrm{d} = \sum_{j=1}^{4} F_{\mathrm{d,j}} (r_j/r_0)^\gamma, \tag{5.52}$$

where r_j are the central distances of the rings and values of 0, 1, 2, and 3 were used for the slope γ. As the reference runs were made for rings of one Earth mass each with volumes proportional to r^3, the corresponding volume density in the extended disc is proportional to $r^{\gamma-3}$, while the pole-on surface density and normal geometrical optical depth follow $\propto r^{\gamma-2}$. The distance r_0 normalizes the total mass to $1 M_\oplus$. Therefore, by changing the slope, the mass is only shifted between inner and outer regions.

In Fig. 5.13 the effect on the 24 and 70 µm fluxes is shown. If the weights are assigned in favor of more distant debris rings, the resulting fluxes are naturally reduced. The same is true for the speed of the decay

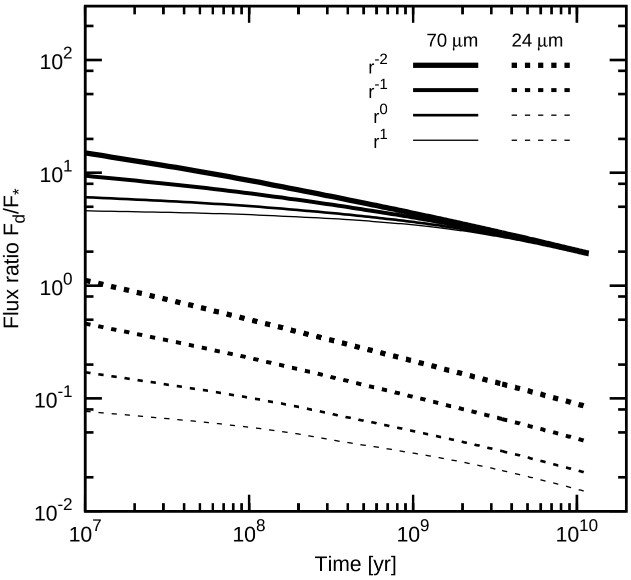

Figure 5.13: Time evolution of the infrared excess of extended discs with different initial radial distributions (labels indicate the radial slope of the surface mass density; the thicker the lines, the flatter the profiles) at 24 μm (dashed lines) and 70 μm (solid lines). The total mass is $1M_\oplus$ in each case.

because the timescales get longer. The evolution of the fluxes at the two Spitzer/MIPS wavelengths 24 and 70 μm differs significantly. At 24 μm, the decay starts earlier and reaches its maximum speed earlier because shorter-lived inner regions make the main contribution.

The models contain a sufficient number of parameters, variation of which would affect the curves in Fig. 5.13 in different ways. As stated earlier, varying the total mass changes the timescale according to $T \propto M_{\rm disc}^{-1}$. Hence, the curves can be shifted along the lines of equal $t \cdot M_{\rm disc}$, i.e. along the top left – bottom right diagonal. As seen from Fig. 5.13, variation of the radial distribution changes both the absolute level and the tilt of the curves. Besides, it affects the disc colours, i.e. the separation of the 24 and 70 μm curves in Fig. 5.13. In addition, the dynamical timescales, and therefore the tilt of the curves, are affected by eccentricities and inclinations of the parent bodies that may reflect the presence of planetary perturbers in the disc (see Sect. 5.3.3). Altogether, these degrees of freedom would allow one to reproduce a broad set of observational data.

5.6 Comparison with Observational Data

5.6.1 Spitzer Data

In recent years, various photometric surveys of hundreds of nearby stars have been conducted with the Spitzer Space Telescope. These are the GTO survey of FGK stars (Beichman et al. 2005; Bryden et al. 2006; Beichman et al. 2006a; Trilling et al. 2008), the FEPS Legacy project (Meyer et al. 2004; Kim et al. 2005; Hillenbrand et al. 2008; Meyer et al. 2008), the A star GTO programmes (Rieke et al. 2005; Su et al. 2006), the young cluster programmes (Gorlova et al. 2006), and others. These observations were done mostly at 24 and 70 μm with the MIPS photometer, but also between 5 and 40 μm with the IRS spectrometer (Jura et al. 2004; Chen et al. 2006). Based on these studies, about 15% of mature solar-type (F0–K0) stars have been found to harbour cold debris discs at 70 μm. For cooler stars, the fraction drops to 0%–4% (Beichman et al. 2006a). For earlier spectral types, the proportion increases to about 30% (Su et al. 2006; Trilling et al. 2008). At 24 μm, the fraction of systems with detected excess stays similar for A stars, but appreciably decreases for FGK ones. Trilling et al. (2007) report a significantly increased dust incidence for binary star systems with A and F stars. Similar results in the sub-millimeter range are expected to become available soon from a survey with SCUBA and SCUBA2 on the James Clerk Maxwell Telescope (JCMT) (Matthews et al. 2007). Preliminary SCUBA results for M dwarfs show, in particular, a fraction of systems with observed debris discs which is higher than that found by Spitzer (Lestrade et al. 2006).

The advent of the Spitzer Space Observatory has brought a tremendous increase in the number of main-sequence stars surveyed for the existence of cold dust emission (see Werner et al. (2006) for a recent compilation).

The wealth of data from these debris disc surveys allows to confront the models with actual observations. To this end, the literature was searched for published flux ratios at 24 and/or 70 µm (two of the three MIPS bands) around G-type main-sequence stars. To qualify as a main-sequence star a lower limit of 10 Myr was set to the stellar age. Sources with stellar age estimates younger than this are likely stars with gas-dominated, protoplanetary discs; these were not taken into account.

The bulk of the data taken in the framework of the Legacy programme "Formation and Evolution of Planetary Systems" (FEPS) (Meyer et al. 2004, 2006) is public since December 2006. The FEPS archive contains images, spectra, photometry tables and Kurucz photosphere models and is available at http://data.spitzer.caltech.edu/popular/feps/20061223_enhanced_v1/. Age estimates have been published for 46 FEPS G stars (Kim et al. 2005; Stauffer et al. 2005; Silverstone et al. 2006). [Addendum.—The data for 18 additional objects have been drawn from Hillenbrand et al. (2008).]

The large Guaranteed Time Observer (GTO) survey of FGK stars contains another 94 stars, where ages are available (Beichman et al. 2005, 2006a; Bryden et al. 2006; Trilling et al. 2008). Data for ten more G stars are listed in Chen et al. (2005a,b).

In total, 169 G-type main-sequence stars with flux ratios at 24 and/or 70 μm have been compiled from the literature for comparison with model flux ratios. Of those stars, only a small fraction has significant excess (3σ). However, for this work, even insignificant excess is plotted in the diagrams as long as the excess is positive.

5.6.2 Population Synthesis

Based on the analytic prescription presented in Sect. 5.4 and motivated by the Wyatt et al. (2007b) work, a synthetic set of debris discs around G2 stars is now built. We generate a set of ring-like discs of width $\mathrm{d}r$ located at distances $r \in [r_{\mathrm{min}}, r_{\mathrm{max}}]$, with masses $M_{\mathrm{disc}} \in [M_{\mathrm{min}}, M_{\mathrm{max}}]$, and ages between 10 Myr and 10 Gyr. The probability to have a disc of initial mass M_0 at radius r was assumed to follow $M_0^{-1} r^{-0.8}$, where M_0^{-1} corresponds to a log-normal distribution of initial disc masses and the $r^{-0.8}$ dependence was proposed by Wyatt et al. (2007b). As described in Sect. 5.5.2, the temperatures and the resulting thermal fluxes are calculated using the modified black-body formulas by Backman & Paresce (1993), assuming the emitting grains to have $s = 1$ µm, in agreement with the size distribution shown in Fig. 5.4. The other parameters are taken to be: $q_{\mathrm{p}} = 2.00$, $q_{\mathrm{g}} = 1.67$, $q_{\mathrm{s}} = 1.877$, $\mathrm{d}r/r = 0.5$, $2I = e = 0.15$, $Q_{\mathrm{D}}^{*}(1\,\mathrm{m}) = Q_{\mathrm{D}}^{*}(1\,\mathrm{km}) = 5 \times 10^{6}$ erg/g, $b_{\mathrm{d}} = -0.12$, $b_{\mathrm{g}} = 0.47$, roughly corresponding to basalt in Benz & Asphaug (1999). Due to the small observational sample, our aim was not to perform a multi-parameter fit to the observations, but rather to cover the range of observed flux densities, which is defined by the limits of the distributions, not by their slopes.

Varying disc locations and masses easily reproduces the observed distribution of fluxes at 24 µm and 70 µm (Fig. 5.14). The synthetic population shown corresponds to $r_{\mathrm{min}} \approx 25$ AU, $r_{\mathrm{max}} \approx 150$ AU and $M_{\mathrm{min}} < 0.01\ M_{\oplus}$, $M_{\mathrm{max}} \approx 50\ M_{\oplus}$. [Addendum.—These values are slightly different from the ones used in Löhne et al. (2008) but lead to similar results.] Here, the radial range is needed to cover the range of colours, i.e. the ratios between the excess emissions at the two wavelengths. The mass range is needed to cover the observed range of excess, especially for younger discs at 70 µm.

Analyses of Spitzer detections might indicate a statistically significant increase of both 24 and 70 µm fluxes at ages between a few tens of Myr to a few hundreds of Myr. (e.g., J. M. Carpenter et al., in prep.), which can only be marginally seen in our sample (Fig. 5.14). It is hypothesized that this feature is caused either by an increased dust production due to delayed stirring by growing planets or by events similar to the late heavy bombardment in the solar system. Such effect could only be studied with an improved version of the analytic model or with the numerical one.

The distribution of disc colours is more difficult to reproduce. Fig. 5.15 shows a significant abundance of fainter but warmer discs in an area that is not covered by the synthetic population. One explanation

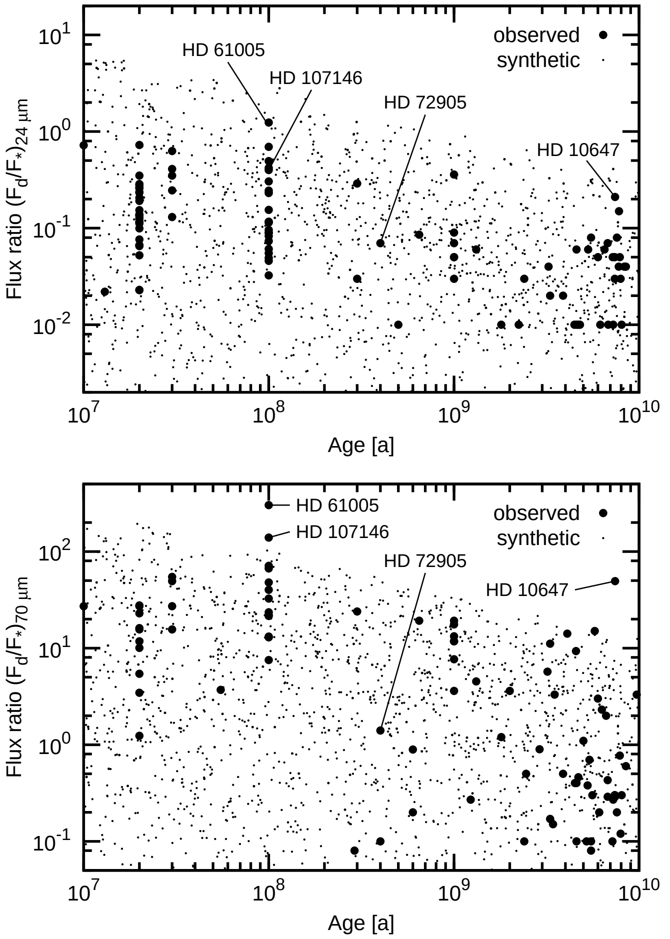

Figure 5.14: Flux ratios versus time for 24 µm *(top)* and 70 µm *(bottom)*. The synthesized population (*small dots*) is compared to the observed one (*big dots*). Individually labeled is the possibly transient system HD 72905, see text.

would be that the upper mass limit is a function of radial distance, and that the innermost discs tend to be less massive and less luminous, from the very beginning. In addition, the lower panel of that Fig. 5.15 shows a trend towards higher effective temperatures for higher ages, which is difficult to understand. Indeed, as long as faint close-in discs are observed around older stars, one would expect ever brighter discs, and therefore more numerous detections of discs at the same distances around younger stars. Furthermore, the trend in question contradicts to the results by Najita & Williams (2005), who found no significant correlation between the disc radii and ages. Most likely, the discrepancy is only caused by uncertainties of the measured excesses at 24 µm. Bryden et al. (2006) report that the average photometric accuracy in that filter band is only as good as $1\sigma_{24} = 6\%$ due to stellar photosphere fitting errors and flat-field uncertainties. Therefore, excesses below those 6% of the photospheric emission cannot be considered as significant. For 70 µm, Bryden et al. (2006) state $1\sigma_{70} \approx 15\%$. Both limits are shown in the upper panel of Fig. 5.15. [Addendum.—This upper panel also shows a lack of bright and warm discs in the observed population when compared to the synthetic one. This might be an indication that mechanisms other than collisional erosion are responsible for the depletion of those inner discs or disc regions.]

In Figs. 5.14 and 5.15, there is are four particular systems directly labeled. One system, HD 72905, was observed to show significant excess emission not only at 24 and 70 µm, but also in the spectral ranges 8–13 and 30–34 µm of the Spitzer/IRS instrument (Beichman et al. 2006b). The presence of two dusty regions was suggested: one exozodiacal at 0.03–0.43 AU and one around 14 AU. From the excess at 8–13 µm, Wyatt et al. (2007a) inferred the dust population in HD 72905 to be transient because the observed fractional luminosity is above the maximum expected for a system of 300–400 Myr. As long as only 24 and 70 µm are considered, the HD 72905 dust does not seem particularly hot or bright, although it is among the hotter discs. [Addendum.—The other systems, namely HD 61005, HD 107146,

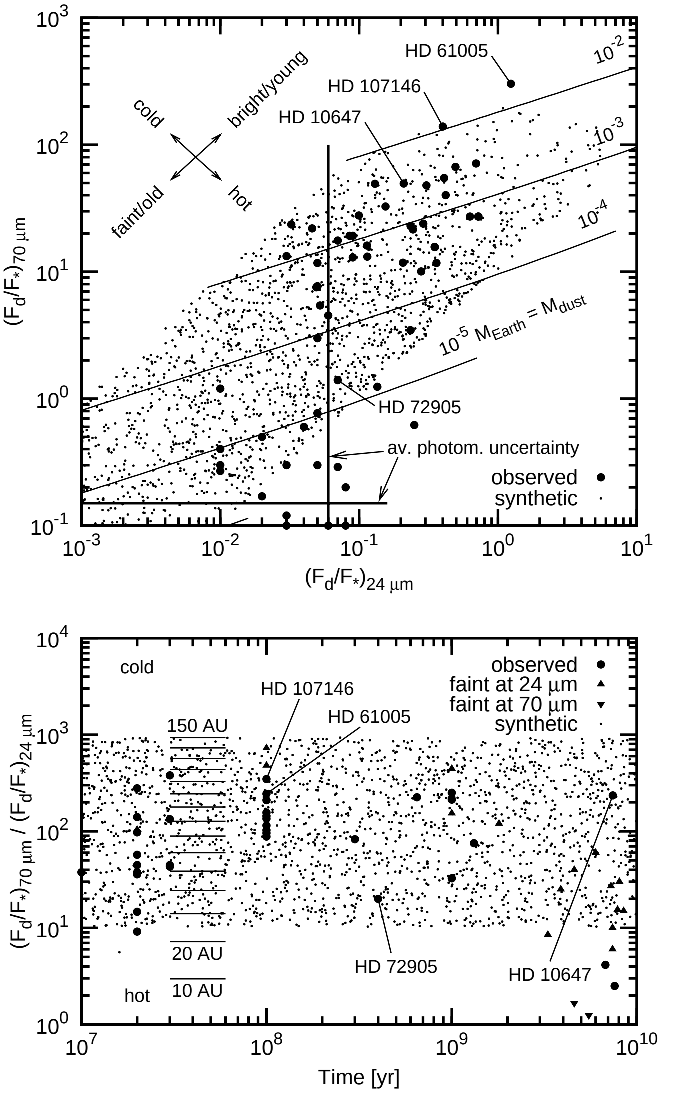

Figure 5.15: Relation between fluxes at 24 and 70 μm versus time. The synthesized population (*small dots*) is compared to the observed one (*big dots and triangles*). The average photospheric uncertainty for both filters is marked by dashed lines in the upper panel. Excesses below those limits in either of the two filters are marked by triangles in the lower panel. In addition, the upper panel shows lines of equal dust mass and the lower panel gives the ring radii corresponding to the colours.

and HD 10647 (q^1 Eri), are prominent due to their strong excess.]

At this point, it is interesting to compare our results to those of Wyatt et al. (2007b). Both analytic approaches aim at explaining and reproducing the observations. Our model is different from theirs in that we take into account the size dependence of the critical specific energy as well as the transition from a "primordial" size distribution of planetesimals to the one set up by a collisional cascade. The amount of dust in their model is determined, from the very beginning, by the rather long collisional timescales of objects of tens of kilometers, so that the collisional evolution is much slower. This can be seen from the equations: "1+" in the denominator of equation (5.13) causes the mass to stay almost at the initial level for a long time, before the system reaches the t^{-1} decay. In our model, although the mass decay is asymptotically slower (t^{ξ} with $\xi \approx -0.3\ldots-0.4$), it sets up very quickly, namely on collisional timescales of objects with minimum binding energy ($s_b \sim 100$ meters). Therefore, one would expect the model by Wyatt et al. (2007b) to show significantly larger excesses at ages considered, if all other parameters were comparable. This, however, is not the case. Wyatt et al. (2007b) assumed a much weaker material in their collisional prescription. Their $Q_{\mathrm{D}}^{*} = 300$ J/kg at an object radius of 30 km ($D_{\mathrm{c}} = 60$ km) is by more than two orders of magnitude below the values used in equation (2.27). As $T \propto Q_{\mathrm{D}}^{q_{\mathrm{p}}-1}$ in equation (5.35), their collisional timescales are shorter and their evolution faster, too. Besides the material strength, the difference in the assumed effective eccentricities—$e = 0.05$ in their model against $e_{\max}/2 = 0.15$ in ours—causes another factor of roughly 10 in the collisional timescales, according to Sect. 5.3.3. All the differences listed happen to nearly compensate each other. As a net result, the excesses predicted by Wyatt's et al. and our models are comparable with each other (see also Fig. 5.11), being in reasonable agreement with the observed ones.

6 Summary and Conclusions

The subject of this work has been “typical circumstellar debris discs”. Instead of including a large array of forces and effects to reproduce particular observed systems, the focus has been set on a few fundamental physical effects and on the development of a kind of reference model.

Thus, the disc is treated as an idealized ensemble of objects from micron-sized dust to kilometre-sized planetesimals, exposed to stellar gravity and direct radiation pressure and experiencing mainly fragmenting collisions. The method used can be referred to as a “kinetic theory in orbital elements”. It was successfully implemented into a numerical code that can simultaneously handle a size distribution that spans many orders of magnitude and that is strictly entangled with the radial distribution, especially for dust. Solving a balance equation for material gain and loss, a three-dimensional distribution of mass, semimajor axes, and eccentricities is obtained, which can easily be transformed to “usual” distributions, such as size distribution or radial profiles. The approach is shown to be also suitable for transport-dominated discs, where slight gas drag, Poynting-Robertson drag, or corpuscular drag due to stellar wind are important. However, these discs are *not* detailed here. The main interest was to identify several essential, generic properties of a collision-dominated rotationally symmetric disc.

We have investigated what kind of size or mass and spatial distributions of the disc material can be expected from theory, and how these distributions might depend on the distribution of the parent bodies, the parameters of the central star, and the grain properties. With a number of tests, the genericity of the characterisitics found is checked.

Application was made to the disc around the A0-type star Vega and to a variety of discs around G2-type stars. For the latter, the long-term evolution was studied. First, numerical simulations with the collisional code were performed. Second, the numerical results were supplemented by, and interpreted with, a new analytic model. This model is similar to, and builds up on, the model developed earlier by Wyatt et al. (2007a), but extends it in several important directions. It naturally includes the transition from the “primordial” size distribution of left-over planetesimals, set up at their agglomeration phase, to the size distribution established by the collisional cascade. Further, it lifts the assumption that the critical specific energy needed for disruption and dispersal is constant across the full range of sizes, from dust to the largest planetesimals. With these improvements, a good agreement between numerics and analytics as well as observational statistics is achieved.

Our main findings can be divided into two categories: the properties of size and spatial distributions in quasi-steady state and the temporal evolution of these distributions and of a disc’s dust and mass budget.

Size and Spatial Distribution

1. *Size distribution with five regimes.* At least five basic size regimes can be identified: (I) the *smallest dust particles*, which are unbound and rapidly ejected from the system due to radiation pressure; (II) *barely bound dust grains* slightly above this blowout limit, populating highly eccentric orbits independent from the distribution of eccentricities of their parent bodies; (III) objects with no or little response to radiation pressure whose collisional equilibrium distribution is set by *material strength*; (IV) objects larger than around 100 metres, whose collisional equilibrium distribution is set by *self-gravity*; and (V) the *largest planetesimals* whose collisional timescales are too long and their size distribution still primordial.

2. *Wavy size distribution of dust.* The radiation pressure strongly influences the grain size distribution in a debris disc. The smallest grains are unbound and depleted and cannot efficiently erode the

population of barely bound grains. The resulting overabundance of barely bound grains leads again to an underabundance of somewhat larger particles, and so on. In the steady-state size distribution, a well-understood (Campo Bagatin et al. 1994; Thébault et al. 2003) wavy pattern emerges, whose wavelength and amplitude strongly depend on the grains' mechanical properties and average impact velocities.

3. *Grains that dominate thermal emission*. For a collision-dominated disc with moderate orbital eccentricities of the planetesimal population, the total cross sectional area is dominated by particles somewhat above the blowout limit, i.e. by the smallest grains that can barely stay in bound orbits against the radiation pressure. For the Vega disc, this corresponds to a grain radius of roughly 10 µm. The disc's brightness and spectral energy distribution at mid and far-infrared wavelengths are dominated by the same particles. The cross sectional density of smaller particles, sweeping through the disc in hyperbolic orbits, is by about two orders of magnitude lower. This finding contradicts elsewhere derived empirical size distributions but is supported by fundamental considerations. Only for so-called dynamically cold discs with average eccentricities below ~ 0.01, the highly eccentric barely bound grains are depleted and grains larger than 100 micrometre become important.

4. *Spatial distribution of dust*. The outer slope of the radial profile of the normal optical depth, $\tau_\perp \propto r^\alpha$, converges in time towards an upper limit of $\alpha \approx -1.5$ for steady state. This would correspond to a power law index of the surface brightness profile between -2 and, more likely, -4 if the thermal emission mainly comes from ~ 10 µm-sized grains, as suggested by the size distribution derived here. This may be consistent with resolved observations of the Vega disc that reveal profiles with a surface brightness index of -3 to -4 (Su et al. 2005).

5. *Mass and mass loss of Vega's disc*. The total disc masses needed for the model discs to produce the observed amount of micron and submillimetre-sized dust around Vega do not exceed several Earth masses for an upper size limit of 300 metres for rocky bodies. Even if the size distribution holds for objects that are 2 orders of magnitude larger (30 kilometres), the total mass of 10 to 30 Earth masses will still be reasonable. Mass and mass loss are consistent with a continuous collisional cascade if the observed emission is dominated by dust grains on bound orbits, as is suggested here. Transient events like a recent large collision are argued to be unlikely scenarios for the observed Vega disc.

Temporal Evolution

1. *Timescales for reaching steady state in the dust regime.* The size distribution converges towards the aforementioned quasi-steady state on timescales depending on the collision rates. The latter, in turn, depend on grain sizes and the distance from the star. For grains up to some hundred µm orbiting Vega at 100 astronomical units, about 1 million years are needed to reach a steady state.

2. *Scaling laws.* Empirical scaling laws are derived from the numerical results and are in good agreement with the analytic models. The timescale for the collisional evolution, T, is inversely proportional to the initial disc mass and shows a $r^{4.3}$ dependence on the radial distance r. The collisional lifetime of objects unaffected by stellar radiation and the timescale for mass loss through blowout of smallest dust grains by the stellar radiation vary with the average orbital eccentricity e of dust parent bodies as $e^{-2.3}$ – in contrast to rough analytic estimates, which yield $e^{-1.75}$.

3. *Analytic model.* An analytic approximation of the evolution of the three size regimes for larger objects, (III), (IV), and (V), is developed. The transitional size between the primordial and the collisionally evolved size distribution increases with time, meaning that ever-larger planetesimals get involved in the collisional cascade. The model is shown to approximately reproduce the numerical results.

4. *Dust mass and disc mass.* At actual ages of debris discs, $\sim$10 million years to $\sim$10 billion years, the decay of the dust mass and the total disc mass follow different laws. The reason is that, in all conceivable debris discs, the largest planetesimals (V) have longer collisional lifetimes than the system's age, and therefore did not have enough time to reach a collisional equilibrium. If the system were let to evolve for sufficiently long time t, both dust mass and disc mass would start to follow t^{-1}. However, this requires time spans of much longer than 10 billion years.

5. *Decay of luminosity.* The loss rate of the dust mass and the decay rate of fractional luminosity primarily depend on the difference between the slope q_p of the primordial size distribution of largest planetesimals (V) and the slope q_g of the size distribution of somewhat smaller, yet gravity-dominated, planetesimals that already underwent sufficient collisional evolution (IV). For reasonable values of q_p and q_g, the dust mass and the thermal fluxes follow approximately t^ξ with $\xi = -0.3 \ldots -0.4$. Other important parameters are: the critical fragmentation energy Q_D^* as a function of size and the maximum size of planetesimals as well as their characteristic orbital eccentricity and inclination.

6. *Synthetic population versus observations.* Assuming standard material prescriptions as well as disc masses and extents, a synthetic population of discs generated with our analytic model generally agrees with the observed statistics of 24 and 70 micron fluxes versus age. Similarly, the ratios of the synthetic fluxes at both wavelengths are consistent with the observed disc colours.

Outlook

As every model, the numerical and the analytic models presented here make a number of general, simplifying assumptions and compromises with respect to computational effort. Despite these limitations, the models reproduce, in essential part, the observed evolution of dust in debris discs. They may serve as a starting point for possible in-depth studies on more specific processes. Some examples are listed below.

- The collisional evolution in the current model is assumed to be smooth and unperturbed. Singular episodes like the aftermath of giant break-ups or special periods of the dynamical evolution such as the late heavy bombardment are not included.

- Effects of perturbing planets are taken into account only indirectly: through the eccentricities of planetesimals (dynamical excitation) and confinement of planetesimal belts (truncation of discs). Further effects such as resonant trapping or ejection of material by possibly migrating planets are neglected.

- The present work neither covers dilute discs under the regime of Poynting-Robertson drag (although implemented in the model) nor very dense, and possibly gaseous, discs with collisional timescales shorter than the orbital timescales. In the latter, dusty avalanches are induced and fed by a cascade of collisions between blowout grains and grains on bound orbits.

- Explaining the initial conditions or deriving them from the dynamical history of the systems at early stages of planetesimal and planetary accretion was out of the scope of this work. Correlations between disc masses, disc radii, and the presence of planets, for example, were not considered and not at hand, although they might alter the scalings found here.

Clear motivation for future work arises from the questions that remain unanswered, as well as by new data expected from ongoing and planned observational programmes.

Bibliography

ABSIL, O.; DI FOLCO, E.; MÉRAND, A.; et al. (2006): Circumstellar material in the Vega inner system revealed by CHARA/FLUOR. In: *Astronomy & Astrophysics*, 452, pp. 237–244.

ALLEN, C. W. (1973): *Astrophysical quantities*, 3rd edn., London: University of London, Athlone Press.

ALTOBELLI, N.; KEMPF, S.; ROY, M.; et al. (2007): Preliminary Results on Analysis of the Cosmic Dust Analyzer Data Between Jupiter and Saturn. In: *Dust in Planetary Systems*, 643, pp. 65–68.

ARAKAWA, M. (1999): Collisional Disruption of Ice by High-Velocity Impact. In: *Icarus*, 142, pp. 34–45.

ARTYMOWICZ, P. (1997): Beta Pictoris: an Early Solar System? In: *Annual Review of Earth and Planetary Science*, 25, pp. 175–219.

ASPHAUG, E.; OSTRO, S. J.; HUDSON, R. S.; et al. (1998): Disruption of kilometre-sized asteroids by energetic collisions. In: *Nature*, 393, pp. 437–440.

AUGEREAU, J.; BEUST, H. (2006): The AU Mic debris ring. Density profile and dynamics of the dust. In: *Astronomy & Astrophysics*, 455, pp. 987–999.

AUMANN, H. H.; BEICHMAN, C. A.; GILLETT, F. C.; et al. (1984): Discovery of a shell around Alpha Lyrae. In: *The Astrophysical Journal Letters*, 278, pp. 23–27.

BACKMAN, D. E.; DASGUPTA, A.; STENCEL, R. E. (1995): Model of a Kuiper Belt Small Grain Population and Resulting Far-Infrared Emission. In: *The Astrophysical Journal Letters*, 450, pp. 35–38.

BACKMAN, D. E.; PARESCE, F. (1993): Main-sequence stars with circumstellar solid material – The Vega phenomenon. In: *Protostars and Planets III*, ed. E. H. Levy & J. I. Lunine, pp. 1253–1304.

BEICHMAN, C. A.; BRYDEN, G.; RIEKE, G. H.; et al. (2005): Planets and Infrared Excesses: Preliminary Results from a Spitzer MIPS Survey of Solar-Type Stars. In: *The Astrophysical Journal*, 622, pp. 1160–1170.

BEICHMAN, C. A.; BRYDEN, G.; STAPELFELDT, K. R.; et al. (2006a): New Debris Disks around Nearby Main-Sequence Stars: Impact on the Direct Detection of Planets. In: *The Astrophysical Journal*, 652, pp. 1674–1693.

BEICHMAN, C. A.; NEUGEBAUER, G.; HABING, H. J.; et al. (1988): IRAS Catalogs and Atlases, Version 2. Explanatory Supplement. In: *NASA Reference Publication*, 1190, pp. 1–450.

BEICHMAN, C. A.; TANNER, A.; BRYDEN, G.; et al. (2006b): IRS Spectra of Solar-Type Stars: A Search for Asteroid Belt Analogs. In: *The Astrophysical Journal*, 639, pp. 1166–1176.

BENZ, W.; ASPHAUG, E. (1999): Catastrophic Disruptions Revisited. In: *Icarus*, 142, pp. 5–20.

BENZ, W.; ASPHAUG, E.; RYAN, E. V. (1994): Numerical simulations of catastrophic disruption: Recent results. In: *Planetary and Space Science*, 42, pp. 1053–1066.

BERNSTEIN, G. M.; TRILLING, D. E.; ALLEN, R. L.; et al. (2004): The Size Distribution of Trans-Neptunian Bodies. In: *The Astronomical Journal*, 128, pp. 1364–1390.

BEUST, H.; LAGRANGE-HENRI, A. M.; VIDAL-MADJAR, A.; FERLET, R. (1989): The Beta Pictoris circumstellar disk. IX – Theoretical results on the infall velocities of CA II, AL III, and MG II. In: *Astronomy & Astrophysics*, 223, pp. 304–312.

BEUST, H.; MORBIDELLI, A. (2000): Falling Evaporating Bodies as a Clue to Outline the Structure of the β Pictoris Young Planetary System. In: *Icarus*, 143, pp. 170–188.

BLUM, J.; WURM, G.; KEMPF, S.; et al. (2000): Growth and Form of Planetary Seedlings: Results from a Microgravity Aggregation Experiment. In: *Physical Review Letters*, 85, pp. 2426–2429.

BOHREN, C. F.; HUFFMAN, D. R. (1983): *Absorption and scattering of light by small particles*, New York: Wiley.

BRYDEN, G.; BEICHMAN, C. A.; TRILLING, D. E.; et al. (2006): Frequency of Debris Disks around Solar-Type Stars: First Results from a Spitzer MIPS Survey. In: *The Astrophysical Journal*, 636, pp. 1098–1113.

BURNS, J. A.; LAMY, P. L.; SOTER, S. (1979): Radiation forces on small particles in the solar system. In: *Icarus*, 40, pp. 1–48.

CAMPO BAGATIN, A.; CELLINO, A.; DAVIS, D. R.; et al. (1994): Wavy size distributions for collisional systems with a small-size cutoff. In: *Planetary and Space Science*, 42, pp. 1079–1092.

CAMPO BAGATIN, A.; PETIT, J.-M. (2001): Effects of the Geometric Constraints on the Size Distributions of Debris in Asteroidal Fragmentation. In: *Icarus*, 149, pp. 210–221.

CHARNOZ, S.; BRAHIC, A. (2001): Long-term collisional evolution of a dissipative particle disc perturbed by a giant-planet embryo. In: *Astronomy & Astrophysics*, 375, pp. 31–34.

CHARNOZ, S.; THÉBAULT, P.; BRAHIC, A. (2001): Short-term collisional evolution of a disc perturbed by a giant-planet embryo. In: *Astronomy & Astrophysics*, 373, pp. 683–701.

CHEN, C. H.; JURA, M.; GORDON, K. D.; BLAYLOCK, M. (2005a): A Spitzer Study of Dusty Disks in the Scorpius-Centaurus OB Association. In: *The Astrophysical Journal*, 623, pp. 493–501.

CHEN, C. H.; PATTEN, B. M.; WERNER, M. W.; et al. (2005b): A Spitzer Study of Dusty Disks around Nearby, Young Stars. In: *The Astrophysical Journal*, 634, pp. 1372–1384.

CHEN, C. H.; SARGENT, B. A.; BOHAC, C.; et al. (2006): Spitzer IRS Spectroscopy of IRAS-discovered Debris Disks. In: *The Astrophysical Journal Supplement*, 166, pp. 351–377.

CHINI, R.; KRÜGEL, E.; KREYSA, E. (1990): Large dust particles around main sequence stars. In: *Astronomy & Astrophysics*, 227, pp. 5–8.

DAVIS, D. R.; CHAPMAN, C. R.; GREENBERG, R.; et al. (1979): Collisional evolution of asteroids – Populations, rotations, and velocities. In: *Asteroids*, pp. 528–557.

DAVIS, D. R.; CHAPMAN, C. R.; WEIDENSCHILLING, S. J.; GREENBERG, R. (1985): Collisional history of asteroids: Evidence from Vesta and the Hirayama families. In: *Icarus*, 63, pp. 30–53.

DAVIS, D. R.; RYAN, E. V. (1990): On collisional disruption – Experimental results and scaling laws. In: *Icarus*, 83, pp. 156–182.

DELLER, A. T.; MADDISON, S. T. (2005): Numerical Modeling of Dusty Debris Disks. In: *The Astrophysical Journal*, 625, pp. 398–413.

DELL'ORO, A.; PAOLICCHI, P. (1998): Statistical Properties of Encounters among Asteroids: A New, General Purpose, Formalism. In: *Icarus*, 136, pp. 328–339.

DELSANTI, A.; JEWITT, D. (2006): The Solar System Beyond The Planets. In: *Solar System Update*, p. 267.

DENT, W. R. F.; WALKER, H. J.; HOLLAND, W. S.; GREAVES, J. S. (2000): Models of the dust structures around Vega-excess stars. In: *Monthly Notices of the Royal Astronomical Society*, 314, pp. 702–712.

DIKAREV, V.; GRÜN, E. (2002): New information recovered from the Pioneer 11 meteoroid experiment data. In: *Astronomy & Astrophysics*, 383, pp. 302–308.

DIKAREV, V.; GRÜN, E.; BAGGALEY, J.; et al. (2005): The new ESA meteoroid model. In: *Advances in Space Research*, 35, pp. 1282–1289.

DOHNANYI, J. S. (1969): Collisional models of asteroids and their debris. In: *Journal of Geographic Research*, 74, pp. 2531–2554.

—. (1973): Current Evolution of Meteoroids. In: *NASA Special Publication*, 319, pp. 363–374.

—. (1978): Particle dynamics. In: *Cosmic Dust*, ed. J. A. M. McDonnell, Chichester, UK: Wiley-Interscience, pp. 527–605.

DOMINIK, C.; DECIN, G. (2003): Age Dependence of the Vega Phenomenon: Theory. In: *The Astrophysical Journal*, 598, pp. 626–635.

DONNISON, J. R. (2006): The size distribution of trans-Neptunian bodies. In: *Planetary and Space Science*, 54, pp. 243–250.

DRAINE, B. T. (2003): Scattering by Interstellar Dust Grains. II. X-Rays. In: *The Astrophysical Journal*, 598, pp. 1026–1037.

Duncan, M.; Quinn, T.; Tremaine, S. (1988): The origin of short-period comets. In: *The Astrophysical Journal Letters*, 328, pp. 69–73.

Duncan, M. J.; Levison, H. F. (1997): A scattered comet disk and the origin of Jupiter family comets. In: *Science*, 276, pp. 1670–1672.

Durda, D. D.; Bottke, W. F.; Nesvorný, D.; et al. (2007): Size frequency distributions of fragments from SPH/N-body simulations of asteroid impacts: Comparison with observed asteroid families. In: *Icarus*, 186, pp. 498–516.

Durda, D. D.; Dermott, S. F. (1997): The Collisional Evolution of the Asteroid Belt and Its Contribution to the Zodiacal Cloud. In: *Icarus*, 130, pp. 140–164.

Durda, D. D.; Greenberg, R.; Jedicke, R. (1998): Collisional Models and Scaling Laws: A New Interpretation of the Shape of the Main-Belt Asteroid Size Distribution. In: *Icarus*, 135, pp. 431–440.

Epifani, E.; Colangeli, L.; Fulle, M.; et al. (2001): ISOCAM Imaging of Comets 103P/Hartley 2 and 2P/Encke. In: *Icarus*, 149, pp. 339–350.

Fechtig, H.; Hartung, J. B.; Nagel, K.; et al. (1974): Lunar microcrater studies, derived meteoroid fluxes, and comparison with satellite-borne experiments. In: *Lunar and Planetary Science Conference*, Vol. 5, pp. 2463–2474.

Freistetter, F.; Krivov, A. V.; Löhne, T. (2007): Planets of β Pictoris revisited. In: *Astronomy & Astrophysics*, 466, pp. 389–393.

Fujiwara, A. (1986): Results obtained by laboratory simulations of catastrophic impact. In: *Memorie della Societa Astronomica Italiana*, 57, pp. 47–64.

Fujiwara, A.; Kamimoto, G.; Tsukamoto, A. (1977): Destruction of basaltic bodies by high-velocity impact. In: *Icarus*, 31, pp. 277–288.

Fujiwara, A.; Tsukamoto, A. (1980): Experimental study on the velocity of fragments in collisional breakup. In: *Icarus*, 44, pp. 142–153.

Fulle, M.; Mikuz, H.; Bosio, S. (1997): Dust environment of Comet Hyakutake 1996B2. In: *Astronomy & Astrophysics*, 324, pp. 1197–1205.

Galligan, D. P.; Baggaley, W. J. (2004): The orbital distribution of radar-detected meteoroids of the Solar system dust cloud. In: *Monthly Notices of the Royal Astronomical Society*, 353, pp. 422–446.

—. (2005): The radiant distribution of AMOR radar meteors. In: *Monthly Notices of the Royal Astronomical Society*, 359, pp. 551–560.

Goldreich, P.; Lithwick, Y.; Sari, R. (2004): Planet Formation by Coagulation: A Focus on Uranus and Neptune. In: *Annual Review of Astronomy and Astrophysics*, 42, pp. 549–601.

Gomes, R.; Levison, H. F.; Tsiganis, K.; Morbidelli, A. (2005): Origin of the cataclysmic Late Heavy Bombardment period of the terrestrial planets. In: *Nature*, 435, pp. 466–469.

Gomes, R. S.; Morbidelli, A.; Levison, H. F. (2004): Planetary migration in a planetesimal disk: why did Neptune stop at 30 AU? In: *Icarus*, 170, pp. 492–507.

Gor'kavyi, N. N.; Ozernoy, L. M.; Mather, J. C. (1997a): A New Approach to Dynamical Evolution of Interplanetary Dust. In: *The Astrophysical Journal*, 474, pp. 496–502.

Gor'kavyi, N. N.; Ozernoy, L. M.; Mather, J. C.; Taidakova, T. (1997b): Quasi-Stationary States of Dust Flows under Poynting-Robertson Drag: New Analytical and Numerical Solutions. In: *The Astrophysical Journal*, 488, pp. 268–276.

Gorlova, N.; Rieke, G. H.; Muzerolle, J.; et al. (2006): Spitzer 24 µm Survey of Debris Disks in the Pleiades. In: *The Astrophysical Journal*, 649, pp. 1028–1042.

Greaves, J. S. (2005): Disks Around Stars and the Growth of Planetary Systems. In: *Science*, 307, pp. 68–71.

Greaves, J. S.; Holland, W. S.; Wyatt, M. C.; et al. (2005): Structure in the ε Eridani Debris Disk. In: *The Astrophysical Journal Letters*, 619, pp. 187–190.

Greaves, J. S.; Wyatt, M. C. (2003): Some anomalies in the occurrence of debris discs around main-sequence A and G stars. In: *Monthly Notices of the Royal Astronomical Society*, 345, pp. 1212–1222.

Greenberg, R.; Hartmann, W. K.; Chapman, C. R.; Wacker, J. F. (1978): Planetesimals to planets – Numerical simulation of collisional evolution. In: *Icarus*, 35, pp. 1–26.

GRIGORIEVA, A.; ARTYMOWICZ, P.; THÉBAULT, P. (2007a): Collisional dust avalanches in debris discs. In: *Astronomy & Astrophysics*, 461, pp. 537–549.

GRIGORIEVA, A.; THÉBAULT, P.; ARTYMOWICZ, P.; BRANDEKER, A. (2007b): Survival of icy grains in debris discs – The role of photosputtering. In: *Astronomy & Astrophysics*, 475, pp. 755–764.

GRÜN, E.; GUSTAFSON, B. A. S.; DERMOTT, S.; FECHTIG, H., eds. (2001): *Interplanetary Dust* (Astronomy and Astrophysics Library), Berlin: Springer.

GRÜN, E.; SVESTKA, J. (1996): Physics of Interplanetary and Interstellar Dust. In: *Space Science Reviews*, 78, pp. 347–360.

GRÜN, E.; ZOOK, H. A.; FECHTIG, H.; GIESE, R. H. (1985): Collisional balance of the meteoritic complex. In: *Icarus*, 62, pp. 244–272.

GUSTAFSON, B. A. S. (1994): Physics of Zodiacal Dust. In: *Annual Review of Earth and Planetary Sciences*, 22, pp. 553–595.

HADAMCIK, E.; LEVASSEUR-REGOURD, A. C. (2003): Dust evolution of comet C/1995 O1 (Hale-Bopp) by imaging polarimetric observations. In: *Astronomy & Astrophysics*, 403, pp. 757–768.

HAHN, J. M.; MALHOTRA, R. (2005): Neptune's Migration into a Stirred-Up Kuiper Belt: A Detailed Comparison of Simulations to Observations. In: *The Astronomical Journal*, 130, pp. 2392–2414.

HENNING, T.; IL'IN, V. B.; KRIVOVA, N. A.; et al. (1999): WWW database of optical constants for astronomy. In: *Astronomy and Astrophysics Supplement*, 136, pp. 405–406.

HILLENBRAND, L. A.; CARPENTER, J. M.; KIM, J. S.; et al. (2008): The Complete Census of 70 μm-bright Debris Disks within "the Formation and Evolution of Planetary Systems" Spitzer Legacy Survey of Sun-like Stars. In: *The Astrophysical Journal*, 677, pp. 630–656.

HIRAOKA, K.; ARAKAWA, M.; YOSHIKAWA, K.; NAKAMURA, A. M. (2007): Laboratory experiments of crater formation on ice silicate mixture targets. In: *Advances in Space Research*, 39, pp. 392–399.

HOLLAND, W. S.; GREAVES, J. S.; ZUCKERMAN, B.; et al. (1998): Submillimetre images of dusty debris around nearby stars. In: *Nature*, 392, pp. 788–790.

HORÁNYI, M. (1996): Charged Dust Dynamics in the Solar System. In: *Annual Review of Astronomy and Astrophysics*, 34, pp. 383–418.

HUMES, D. H. (1980): Results of Pioneer 10 and 11 meteoroid experiments – Interplanetary and near-Saturn. In: *Journal of Geographic Research*, 85, pp. 5841–5852.

IDA, S. (1990): Stirring and dynamical friction rates of planetesimals in the solar gravitational field. In: *Icarus*, 88, pp. 129–145.

IDA, S.; BRYDEN, G.; LIN, D. N. C.; TANAKA, H. (2000): Orbital Migration of Neptune and Orbital Distribution of Trans-Neptunian Objects. In: *The Astrophysical Journal*, 534, pp. 428–445.

IDA, S.; MAKINO, J. (1993): Scattering of planetesimals by a protoplanet – Slowing down of runaway growth. In: *Icarus*, 106, pp. 210–227.

ISHIMOTO, H. (2000a): An Analytical Model for the Mass Distribution of the Interplanetary Dust Cloud. In: *Advances in Space Research*, 25, pp. 281–284.

—. (2000b): Modeling the number density distribution of interplanetary dust on the ecliptic plane within 5AU of the Sun. In: *Astronomy & Astrophysics*, 362, pp. 1158–1173.

JEWITT, D.; LUU, J. (1993): Discovery of the candidate Kuiper belt object 1992 QB1. In: *Nature*, 362, pp. 730–732.

JEWITT, D.; LUU, J.; TRUJILLO, C. (1998): Large Kuiper Belt Objects: The Mauna Kea 8K CCD Survey. In: *The Astronomical Journal*, 115, pp. 2125–2135.

JORDA, L.; LAMY, P.; FAURY, G.; et al. (2007): Properties of the dust cloud caused by the Deep Impact experiment. In: *Icarus*, 191, pp. 412–423.

JOSWIAK, D. J.; BROWNLEE, D. E.; PEPIN, R. O.; SCHLUTTER, D. J. (2007): Densities and Mineralogy of Cometary and Asteroidal Interplanetary Dust Particles Collected in the Stratosphere. In: *Dust in Planetary Systems* (ESA SP), Vol. 643, pp. 141–144.

JURA, M.; CHEN, C. H.; FURLAN, E.; et al. (2004): Mid-Infrared Spectra of Dust Debris around Main-

Sequence Stars. In: *The Astrophysical Journal Supplement*, 154, pp. 453–457.

KELSALL, T.; WEILAND, J. L.; FRANZ, B. A.; et al. (1998): The COBE Diffuse Infrared Background Experiment Search for the Cosmic Infrared Background. II. Model of the Interplanetary Dust Cloud. In: *The Astrophysical Journal*, 508, pp. 44–73.

KEMPF, S.; BECKMANN, U.; SRAMA, R.; et al. (2006): The electrostatic potential of E ring particles. In: *Planetary and Space Science*, 54, pp. 999–1006.

KENYON, S. J.; BROMLEY, B. C. (2004): The Size Distribution of Kuiper Belt Objects. In: *The Astronomical Journal*, 128, pp. 1916–1926.

—. (2005): Prospects for Detection of Catastrophic Collisions in Debris Disks. In: *The Astronomical Journal*, 130, pp. 269–279.

KENYON, S. J.; BROMLEY, B. C.; O'BRIEN, D. P.; DAVIS, D. R. (2008): Formation and Collisional Evolution of Kuiper Belt Objects. In: *The Solar System Beyond Neptune*, ed. M. A. Barucci, H. Boehnhardt, D. P. Cruikshank, & A. Morbidelli, Tucson: University of Arizona Press, pp. 293–313.

KIM, J. S.; HINES, D. C.; BACKMAN, D. E.; et al. (2005): Formation and Evolution of Planetary Systems: Cold Outer Disks Associated with Sun-like Stars. In: *The Astrophysical Journal*, 632, pp. 659–669.

KIMURA, H.; MANN, I. (1998): The Electric Charging of Interstellar Dust in the Solar System and Consequences for Its Dynamics. In: *The Astrophysical Journal*, 499, pp. 454–462.

KOERNER, D. W.; SARGENT, A. I.; OSTROFF, N. A. (2001): Millimeter-Wave Aperture Synthesis Imaging of Vega: Evidence for a Ring Arc at 95 AU. In: *The Astrophysical Journal Letters*, 560, pp. 181–184.

KOKUBO, E.; IDA, S. (1998): Oligarchic Growth of Protoplanets. In: *Icarus*, 131, pp. 171–178.

KOSCHNY, D.; GRÜN, E. (2001a): Impacts into Ice-Silicate Mixtures: Crater Morphologies, Volumes, Depth-to-Diameter Ratios, and Yield. In: *Icarus*, 154, pp. 391–401.

—. (2001b): Impacts into Ice-Silicate Mixtures: Ejecta Mass and Size Distributions. In: *Icarus*, 154, pp. 402–411.

KRIVOV, A. V.; LÖHNE, T.; SREMČEVIĆ, M. (2006): Dust distributions in debris disks: effects of gravity, radiation pressure and collisions. In: *Astronomy & Astrophysics*, 455, pp. 509–519.

KRIVOV, A. V.; MANN, I.; KRIVOVA, N. A. (2000): Size distributions of dust in circumstellar debris discs. In: *Astronomy & Astrophysics*, 362, pp. 1127–1137.

KRIVOV, A. V.; QUECK, M.; LÖHNE, T.; SREMČEVIĆ, M. (2007): On the nature of clumps in debris disks. In: *Astronomy & Astrophysics*, 462, pp. 199–210.

KRIVOV, A. V.; SREMČEVIĆ, M.; SPAHN, F. (2005): Evolution of a Keplerian disk of colliding and fragmenting particles: a kinetic model with application to the Edgeworth-Kuiper belt. In: *Icarus*, 174, pp. 105–134.

KRIVOVA, N. A.; KRIVOV, A. V.; MANN, I. (2000): The Disk of β Pictoris in the Light of Polarimetric Data. In: *The Astrophysical Journal*, 539, pp. 424–434.

KUCHNER, M. J.; HOLMAN, M. J. (2003): The Geometry of Resonant Signatures in Debris Disks with Planets. In: *The Astrophysical Journal*, 588, pp. 1110–1120.

LANDGRAF, M.; LIOU, J.-C.; ZOOK, H. A.; GRÜN, E. (2002): Origins of Solar System Dust beyond Jupiter. In: *The Astronomical Journal*, 123, pp. 2857–2861.

LAOR, A.; DRAINE, B. T. (1993): Spectroscopic constraints on the properties of dust in active galactic nuclei. In: *The Astrophysical Journal*, 402, pp. 441–468.

LE SERGEANT D'HENDECOURT, L. B.; LAMY, P. L. (1980): On the size distribution and physical properties of interplanetary dust grains. In: *Icarus*, 43, pp. 350–372.

—. (1981): Collisional processes among interplanetary dust grains – an unlikely origin for the beta meteoroids. In: *Icarus*, 47, pp. 270–281.

LECAVELIER DES ETANGS, A.; SCHOLL, H.; ROQUES, F.; et al. (1996): Perturbations of a Planet on the beta Pictoris Circumstellar Dust Disk. In: *Icarus*, 123, pp. 168–179.

LEINERT, C.; BOWYER, S.; HAIKALA, L. K.; et al. (1998): The 1997 reference of diffuse night sky brightness. In: *Astronomy and Astrophysics Supplement*, 127, pp. 1–99.

LEINERT, C.; GRÜN, E. (1990): Interplanetary Dust. In: *Physics of the Inner Heliosphere I*, ed. R. Schwenn & E. Marsch, Berlin: Springer, pp. 207–275.

LEINERT, C.; RICHTER, I.; PITZ, E.; PLANCK, B. (1981): The zodiacal light from 1.0 to 0.3 A.U. as observed by the HELIOS space probes. In: *Astronomy & Astrophysics*, 103, pp. 177–188.

LEINERT, C.; ROSER, S.; BUITRAGO, J. (1983): How to maintain the spatial distribution of interplanetary dust. In: *Astronomy & Astrophysics*, 118, pp. 345–357.

LESTRADE, J.-F.; WYATT, M. C.; BERTOLDI, F.; et al. (2006): Search for cold debris disks around M-dwarfs. In: *Astronomy & Astrophysics*, 460, pp. 733–741.

LISSAUER, J. J. (1987): Timescales for planetary accretion and the structure of the protoplanetary disk. In: *Icarus*, 69, pp. 249–265.

LISSE, C. M.; BEICHMAN, C. A.; BRYDEN, G.; WYATT, M. C. (2007): On the Nature of the Dust in the Debris Disk around HD 69830. In: *The Astrophysical Journal*, 658, pp. 584–592.

LIU, M. C.; MATTHEWS, B. C.; WILLIAMS, J. P.; KALAS, P. G. (2004): A Submillimeter Search of Nearby Young Stars for Cold Dust: Discovery of Debris Disks around Two Low-Mass Stars. In: *The Astrophysical Journal*, 608, pp. 526–532.

LÖHNE, T.; KRIVOV, A. V.; RODMANN, J. (2008): Long-Term Collisional Evolution of Debris Disks. In: *The Astrophysical Journal*, 673, pp. 1123–1137.

LOVE, S. G.; HÖRZ, F.; BROWNLEE, D. E. (1993): Target Porosity Effects in Impact Cratering and Collisional Disruption. In: *Icarus*, 105, pp. 216–224.

MANN, I.; KÖHLER, M.; KIMURA, H.; et al. (2006): Dust in the solar system and in extra-solar planetary systems. In: *The Astronomy and Astrophysics Review*, 13, pp. 159–228.

MARCUS, A. H. (1969): Speculations on Mass Loss by Meteoroid Impact and Formation of the Planets. In: *Icarus*, 11, pp. 76–87.

MARSH, K. A.; DOWELL, C. D.; VELUSAMY, T.; et al. (2006): Images of the Vega Dust Ring at 350 and 450 µm: New Clues to the Trapping of Multiple-Sized Dust Particles in Planetary Resonances. In: *The Astrophysical Journal Letters*, 646, pp. 77–80.

MATTHEWS, B. C.; GREAVES, J. S.; HOLLAND, W. S.; et al. (2007): An Unbiased Survey of 500 Nearby Stars for Debris Disks: A JCMT Legacy Program. In: *Publications of the Astronomical Society of the Pacific*, 119, pp. 842–854.

MELOSH, H. J.; RYAN, E. V. (1997): NOTE: Asteroids: Shattered but Not Dispersed. In: *Icarus*, 129, pp. 562–564.

MEYER, M. R.; CARPENTER, J. M.; MAMAJEK, E. E.; et al. (2008): Evolution of Mid-Infrared Excess around Sun-like Stars: Constraints on Models of Terrestrial Planet Formation. In: *The Astrophysical Journal Letters*, 673, pp. 181–184.

MEYER, M. R.; HILLENBRAND, L. A.; BACKMAN, D. E.; et al. (2006): The Formation and Evolution of Planetary Systems: Placing Our Solar System in Context with Spitzer. In: *Publications of the Astronomical Society of the Pacific*, 118, pp. 1690–1710.

—. (2004): The Formation and Evolution of Planetary Systems: First Results from a Spitzer Legacy Science Program. In: *The Astrophysical Journal Supplement*, 154, pp. 422–427.

MICHEL, P.; BENZ, W.; TANGA, P.; RICHARDSON, D. C. (2001): Collisions and Gravitational Reaccumulation: Forming Asteroid Families and Satellites. In: *Science*, 294, pp. 1696–1700.

MICHEL, P.; TANGA, P.; BENZ, W.; RICHARDSON, D. C. (2002): Formation of Asteroid Families by Catastrophic Disruption: Simulations with Fragmentation and Gravitational Reaccumulation. In: *Icarus*, 160, pp. 10–23.

MOÓR, A.; ÁBRAHÁM, P.; DEREKAS, A.; et al. (2006): Nearby Debris Disk Systems with High Fractional Luminosity Reconsidered. In: *The Astrophysical Journal*, 644, pp. 525–542.

MORAN, S. M.; KUCHNER, M. J.; HOLMAN, M. J. (2004): The Dynamical Influence of a Planet at Semimajor Axis 3.4 AU on the Dust around ε Eridani. In: *The Astrophysical Journal*, 612, pp. 1163–1170.

MORBIDELLI, A.; EMEL'YANENKO, V. V.; LEVISON, H. F. (2004): Origin and orbital distribution of the trans-Neptunian scattered disc. In: *Monthly Notices of the Royal Astronomical Society*, 355, pp. 935–940.

MORBIDELLI, A.; LEVISON, H. F. (2004): Scenarios for the Origin of the Orbits of the Trans-Neptunian Objects 2000 CR_{105} and 2003 VB_{12} (Sedna). In: *The Astronomical Journal*, 128, pp. 2564–2576.

MORO-MARTÍN, A.; MALHOTRA, R. (2002): A Study of the Dynamics of Dust from the Kuiper Belt: Spatial Distribution and Spectral Energy Distribution. In: *The Astronomical Journal*, 124, pp. 2305–2321.

MOUILLET, D.; LARWOOD, J. D.; PAPALOIZOU, J. C. B.; LAGRANGE, A. M. (1997): A planet on an inclined orbit as an explanation of the warp in the Beta Pictoris disc. In: *Monthly Notices of the Royal Astronomical Society*, 292, pp. 896–904.

NAJITA, J.; WILLIAMS, J. P. (2005): An 850 µm Survey for Dust around Solar-Mass Stars. In: *The Astrophysical Journal*, 635, pp. 625–635.

NAKAMURA, A.; FUJIWARA, A. (1991): Velocity distribution of fragments formed in a simulated collisional disruption. In: *Icarus*, 92, pp. 132–146.

NESVORNÝ, D.; VOKROUHLICKÝ, D.; BOTTKE, W. F.; SYKES, M. (2006): Physical properties of asteroid dust bands and their sources. In: *Icarus*, 181, pp. 107–144.

NOLAN, M. C.; ASPHAUG, E.; MELOSH, H. J.; GREENBERG, R. (1996): Impact Craters on Asteroids: Does Gravity or Strength Control Their Size? In: *Icarus*, 124, pp. 359–371.

O'BRIEN, D. P.; GREENBERG, R. (2003): Steady-state size distributions for collisional populations:analytical solution with size-dependent strength. In: *Icarus*, 164, pp. 334–345.

OWEN, T. C.; ROUSH, T. L.; CRUIKSHANK, D. P.; et al. (1993): Surface ices and the atmospheric composition of Pluto. In: *Science*, 261, pp. 745–748.

OZERNOY, L. M.; GOR'KAVYI, N. N.; MATHER, J. C.; TAIDAKOVA, T. A. (2000): Signatures of Exosolar Planets in Dust Debris Disks. In: *The Astrophysical Journal Letters*, 537, pp. 147–151.

PAN, M.; SARI, R. (2005): Shaping the Kuiper belt size distribution by shattering large but strengthless bodies. In: *Icarus*, 173, pp. 342–348.

PAOLICCHI, P.; VERLICCHI, A.; CELLINO, A. (1996): An Improved Semi-Empirical Model of Catastrophic Impact Processes. I: Theory and Laboratory Experiments. In: *Icarus*, 121, pp. 126–157.

PETIT, J.-M.; FARINELLA, P. (1993): Modelling the outcomes of high-velocity impacts between small solar system bodies. In: *Celestial Mechanics and Dynamical Astronomy*, 57, pp. 1–2.

POPPE, T.; BLUM, J.; HENNING, T. (2000): Analogous Experiments on the Stickiness of Micron-sized Preplanetary Dust. In: *The Astrophysical Journal*, 533, pp. 454–471.

POULTON, C. J.; GREAVES, J. S.; CAMERON, A. C. (2006): Detecting a rotation in the ε Eridani debris disc. In: *Monthly Notices of the Royal Astronomical Society*, 372, pp. 53–59.

POYNTING, J. H. (1903): Radiation in the solar system : its effect on temperature and its pressure on small bodies. In: *Monthly Notices of the Royal Astronomical Society*, 64, pp. 265–266.

PRESS, W. H.; TEUKOLSKY, S. A.; VETTERLING, W. T.; FLANNERY, B. P. (1992): *Numerical Recipes in C*, 2^{nd} edn., Cambridge: Cambridge University Press.

QUECK, M.; KRIVOV, A. V.; SREMČEVIĆ, M.; THÉBAULT, P. (2007): Velocity distributions among colliding asteroids. In: *Celestial Mechanics and Dynamical Astronomy*, 99, pp. 169–196.

QUILLEN, A. C.; MORBIDELLI, A.; MOORE, A. (2007): Planetary embryos and planetesimals residing in thin debris discs. In: *Monthly Notices of the Royal Astronomical Society*, 380, pp. 1642–1648.

QUILLEN, A. C.; THORNDIKE, S. (2002): Structure in the ε Eridani Dusty Disk Caused by Mean Motion Resonances with a 0.3 Eccentricity Planet at Periastron. In: *The Astrophysical Journal Letters*, 578, pp. 149–152.

RAFIKOV, R. R. (2003): Dynamical Evolution of Planetesimals in Protoplanetary Disks. In: *The Astronomical Journal*, 126, pp. 2529–2548.

RHEE, J. W. (1976): Radial distribution of meteoric particles in interplanetary space. In: *Interplanetary Dust and Zodiacal Light*, ed. H. Elsaesser & H. Fechtig (Lecture Notes in Physics, Berlin Springer

Verlag), Vol. 48, pp. 448–452.

RIEKE, G. H.; SU, K. Y. L.; STANSBERRY, J. A.; et al. (2005): Decay of Planetary Debris Disks. In: *The Astrophysical Journal*, 620, pp. 1010–1026.

ROBERTSON, H. P. (1937): Dynamical effects of radiation in the solar system. In: *Monthly Notices of the Royal Astronomical Society*, 97, pp. 423–437.

SCHMIDT, R. M. (1980): Meteor Crater: Energy of formation – Implications of centrifuge scaling. In: *Lunar and Planetary Science Conference Band*, ed. S. A. Bedini (Lunar and Planetary Science Conference), Vol. 11, pp. 2099–2128.

SCHNEIDER, E.; STORZER, D.; HARTUNG, J. B.; et al. (1973): Microcraters on Apollo 15 and 16 samples and corresponding cosmic dust fluxes. In: *Lunar and Planetary Science Conference*, Vol. 4, pp. 656–658.

SIEGLER, N.; MUZEROLLE, J.; YOUNG, E. T.; et al. (2007): Spitzer 24 μm Observations of Open Cluster IC 2391 and Debris Disk Evolution of FGK Stars. In: *The Astrophysical Journal*, 654, pp. 580–594.

SILVERSTONE, M. D.; MEYER, M. R.; MAMAJEK, E. E.; et al. (2006): Formation and Evolution of Planetary Systems (FEPS): Primordial Warm Dust Evolution from 3 to 30 Myr around Sun-like Stars. In: *The Astrophysical Journal*, 639, pp. 1138–1146.

SPANGLER, C.; SARGENT, A. I.; SILVERSTONE, M. D.; et al. (2001): Dusty Debris around Solar-Type Stars: Temporal Disk Evolution. In: *The Astrophysical Journal*, 555, pp. 932–944.

SPAUTE, D.; WEIDENSCHILLING, S. J.; DAVIS, D. R.; MARZARI, F. (1991): Accretional evolution of a planetesimal swarm. I - A new simulation. In: *Icarus*, 92, pp. 147–164.

STAUFFER, J. R.; REBULL, L. M.; CARPENTER, J.; et al. (2005): Spitzer Space Telescope Observations of G Dwarfs in the Pleiades: Circumstellar Debris Disks at 100 Myr Age. In: *The Astronomical Journal*, 130, pp. 1834–1844.

STERN, S. A.; COLWELL, J. E. (1997): Collisional Erosion in the Primordial Edgeworth-Kuiper Belt and the Generation of the 30-50 AU Kuiper Gap. In: *The Astrophysical Journal*, 490, pp. 879–882.

STEWART, G. R.; IDA, S. (2000): Velocity Evolution of Planetesimals: Unified Analytical Formulas and Comparisons with N-Body Simulations. In: *Icarus*, 143, pp. 28–44.

STRUBBE, L. E.; CHIANG, E. I. (2006): Dust dynamics, surface brightness profils, and thermal spectra of debris disks: The case of AU Mic. In: *The Astrophysical Journal*, 648, pp. 652–665.

SU, K. Y. L.; RIEKE, G. H.; MISSELT, K. A.; et al. (2005): The Vega Debris Disk: A Surprise from Spitzer. In: *The Astrophysical Journal*, 628, pp. 487–500.

SU, K. Y. L.; RIEKE, G. H.; STANSBERRY, J. A.; et al. (2006): Debris Disk Evolution around A Stars. In: *The Astrophysical Journal*, 653, pp. 675–689.

TAKAGI, Y.; MIZUTANI, H.; KAWAKAMI, S.-I. (1984): Impact fragmentation experiments of basalts and pyrophyllites. In: *Icarus*, 59, pp. 462–477.

TAKEUCHI, T.; ARTYMOWICZ, P. (2001): Dust Migration and Morphology in Optically Thin Circumstellar Gas Disks. In: *The Astrophysical Journal*, 557, pp. 990–1006.

TANGA, P.; CELLINO, A.; MICHEL, P.; et al. (1999): On the Size Distribution of Asteroid Families: The Role of Geometry. In: *Icarus*, 141, pp. 65–78.

THÉBAULT, P.; AUGEREAU, J.-C. (2005): Upper limit on the gas density in the β Pictoris system. In: *Astronomy & Astrophysics*, 437, pp. 141–148.

—. (2007): Collisional processes and size distribution in spatially extended debris discs. In: *Astronomy & Astrophysics*, 472, pp. 169–185.

THÉBAULT, P.; AUGEREAU, J. C.; BEUST, H. (2003): Dust production from collisions in extrasolar planetary systems. The inner beta Pictoris disc. In: *Astronomy & Astrophysics*, 408, pp. 775–788.

THÉBAULT, P.; WU, Y. (2008): Outer edges of debris discs. How sharp is sharp? In: *Astronomy & Astrophysics*, 481, pp. 713–724.

TRILLING, D. E.; BRYDEN, G.; BEICHMAN, C. A.; et al. (2008): Debris Disks around Sun-like Stars. In: *The Astrophysical Journal*, 674, pp. 1086–1105.

TRILLING, D. E.; STANSBERRY, J. A.; STAPELFELDT, K. R.; et al. (2007): Debris disks in main-sequence binary systems. In: *The Astrophysical Journal*, 658, pp. 1289–1311.

TRUJILLO, C. A.; JEWITT, D. C.; LUU, J. X. (2001): Properties of the Trans-Neptunian Belt: Statistics from the Canada-France-Hawaii Telescope Survey. In: *The Astronomical Journal*, 122, pp. 457–473.

WEIDENSCHILLING, S. J.; SPAUTE, D.; DAVIS, D. R.; et al. (1997): Accretional Evolution of a Planetesimal Swarm. In: *Icarus*, 128, pp. 429–455.

WEISSMAN, P. R. (1984): The Vega particulate shell – Comets or asteroids? In: *Science*, 224, pp. 987–989.

WERNER, M.; FAZIO, G.; RIEKE, G.; et al. (2006): First Fruits of the Spitzer Space Telescope: Galactic and Solar System Studies. In: *Annual Review of Astronomy and Astrophysics*, 44, pp. 269–321.

WILNER, D. J.; HOLMAN, M. J.; KUCHNER, M. J.; HO, P. T. P. (2002): Structure in the Dusty Debris around Vega. In: *The Astrophysical Journal Letters*, 569, pp. 115–119.

WOOD, B. E.; MÜLLER, H.-R.; ZANK, G. P.; LINSKY, J. L. (2002): Measured Mass-Loss Rates of Solar-like Stars as a Function of Age and Activity. In: *The Astrophysical Journal*, 574, pp. 412–425.

WYATT, M. C. (2003): Resonant Trapping of Planetesimals by Planet Migration: Debris Disk Clumps and Vega's Similarity to the Solar System. In: *The Astrophysical Journal*, 598, pp. 1321–1340.

—. (2005): The insignificance of P-R drag in detectable extrasolar planetesimal belts. In: *Astronomy & Astrophysics*, 433, pp. 1007–1012.

—. (2006): Dust in Resonant Extrasolar Kuiper Belts: Grain Size and Wavelength Dependence of Disk Structure. In: *The Astrophysical Journal*, 639, pp. 1153–1165.

WYATT, M. C.; DENT, W. R. F. (2002): Collisional processes in extrasolar planetesimal discs – dust clumps in Fomalhaut's debris disc. In: *Monthly Notices of the Royal Astronomical Society*, 334, pp. 589–607.

WYATT, M. C.; DERMOTT, S. F.; TELESCO, C. M.; et al. (1999): How Observations of Circumstellar Disk Asymmetries Can Reveal Hidden Planets: Pericenter Glow and Its Application to the HR 4796 Disk. In: *The Astrophysical Journal*, 527, pp. 918–944.

WYATT, M. C.; SMITH, R.; GREAVES, J. S.; et al. (2007a): Transience of Hot Dust around Sun-like Stars. In: *The Astrophysical Journal*, 658, pp. 569–583.

WYATT, M. C.; SMITH, R.; SU, K. Y. L.; et al. (2007b): Steady State Evolution of Debris Disks around A Stars. In: *The Astrophysical Journal*, 663, pp. 365–382.

WYATT, S. P. (1969): The electrostatic charge of interplanetary grains. In: *Planetary and Space Science*, 17, pp. 155–171.

ZOOK, H. A.; BERG, O. E. (1975): A source for hyperbolic cosmic dust particles. In: *Planetary and Space Science*, 23, pp. 183–203.

ZOOK, H. A.; MCKAY, D. S. (1986): On the Asteroidal Component of Cosmic Dust. In: *Lunar and Planetary Institute Conference Abstracts*, Vol. 17, pp. 977–978.

ZUBKO, V. G.; MENNELLA, V.; COLANGELI, L.; BUSSOLETTI, E. (1996): Optical constants of cosmic carbon analogue grains – I. Simulation of clustering by a modified continuous distribution of ellipsoids. In: *Monthly Notices of the Royal Astronomical Society*, 282, pp. 1321–1329.

Ehrenwörtliche Erklärung

Ich erkläre hiermit ehrenwörtlich, dass ich die vorliegende Arbeit selbstständig, ohne unzulässige Hilfe Dritter und ohne Benutzung anderer als der angegebenen Hilfsmittel und Literatur angefertigt habe. Die aus anderen Quellen direkt oder indirekt übernommenen Daten und Konzepte sind unter Angabe der Quelle gekennzeichnet.

Weitere Personen waren an der inhaltlich-materiellen Erstellung der vorliegenden Arbeit nicht beteiligt. Insbesondere habe ich hierfür nicht die entgeltliche Hilfe von Vermittlungs- bzw. Beratungsdiensten (Promotionsberater oder andere Personen) in Anspruch genommen. Niemand hat von mir unmittelbar oder mittelbar geldwertige Leistungen für Arbeiten erhalten, die im Zusammenhang mit dem Inhalt der vorgelegten Dissertation stehen.

Die Arbeit wurde bisher weder im In- noch Ausland in gleicher oder ähnlicher Form einer anderen Prüfungsbehörde vorgelegt.

Die geltende Promotionsordnung der Physikalisch-Astronomischen Fakultät ist mir bekannt.

Ich versichere ehrenwörtlich, dass ich nach bestem Wissen die reine Wahrheit gesagt und nichts verschwiegen habe.

Jena, 21. Juli 2008

Torsten Löhne

Lebenslauf

Zur Person

Voller Name	Torsten Löhne
Geburtsdatum	15. Okt. 1979
Geburtsort	Sömmerda/Thüringen
Staatsangehörigkeit	Deutsch

Werdegang

1986-09 – 1987-02	Grundschule in Sömmerda/Thüringen
1987-02 – 1991-07	Grundschule in Steigra/Sachsen-Anhalt
1991-09 – 1998-06	Gymnasium in Querfurt/Sachsen-Anhalt
1998-07-09	Allgemeine Hochschulreife (Abitur)
1998-11 – 1999-08	Grundwehrdienst in Hammelburg/Bayern
1999-10 – 2005-01	Studium der Physik an der Friedrich-Schiller-Universität (FSU) in Jena/Thüringen
2003-11 – 2005-01	Diplomarbeit am Astrophysikalischen Institut und der Universitätssternwarte (AIU) der FSU zum Thema „Bedeckung junger Sterne durch Asteroiden“ unter Betreuung durch Prof. Ralph Neuhäuser
2005-01-31	Diplom in Physik
seit 2005-03	Graduiertenstudium an der FSU als wiss. Mitarbeiter am AIU unter Betreuung durch Prof. Alexander V. Krivov
2005-10 – 2007-07	Betreuung von Studenten als Assistent im Physikalischen Grundpraktikum
2006-12	Teilnahme an Winterschule zum Thema „Kleinkörper in Planetensystemen“ an der Universität Kobe/Japan
2007-10 – 2008-02	Leitung der Übungen zur Vorlesung „Himmelsmechanik“

Jena, 21. Juli 2008

Torsten Löhne